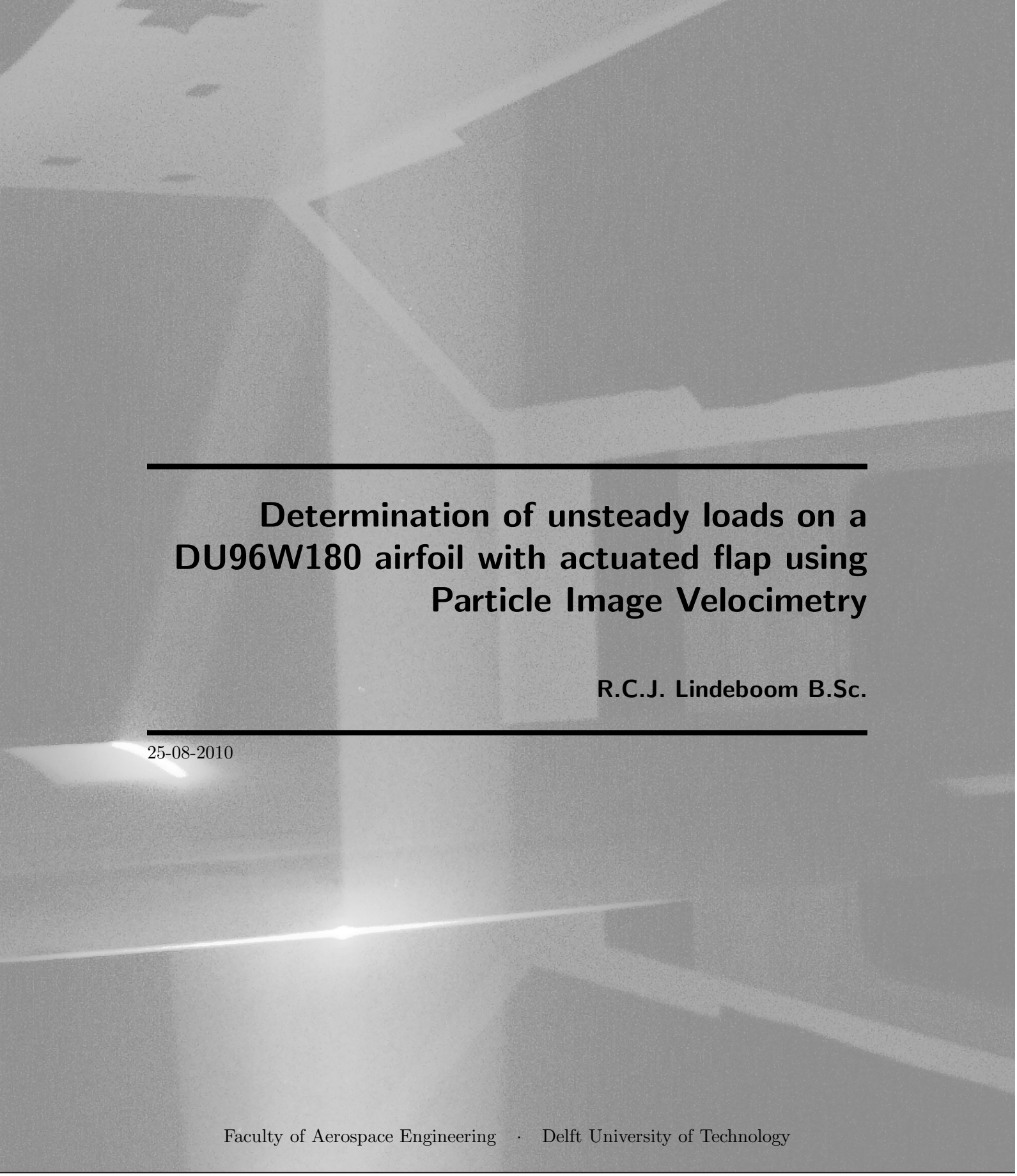

Determination of unsteady loads on a DU96W180 airfoil with actuated flap using Particle Image Velocimetry

R.C.J. Lindeboom B.Sc.

25-08-2010

Faculty of Aerospace Engineering · Delft University of Technology

TU Delft

Determination of unsteady loads on a DU96W180 airfoil with actuated flap using Particle Image Velocimetry

R.C.J. Lindeboom B.Sc.

25-08-2010

Faculty of Aerospace Engineering · Delft University of Technology

Delft University of Technology

Delft University Of Technology
Department Of
Wind energy

The undersigned hereby certify that they have read and recommend to the Faculty of Aerospace Engineering for acceptance a thesis entitled **"Determination of unsteady loads on a DU96W180 airfoil with actuated flap using Particle Image Velocimetry"** by **R.C.J. Lindeboom B.Sc.** in partial fulfillment of the requirements for the degree of **Master of Science**.

Dated: 25-08-2010

Head of department:

prof.dr. G.J.W. van Bussel

Supervisor:

dr.ir.eng. C.J. Simão Ferreira

Co-supervisor:

ir. J.J.H.M Sterenborg

Reader:

dr.ir. B.W. van Oudheusden

Summary

The unsteady flow conditions experienced by wind turbine blades lead to fatigue loads, that increase the cost of energy. The decrease of the impact of these unsteady loads will most certainly lead to a decrease. In order to alleviate unsteady loads the Smart Rotor Blade approach (J.W. van Wingerden et al [2008]) applies spanwise-distributed smart load control devices, which sense the flow and consequently react on the flow. The smart load control devices are applied to avoid the fluctuating unsteady aerodynamic loads. In the context of alleviating these loads, the unsteady behaviour of the flow over a DU96W180 airfoil model due to the oscillation of a $0.2c$ flap is investigated. By building a database of unsteady flow experiments, reference material is created for the validation of Computational Fluid Dynamics models simulating unsteady conditions. Eventually, the knowledge of unsteadiness of the flow acquired, can be applied in projects like the Smart Rotor Blade with the purpose to reduce fluctuating blade loads.

In this thesis two methods are used for the determination of the unsteady force on an airfoil with actuated flap. The experimental approach is based on the acquisition of the velocity fields through Particle Image Velocimetry (PIV). An airfoil model of the type DU96W180, with a span of 1.8 meter and a chord of 0.5 meter is tested. The flow is visualized as a function of flap position under unsteady conditions, using PIV. The unsteadiness addressed is expressed in reduced frequency k, simulating a steady case at $k = 0$ and unsteady flows at $k = 0.1$ and $k = 0.2$. A contour integration technique by F. Noca et al [1999] can determine the forces acting on the body on basis of velocity information enclosing the body. Multiple Fields of View are necessary to capture the mean unsteady flow at different positions around the wing. The flow domain is reconstructed by the interpolation of the sub flow domains to a general grid. The flow behaviour is captured at certain time instances in the period of the flap motion, allowing the determination of a time dependent set of unsteady forces. As a force reference, the lift force is calculated with the concept of circulation.

A potential flow simulation of a panel method is performed on similar unsteady flow cases. The force of the panel method is determined with two distinct methodologies. A direct force output on basis of the pressure will serve as reference for the determination

of the quality of the momentum flux equation. This comparison leads to a thorough understanding on the influence of spatial and temporal resolution on the force as calculated by the momentum flux equation. Analysis is performed on the separate terms contributing to the momentum flux force and consequently coupled to the experimental results. Thereby, insight is created on the error contained in the experimental unsteady force.

Both the model and the experiment follow the theory of Theodorsen, which shows a reduction of amplitude and an increase in phase lag when larger reduced frequencies are considered. The effect of amplitude on the phase lag is most probably best predicted by the evaluation of the experimental lift force by the time independent circulation calculation. The influence of flap amplitude is evaluated and shows that, keeping the reduced frequency constant, a small amplitude induces a larger phase lag compared to larger amplitudes. This result is also found in the evaluation of the momentum flux equation with a relatively coarse time resolution. Thereby the trend of the unsteady lift force is similar for both methods, but differ in the value of the phase lag.

The experimental and simulated results are compared in term of flow quantities and force output. The results reveal that the potential flow simulation shows larger force amplitudes and predicts similar phase lags in case the forces are calculated on basis of the momentum flux equation. However, the validation force methods for both the experiment and the simulation show large discrepancies compared to the momentum flux equation. By comparing the force of the experimental and simulated validation method, it shows that the difference between simulation and experiment is large. From this it can be concluded that the time resolution as applied in this research is too coarse to capture the unsteady flow behaviour.

Finally, it can be stated that the momentum flux method presented has the potential to capture unsteady forces. In order to capture vorticity (as part of the force determination) accurately, spatial refinement is necessary. From the research it also shows that high reduced frequency flows are difficult to capture in terms of time resolution. The noise in the measurements prohibit the accurate determination of acceleration of the flow. Thereby it can be concluded that the determination of unsteady forces is limited by the experimental approach presented in this research.

Acknowledgements

First, I would like to express my gratitude to my supervisor Dr.ir.eng. Carlos *Simão* Ferreira for his continuous support throughout my graduation period. His vision, advice and guidance greatly contributed to my work. I would like to thank my second supervisor ir. Joost Sterenborg for giving me the chance to work on a challenging experiment. His dedication and attitude towards the project inspired me and greatly contributed to this work. I also would like to express my gratitude to Leo Molenwijk, Stefan Bernardy and Frits Donker-Duyvis for all the help they provided me during the setup of the experiment. Also the effort of David Schmidt is appreciated with whom I have shared inights and ideas to perform a good experiment. Without their expertise the experiment would not have been possible.

I am gratefull that I could have shared and distracted my thoughts during my graduation with my fellow roommates. I would like to thank them for their interest and support in my work. I also would like to express my gratefullness towards my friends who carried me along during my educative carreer at the faculty of Aerospace Engineering in Delft.

Most important, many thanks to my parents and family for their continuous support and motivation. Without them I could not have started nor finished my studies.

The work described in this thesis is part of research program of the INNWIND consortium and is carried out within the framework of the EOS-LT programme of the Dutch Ministry of Economical Affairs under contract with SenterNovem.

Delft, The Netherlands R.C.J. Lindeboom B.Sc.
25-08-2010

Contents

Nomenclature

Latin Symbols

A	Flap equilibrium position	[°]
B	Flap amplitude	[°]
C_D	Drag coefficient	[-]
C_L	Lift coefficient	[-]
C_M	Moment coefficient	[-]
S_b	Internal surface bound	[m]
U_∞	Free stream velocity	[m/s]
F	Fluid dynamic force	[N]
I	Unit tensor	[-]
c	Chord	[m]
f	Frequency	[m]
h_f	Frequency	[m]
k	Reduced frequency $k = \frac{\pi f c}{U_\infty}$	[-]
p	Pressure	[Pa]
u,v,w	Velocity component in x,y,z-direction	[m/s]
x	X-Coordinate	[m]
y	Y-Coordinate	[m]

Greek Symbols

Γ	Circulation	$[m^2/\text{s}]$

ξ	Position of singularities	[m]
α	Angle of attack	[$\circ$]
β	Flap angle	[$\circ$]
γ	vorticity	[$\frac{1}{s}$]
μ	Dynamic viscosity	[$\frac{kg}{m/s}$]
ϕ	Phase angle	[$\circ$]
ρ	Density	[$\frac{kg}{m^3}$]

Abbreviations

CFD	Computational Fluid Dynamics
DNS	Direct Numerical Simulation
FIFD	Force Interpolated Force Determination
FOV	Field of view
iFFFD	interpolated Flow Field Force Determination
LES	Large Eddy Simulation
PIV	Particle Image Velocimetry
RANS	Reynolds-Averaged Navier-Stokes
RFD	Raw Force Determination

Chapter 1

Introduction

1.1 Background

The unsteady flow conditions experienced by wind turbine blades lead to fatigue loads due to gusts, that increase the cost of energy. The decrease of the impact of these unsteady loads will most certainly lead to a decrease of the cost of energy. In order to alleviate unsteady loads the Smart Rotor Blade approach (J.W. van Wingerden et al [2008]) applies spanwise-distributed smart load control devices. The smart load control devices are applied to avoid the fluctuating unsteady aerodynamic loads. In the context of alleviating these loads, the unsteady behaviour of the flow over a 2D airfoil model is investigated. The unsteadiness created in the flow is due to the actuation of a $0.2c$ flap.

With the increase of computer power and the increase of the capabilities of cameras and lasers, measurement techniques like Digital Particle Image Velocimetry (DPIV) become more and more competitive in the field of experimental aerodynamics. The advantage of this technique is that the data can be interpreted intuitively due to the visualization of the flow. As opposed to other experimental techniques, PIV is non-intrusive and is able to determine a matrix of data points instead of a single point, which is for example the case in hot wire anemometry. The combination of the flow fields acquired with PIV with an integration technique for the determination of the (unsteady) loads, results in powerful methodologies to evaluate unsteady aerodynamic forces. The integration technique used in this research is based on the work by F. Noca et al [1999], which only uses velocities and its temporal and spatial derivatives on a contour around the airfoil. Each contribution to the force on basis of the contour integration can be coupled to a flow phenomenon which is visible due to the application of PIV. From this set of information, the lift force (lift coefficient), the drag force (drag coefficient) and the aerodynamic moment (moment coefficient) can be calculated.

By building a database of unsteady flow experiments, reference material is created for the validation of computational fluid dynamics models simulating unsteady conditions. Eventually, the knowledge of unsteadiness of the flow acquired can be applied in projects like the Smart Rotor Blade with the purpose to reduce fluctuating blade loads.

1.2 Objective

The objective of this research is defined as:

> *The determination of the unsteady forces on a DU96W180 airfoil with actuated flap by application of Particle Image Velocimetry and validation of the unsteady forces by a potential flow model*

In this thesis the goal is to determine and validate the unsteady loads on a DU96W180 airfoil model with 0.2c actuated flap using particle image velocimetry. An experiment is performed in which the flow is recorded by application of Particle Image Velocimetry. The resulting velocity fields are input for the momentum flux equation, which determines the unsteady force acting on the body. In order to verify the experimental lift force as calculated by the momentum flux equation, use is made of the calculation of the lift force by the concept of circulation.

The unsteady flow around the DU96W180 airfoil with actuated flap is simulated by a potential flow model. This model determines the force acting on the body by means of the pressure available at the surface of the simulated model. The simulation also determines the velocity vector field which again will serve as the input for the momentum flux equation.

The experimental and simulated unsteady force results are compared. This comparison serves to identify the errors that are encountered in the processing procedure to determine the force. Thereafter, the physical difference between the experiment and simulation can be discussed. The flowchart in Figure 1.1 shows the general setup of this thesis.

In Part I of this thesis, a literature research is performed illustrating the background of unsteady aerodynamics and discussing the numerical and experimental approach for the determination of unsteady flow phenomena. In chapter 2 this thesis is put into a perspective as part of the Smart Rotor Blade research. From this general overview the part which deals with the research topic as presented in this thesis, unsteady aerodynamics, is considered in Chapter 3. Chapter 4 gives an overview of the models that can be used to calculate unsteady flow. Chapter 5 describes Theodorsen's theory, to give a mathematical insight in the mechanisms in unsteady aerodynamics. This theory will be used for the validation of the panel code in unsteady conditions. Chapter 6 considers the elementary mathematics for the panel code which is used. Chapter 7 describes the general considerations on experimental aerodynamics. Chapter 8 deals with particle image velocimetry as measurement technique and shows the basics which are needed to perform a proper measurement. Also postprocess techniques will be considered in this chapter. Chapter 9

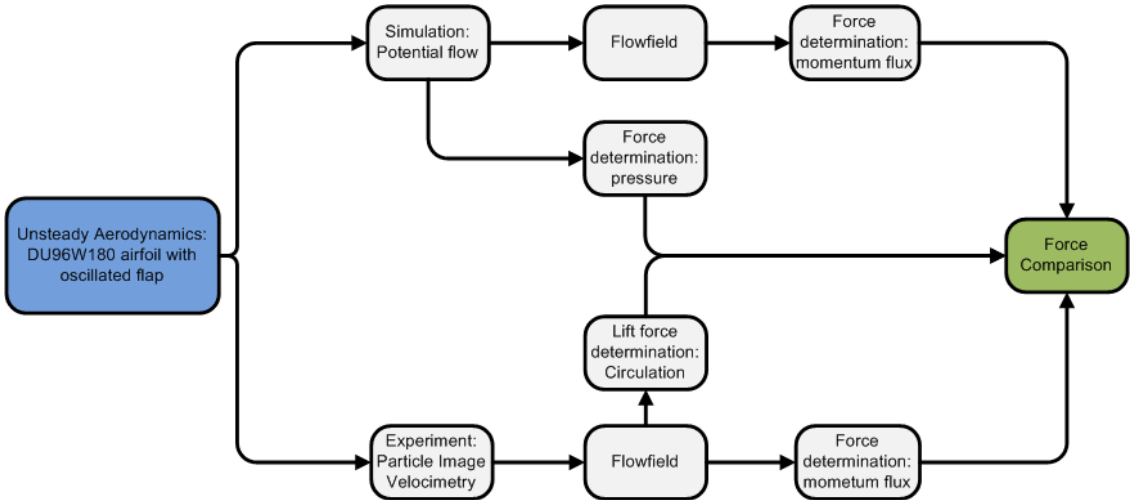

Figure 1.1: The determination of the unsteady force on a DU96W180 airfoil with oscillated flap in the perspective of experiment and potential flow simulation.

deals with the momentum flux equation. Firstly the mathematical form of this equation is presented and thereafter a thorough analysis in correspondence with experimental PIV errors is addressed.

In part II the experiment is considered. Chapter 10 describes the setup of the experiment. A description is given on the experimental procedure and the experimental equipment used. This chapter gives an indication where experimental errors might be introduced and shows the reader the difficulties of performing this experiment. Chapter 11 discusses the postprocessing techniques in relation with the force evaluation. In Chapter 12 the lift and drag force are calculated for the different testcases considered in steady and unsteady conditions. The lift force is calculated by the application of the concept of cirulation. Thereafter the steady and unsteady results as calculated by the momentum flux equation and the the concept of circulation, are compared and discussed in terms of amplitude reduction and phase lag. The chapter is finalized by a discussion on the subcomponents of the momentum flux equation and the error estimation on basis of the techniques described in section 9.

In part III the unsteady flow problem is considered by making use of Computational Fluid Dynamics (CFD). Chapter 13 is devoted to the setup of the potential flow model. It discusses the convergence of the force results and shows a visualisation of the determined flow quantities. In Chapter 14 the unsteady lift force is determined by determining the force on basis of the pressure at the body surface and by application of the momentum flux equation, where the same temporal and spatial resolution are applied as used in the experiment. The chapter adresses the steady and unsteady results and compares the results of the two force determination methods (momentum flux equation and the determination of the force through the pressure) in terms of force amplitude and phase lag. Important to note is that this chapter uses the same approach for the determination of the unsteady force through the momentum flux equation in order to identify the possible errors encountered in the experiment.

In Chapter 15 part IV a comparison is made between the experiment and potential flow simulation. An identification of the errors between experiment and simulation is performed. By reducing the processing errors, insight in the difference between the potential flow model and the experiment is created. Chapters 16 and 17 give the conclusions and recommendations on this research.

Part I

Literature research

Chapter 2

Smart Rotor Blade Research

A trend towards larger rotor radii for off shore wind turbines is observed over the years. The energy yield increases with the square of the rotor diameter. A side effect of increasing the rotor diameter is the relative increase of loads on the windturbine structure. A larger radius implies a larger moment working on the blade, the hub, the generator and the foundation, increasing the demands on the structure itself. Generally, it can be stated that a larger rotor blade implies an increasing *mass effect* and an increase in *fluctuations in the flow field*. To compensate for the mass effect, lighter structures are required, increasing the flexibility of the blades. However, flexibility in combination with larger fluctuation in the flowfield, increase the fatigue loading on the structure.

In order to decrease these fatigue loads on the structure, an advanced control concept can be used in which a number of control devices locally change the profile of the blade. This concept is used for many years on aircraft wings (see Figure 2.1). By applying such a concept, the forces can be reduced locally, implying less stress between different rotorblade sections. In combination with appropriate sensors, loads can be read and used in the control scheme which in turn produces an actuation signal for the control of the actuators. This concept is known as the Smart Rotor Concept. This concept is already being applied in the helicopter industry where trailing edge flaps reduce the loads on the rotor. Especially fatigue loads are targeted by the smart rotor concept, increasing the lifetime of the windturbine and hence reducing the costs for wind energy consumers. An impression of the rotor blade concept is depicted in Figure 2.2.

Research has been performed on the Smart Rotor Blade where trailing edge flaps and micro-electro-mechanical tabs were used. Firstly, a feasibility study was performed by Busualdo in which a trailing edge flap in two dimensional flow was tested. This research was extended to a rotating blade by T. Buhl et al [2005]. The first proof of concept was shown by C. Bak et al [2007]. Validation of the two dimensional model of Takahashi [2006] was part of the work of C. Bak et al [2007] research in which a rigid cross section with a trailing edge flap was used. Currently, research is performed with the goal to prove

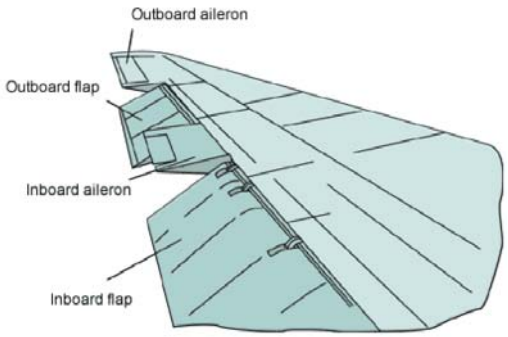

Figure 2.1: The Smart Rotor Blade is equiped with similar control devices as on aircraft wings

Figure 2.2: The Smart Rotor Blade applied on a wind turbine, showing a distribution of trailing edge flaps over the span of the rotor

the feasibility of significant blade load alleviation by applying spanwise-distributed smart load control devices through models and experiments and to provide design guidelines for smart wind rotor wind turbines (J.W. van Wingerden et al [2008]).

Chapter 3

Unsteady aerodynamics

Unsteady aerodynamics lead to unsteady aerodynamic forces, which will be determined in this research on a DU96W180 airfoil with actuated flap. This chapter describes the two main concepts in order to understand the phenomena concerned in this field of aerodynamics. The two concepts that are discussed respectively in Section 3.1 and 3.2 are vorticity dynamics and unsteady viscous effects. Both are important to understand the nature of unsteady aerodynamics. This chapter follows the most important low speed unsteady aerodynamic features according to *Aeroelasticity* [2007].

3.1 Vorticity dynamics

Dynamics of convecting vortical structures can affect the forces on nearby solid bodies. It is possible to express the vortical convection along streamlines when viscosity is neglected. To illustrate the effect of vorticity dynamics, an experiment is considered based on the theory of incompressible potential flow over an airfoil. (The concept of potential flow will be discussed in detail in Chapter 6.)

Considering incompressible potential flow over an airfoil, lift is related with its value of bound circulation. In attached flow aerodynamic theory, the value of the bound circulation is determined by the Kutta condition. This condition prevents a singularity appearing at an airfoil's sharp trailing edge. In potential flow theory there is no statement which does not allow the existence of a singularity present in the flow. In this way the solution showing zero bound circulation is valid as depicted in Figure 3.1.

Consider an airfoil in rest which impulsively is started. For a sharp trailing edge the sharp geometry will lead to velocities which tend to infinity and hence very low pressures. However on the upper surface at the stagnation point, the highest value for the pressure is obtained. This leads to an adverse pressure gradient, which might cause seperation. An illustration of the zero circulation potential flow solution is given in Figure 3.2.

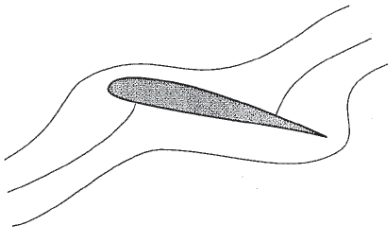

Figure 3.1: Zero circulation potential flow solution (*Aeroelasticity* [2007])

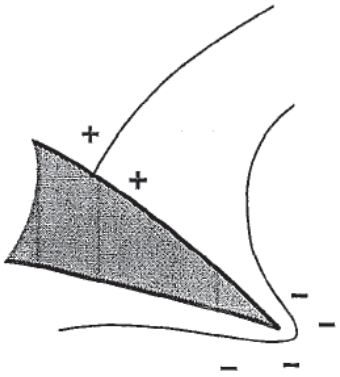

Figure 3.2: Pressure field of zero circulation potential flow solution (*Aeroelasticity* [2007])

When a positive pressure gradient is considered in Equation 3.1, the second derivative of the velocity profile in normal direction (X_1) is also positive. This type of velocity profile is characteristic for regions near separation (Figure 3.3).

$$\mu \frac{\partial^2 u_i}{\partial x_1^2} = \frac{\partial p_e}{\partial x_i} \tag{3.1}$$

Suppose this condition as shown in Figure 3.3 is sufficient to start separation at the trailing edge, leading to the formation of a vortex, known as the starting vortex depicted in Figure 3.4.

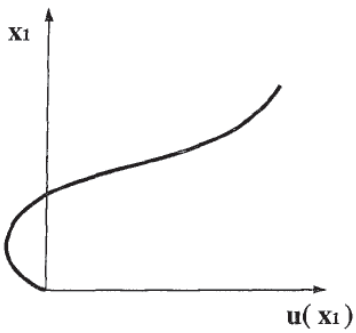

Figure 3.3: A velocity profile with $\frac{\partial^2 u_i}{\partial x_1^2} > 0$ near the wall

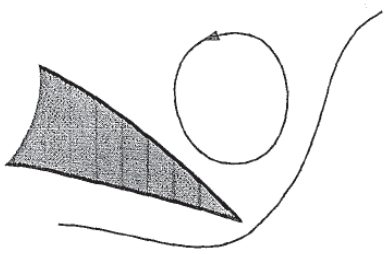

Figure 3.4: Formation of starting vortex (*Aeroelasticity* [2007])

So, once the starting vortex is formed it convects downstream with the local velocity of the flow. Kelvin's theorem states that the total vorticity within a closed contour which convects with the flow remains constant. So for a contour enclosing both the airfoil and the starting vortex, the total vorticity must be zero (value before impulsive start). Furthermore, the starting vortex has to be equal and opposite in strength with respect to the bound vortex.

The velocity field induced by the starting vortex tries to lower the local angle of attack and hence the lift at the moment of shedding the starting vortex is lower than the steady-state lift value. For the impulsive start what can be observed in time is that while the vortex convects downstream, the influence becomes less and hence the local angle of attack value is increased again. Basically what can be stated is that when the bound circulation changes, vorticity is shed. For a continuously oscillating blade the sign of the shed vorticity depends on the phase within an oscillation cycle. What to be observed is an oscillatory wake, which might induce a phase lag and magnitude change of the forces on the blade compared to steady theory. The wake vorticity also influences the wake itself and hence complex wake structures can exist.

3.2 Viscous effects

Another effect of unsteadiness in the flow is related to viscosity. Unsteady viscous effects can have a significant contribution to the flow phenomena observed. For thicker airfoils the effect of viscosity is larger than for thin airfoils. However, neglecting viscosity in simulations considering thin airfoils can give erroneous results in terms of force prediction.

An example of this viscous effect is demonstrated by returning to the discussion of the Kutta condition. The dynamics of the trailing edge seperation can be inluenced by the frequency of oscillation. At high frequencies it is possible to have a reduction in the effect of the Kutta condition via the appearance of a counter vortex near the trailing edge (Figure 3.5). In this case the change in forces can be substantially reduced. This effect is governed by the frequency, trailing edge geometry and sharpness.

Suppose the Kutta condition is satisfied, the unsteady lift can still be affected by the transient repsonse of the boundary layer over the wing. On the upper surface the boundary layer tends to increase more rapidly than the lower surface with increasing angle of attack.

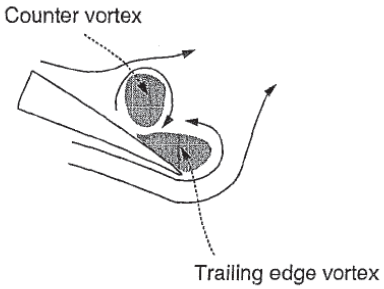

Figure 3.5: Reduction in the effectiveness of the Kutta condition (*Aeroelasticity* [2007])

Deflecting a flap enhances this effect and the airfoil becomes decambered on basis of this boundary layer. In unsteady flows, the decambering effect becomes a function of the boundary layer dynamics, which is itself different from the main flow dynamics due to the relatively low-intertia near-wall flow.

Chapter 4

Model equations for unsteady flows

In this thesis the unsteady aerodynamic forces are determined through PIV. Subsequently, the results are linked to the results of a panel method and Reynolds-Averaged Navier-Stokes equation. In order to understand the differences between the experiment and the simulations, insight is required in the simulation methods used. This chapter reviews different model equations for the prediction of unsteady aerodynamic flows. As a starting point the full Navier Stokes equations are given.

4.1 Navier-Stokes Equations

The Navier-Stokes equations model all effects in homogeneous flows which may be described as a continuum [1]. These equations express the conservation of mass, momentum and energy for a viscous compressible fluid. In integral form for a moving control volume the equations are written as,

$$\frac{d}{dt}\int_V W dV + \int_S \left(\vec{F}^i - \vec{F}^v - \dot{x}W\right)\cdot \vec{n} dS = 0 \tag{4.1}$$

where

$$W = \begin{bmatrix} \rho \\ \rho\vec{u} \\ \rho E \end{bmatrix}, \vec{F}^i = \begin{bmatrix} \rho\vec{u} \\ \rho\vec{u}\vec{u} + p\bar{\bar{I}} \\ \rho\vec{u}H \end{bmatrix}, \vec{F}^v = \begin{bmatrix} 0 \\ \bar{\bar{\tau}} \\ \bar{\bar{\tau}}\cdot\vec{u} - \vec{q} \end{bmatrix}$$

[1] Continuum theories or models explain variation as involving a gradual quantitative transition without abrupt changes or discontinuities

W is known as the state vector containing the conservative variables density, momentum and total specific energy, where $\vec{u}$ is the local fluid velocity and $E = \epsilon + \frac{1}{2}\|\vec{u}\|^2$, the sum of internal and kinetic energies. The total enthalpy H, is given by $H = E + p/\rho$, where p is the local value of pressure.

The inviscid flux vector $\vec{F}^i$, in combination with the $\dot{x}W$, expresses the transport of the conserved variables across the control surface. It includes the effect of pressure acting on this control surface on the balance of momentum within the control volume. The viscous flux vector $\vec{F}^v$, contains the effect of viscous stresses, where $\bar{\bar{\tau}}$ is denoted in Equation 4.2:

$$\tau_{ij} = \mu \left[\frac{\partial u_i}{\partial x_j} + \frac{\partial u_j}{\partial x_i} \right] + \lambda \delta_{ij} \frac{\partial u_k}{\partial x_k} \tag{4.2}$$

where μ and λ are the viscosity coefficients. These coefficients are functions of temperature, mostly determined by experiment. A complementary relation is required which relates pressure to the remaining flow variables. In most cases an ideal gas model may be used [2]. Numerical techniques are required for solving the unsteady flow problems, where the computational cost is strongly affected by the different length scales. These length scales arise form the need to represent the effect of turbulence, for which relevant length scales can be several orders of magnitude smaller than the scale of interest. There are multiple approaches to deal with this difficulty, which are listed below:

- Direct Numerical Simulation
- Large Eddy Simulation
- Reynolds-Averaged Navier-Stokes equations
- Euler equations
- Potential equations

4.2 Computational Fluid Dynamic models

The models that are addressed appear in the order of most complex to most simple model.

Direct Numerical Simulation Direct Numerical Simulation (DNS) refers to computations which try to resolve all the relevant length scales of the flow. These computations must be performed in three dimensions in order to capture the dynamics of turbulence. For low Reynolds number flows, the different length scales are limited, but by increasing the Reynolds number the expense of DNS increases rapidly.

[2] The state of an amount of gas is determined by its pressure, volume, and temperature.

Large Eddy Simulation Large Eddy Simulation (LES) makes use of a subgrid scale model to eliminate the smallest turbulence length scales from consideration, while fully simulating the dynamics of larger structures. For free turbulent flows, in which the smallest length scale can be modelled by fairly simple relations, this method works well. Wall-bounded flows prohibit the determination of the smaller length scales, due to a highly anisotropic nature of the turbulent boundary layer. In order to solve such a flow problem correctly, DNS-like resolution is required at the walls and hence the LES computations are also time costly.

Reynolds-Averaged Navier-Stokes equations Reynolds Averaged Navier Stokes equations (RANS) use the approach of decomposing the quantities of interest in the flow into mean and fluctuating components, in which the pressure can be decomposed as:

$$p(x,t) = \bar{p}(x,t) + p'(x,t) \tag{4.3}$$

where the mean value is given by averaging over a time scale, T:

$$\bar{p}(x,t) = \frac{1}{T} \int_{t}^{t+T} p(x,t)dt \tag{4.4}$$

The time scale T, must be large compared to the time scale of the turbulent fluctuations. Introducing the mean and fluctuating parts in the Navier-Stokes equation leads to the RANS equations for incompressible flows or the Favre-averaged Navier-Stokes equations for compressible flows. The RANS shows additional terms as a result of the introduction of the fluctuating components. Therefore the equation needs an additional turbulence model in order to describe the behaviour. In unsteady flows, the choice of the averaging period T is challenging, because of the difficulty of seperating the behaviour of the time scale of the turbulent fluctuations from the unsteady flow time scale itself. In this case, the time averaging technique might not be reliable and other procedures must be applied. Reynolds-averaged Navier-Stokes equations can produce useful results, however, the computational time is relatively high.

Euler equations The Euler equations can be obtained by eliminating the viscous term in Equation 4.1. The Euler equations are therefore limited to problems in which viscous effects do not significantly affect the forces and moments. In practice, attached flows can be considered. If one wants to add the effect of viscosity, the Euler solution can be corrected close to the boundaries by application of the boundary layer equations. This approach is the viscous-inviscid interaction method, used to cope with attached flows or flows with small regions of seperation. The Euler equations fully represent all of the inviscid effects associated with unsteady flow, including the convection of entropy and vorticity. The fact that vorticity dynamics are automatically included in the solution is a great advantage when considering complex wakes, or multiple wake interactions. The Euler equations are still quite costly in terms of time.

Full potential equations The full potential equation uses the Euler equation and assumes the flow to be irrotational and isentropic. The equations left form a coupled non linear system for only two unknowns. The potential equation uses a potential function, $\vec{u} = \nabla\Phi$, leaving two equations. Equation 4.5 relates the density and the potential function by using the isentropic function for a perfect gas.

$$\frac{\rho}{\rho_\infty} = \left[1 + \frac{\gamma - 1}{2a_\infty^2}\left(U_\infty^2 - 2\frac{\partial\phi}{\partial t} - |\nabla\Phi|^2\right)\right]^{\frac{1}{\gamma-1}} \tag{4.5}$$

Equation 4.6 again relates the potential function to the density by making use of the continuity equation.

$$\frac{\partial\rho}{\partial t} + \nabla\cdot(\rho\nabla\Phi) = 0 \tag{4.6}$$

Compared to the Euler equations, a considerbale simplification is obtained, resulting in an inexpensive model in terms of computational time. The assumptions used in the full potential equations have two consequences. Firstly, the assumption of isentropic flow limits the application with weak shocks. Secondly, the assumption of irrotational flow requires that vortical wakes need to be captured explicitly. In addition, the flow can be assumed to be incompressible, which is the potential flow model which is used in this thesis. A thorough discussion is given on this model in Chapter 6.

Chapter 5

Theodorsen's unsteady pitching and plunging model

The first solutions for the forces on an unsteady airfoil were produced in the 1920's by Birnbaum, Wagner and Glauert. These aerodynamicists established some analytical techniques based on series approximation, which did not converge in all cases. In 1934, Theodorsen was able to express the solution to an harmonically oscillating airfoil in terms of Hankel functions. Theodorsen's solution is still used as a simplified analysis technique for the determination of unsteady lift forces. In this chapter the solution is based on a vortex sheet model for a moving airfoil and wake. Due to the influence of convecting shed vorticity, the wake cannot be omitted in the unsteady analysis.

When derived in this chapter, this model is used to validate the panel method (Chapter 6) in unsteady conditions, which in turn is used to model the unsteady aerodynamics of the flow around a DU96W180 airfoil with actuated flap. This chapter is devoted to establish the mathematical equations for Theodorsen's theory. Section 5.1 describes the mathematical model that needs to be solved and thereby the foundation for Theodorsen's function is constructed. Section 5.2 to 5.6 describe the physical conditions that have to be satisfied in order to derive a correct solution for harmonically oscillating airfoils. In Section 5.7 an harmonic solution is used as a basis for Theodorsen's function, that is derived subsequently. In Section 5.8 the implications for this thesis are described.

5.1 Problem definition for the derivation of Theodorsen's function

The linearized equations for potential flow are given by Equations 5.1 and 5.2, where ϕ is the perturbation potential, p is the pressure, U the freestream velocity where ∞ denotes

freestream conditions. The linearized potential equations assume an irrotational, inviscid, isentropic and incompressible flow.

$$\nabla^2\phi = 0 \tag{5.1}$$

$$p - p_\infty = -\rho_\infty \left(\frac{\partial \phi}{\partial t} + U_\infty \frac{\partial \phi}{\partial x} \right) \tag{5.2}$$

Only small angles (inflow) are assumed in order to stay close to the assumption that the equation follows the linearized equation for potential flow. Furthermore, a linearized geometry is assumed as shown in Figure 5.1.

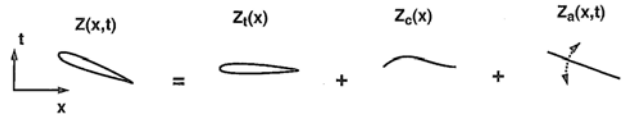

Figure 5.1: Decomposition of an unsteady airfoil problem

If the boundary conditions are also linearized, the solution of the thin-airfoil problem is split up into its thickness, camber and flat-plate components. In this case thickness and camber are not functions of time, therefore only the solution for flat plates is considered. This flat plate is subjected to zero pertubation velocity in the far-field, meaning that the pertubations vanish when considering points at infinity. Flow tangency on the airfoil surface defines the impermeability of the airfoil. No pressure jump across the wake is allowed, since a wake cannot handle a pressure difference. Finally, the Kutta condition makes sure that Kelvin's theorem is satisfied.

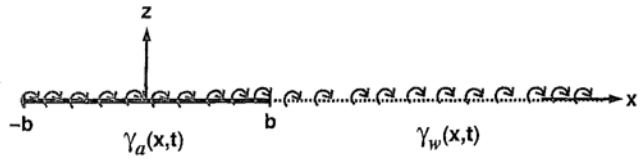

Figure 5.2: Replacement of airfoil and wake by a vortex sheet

The airfoil and the wake are represented by a sheet of vortices of unknown strength, $\gamma(x,t)$, lying on the z=0 plane as depicted in Figure 5.2. The perturbation potential induced by the complete vortex sheet is:

$$\phi(x,z) = -\int_{-b}^{\infty} \frac{\gamma(\xi)}{2\pi} \tan^{-1}\left(\frac{z}{x-\xi}\right) d\xi \tag{5.3}$$

with ξ the position of the vortex points, -b the trailing edge position and γ the strength of the vortex.

When each of the point vortices satisfies the governing equations, then the entire sheet satisfies the equations. In order to find the solution, the distribution of vortex strengths, which satisfies the boundary conditions, must be found. In order to find the solution the following conditions must be examined:

- Far-field condition
- Velocities on z=0 plane
- Flow tangency condition
- Wake pressure condition
- Kutta condition and Kelvin's theory

5.2 Far-field condition

The expression denoted in Equation 5.3 must satisfy the boundary conditions posed. Starting with the far-field perturbation, Equation 5.3 is differentiated in x and z, resulting in the two perpendicular velocity vectors,

$$u(x,z) = \phi_x(x,z) = \int_{-b}^{\infty} \frac{\gamma(\xi)}{2\pi} \left(\frac{z}{(x-\xi)^2 + z^2} \right) d\xi \tag{5.4}$$

$$w(x,z) = \phi_z(x,z) = -\int_{-b}^{\infty} \frac{\gamma(\xi)}{2\pi} \left(\frac{x-\xi}{(x-\xi)^2 + z^2} \right) d\xi \tag{5.5}$$

where ξ is the position of each individual vortex point in time and space, -b is the leading edge and ∞ is the downwind far field.

Both Equation 5.4 and 5.5 tend to zero when x and z tend to infinity.

5.3 Velocities on z=0 plane

Examining the velocities in the z=0 plane, the limit of z in Equation 5.4 is taken to 0, leaving:

$$u(x,0) = Lim_{z \to 0} \int_{-b}^{\infty} \frac{\gamma(\xi)}{2\pi} \left(\frac{z}{(x-\xi)^2 + z^2} \right) d\xi \tag{5.6}$$

$$w(x,0) = -\frac{1}{2\pi} \int_{-b}^{\infty} \left(\frac{\gamma(\xi)}{(x-\xi)} \right) d\xi \tag{5.7}$$

For $u(x,0)$ the integral vanishes except when x $\simeq \xi$, since a singularity exists in the origin of the vortex itself. In order to find an expression a small region with a width of 2 ϵ around x is considered. With $\xi' = \xi - x$:

$$u(x,0) = Lim_{z\to 0} \int_{-\varepsilon}^{+\varepsilon} \frac{\gamma(\xi')}{2\pi} \left(\frac{z}{(\xi')^2 + z^2} \right) d\xi' \tag{5.8}$$

A Taylor series expansion for $\gamma(\xi')$ is set up, leaving:

$$\gamma(x - \varepsilon \to x + \varepsilon) = \gamma(x) + O(\varepsilon) \tag{5.9}$$

Integrating and eliminating higer order terms leads to expression 5.10

$$u(x,0) = Lim_{\varepsilon\to 0} \left\{ \frac{\gamma(x) + O(\varepsilon)}{2\pi} Lim_{z\to 0} \left[\tan^{-1}\left(\frac{\varepsilon}{z}\right) - \tan^{-1}\left(\frac{-\varepsilon}{z}\right) \right] \right\} \tag{5.10}$$

Then the velocity above and below the sheet can be expressed as:

$$u(x, \pm 0) = \pm \frac{\gamma(x)}{2} \tag{5.11}$$

The jump across the vortex sheet is then:

$$\Delta u(x,0) = \gamma(x) \tag{5.12}$$

5.4 Flow tangency condition

Another boundary condition that needs to be fulfilled is the flow tangency condition. At the surface the following should hold:

$$\vec{V} \cdot \vec{n} = V_n = 0 \tag{5.13}$$

where

$$V_n = V_{n_{freestream}} + V_{n_{motion}} + V_{n_\gamma}$$

V_n consists of the freestream sheet normal-component of the freestream due to the instaneous pitch angle, the normal velocity induced by the vertical motion and the local induced normal velocity due to the vortex sheet.

The velocity components of the freestream and motion (w_{FM}) can be written as Equation 5.14, since small angle approximations are applied. In this case $V_{n_{freestream}}$ and $V_{n_{motion}}$

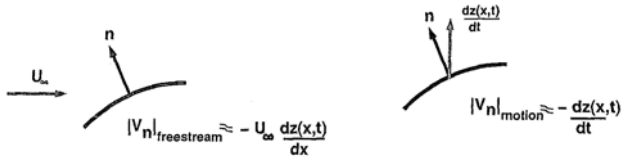

Figure 5.3: Geometric linearizations for the flow-tangency condition

can be replaced by the space and time derivative of the local z coordinate of the sheet. In addition it is assumed on basis of the small angle approximation that $w \simeq V_n$ the expression of w_{FM} is obtained.

$$w_{FM}(x,t) \approx -U_\infty \frac{dz_a(x,t)}{dx} - \frac{dz_a(x,t)}{dt} \tag{5.14}$$

The flow tangency condition can then be written as:

$$w_{FM}(x,t) + w_\gamma(x,t) = 0 \tag{5.15}$$

substitution of 5.14 into 5.15 leads to:

$$-U_\infty \frac{dz_a(x,t)}{dx} - \frac{dz_a(x,t)}{dt} - \frac{1}{2\pi}\int_{-b}^{b} \frac{\gamma_a(\xi,t)}{x-\xi} d\xi - \frac{1}{2\pi}\int_{b}^{\infty} \frac{\gamma_w(\xi,t)}{x-\xi} d\xi = 0 \tag{5.16}$$

where use is made of Equation 5.7 at the z=0 plane, to model the induced vertical velocity by airfoil (w_a) and wake(w_w).

5.5 Wake pressure condition

The wake is a free surface which will move to ensure that a pressure jump does not occur across it. The deviations of the wake in vertical direction are so small that they can be neglected while enforcing a zero-pressure-jump condition. Compared to the high forward velocities this assumption is valid. The pressure jump across the wake can be written as:

$$p_u - p_l = -\rho_\infty \left[\frac{\partial \Delta\phi}{\partial t} + U_\infty \frac{\partial \Delta\phi}{\partial x} \right] \tag{5.17}$$

where $\Delta\phi = \phi_u - \phi_l$. Rewriting in terms of γ, knowing that:

$$\frac{\partial \Delta\phi(x)}{\partial x} = \Delta u(x) = \gamma(x) \tag{5.18}$$

Substituting Equation 5.18 leads to:

$$p_u - p_l = -\rho_\infty \left[U_\infty \gamma + \frac{\partial}{\partial t} \int_{-b}^{x} \gamma(\xi) d\xi \right] \tag{5.19}$$

Where the pressure jump $p_u - p_l = 0$ for $x = b \to \infty$

5.6 Kelvin's Theorem

The assumption is that the Kutta condition is satisfied at each instant of time. A change in the airfoil condition will result in the shedding of vorticity from the trailing edge. Kelvin's theorem has to be satisfied and hence the shed vorticty is equal and opposite to the change in bound circulation over the airfoil. The equation of bound vorticity over the airfoil reads:

$$\Gamma(t) = \int_{-b}^{b} \gamma_a(\xi, t)\, d\xi \tag{5.20}$$

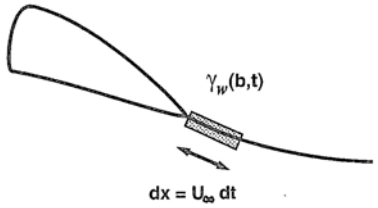

Figure 5.4: Shed vorticity form the trailing edge

An increment of shed vorticity from the trailing edge in terms of $\Gamma(t)$ (Figure 5.4) can be expressed as:

$$\gamma_w(b,t)dx = -\frac{d\Gamma(t)}{dt}dt \tag{5.21}$$

For infinitesimal time and space intervals, the final expression for the instantaneous shed vorticity at the trailing edge yields:

$$\gamma_w(b,t) = -\frac{1}{U_\infty}\frac{d\Gamma(t)}{dt} \tag{5.22}$$

5.7 Harmonic solutions

In the case of an harmonic excitation with the wake vorticity convected with the freestream velocity U_∞, the wake pressure condition is also satisfied. The assumption for harmonic forms for the airfoil excitation and solution is:

$$w_{FM}(x,t) = \hat{w}_{FM}(x)e^{i\omega t} \tag{5.23}$$

$$\gamma_a(x,t) = \hat{\gamma}_a(x,t)e^{i\omega t} \tag{5.24}$$

$$\Gamma(t) = \hat{\Gamma}e^{i\omega t} \tag{5.25}$$

An harmonic response in the wake is also assumed:

$$\gamma_w(x,t) = \hat{\gamma}_w(x,t)e^{i\omega t} \tag{5.26}$$

Kelvin's theorem can then be expressed as:

$$\hat{\gamma}_w(b) = -\frac{iw}{U_\infty}\hat{\Gamma} \tag{5.27}$$

Assuming downstream convection of vorticity with U_∞, the complex coefficient of the wake circulation distribution is then written as:

$$\hat{\gamma}_w(x) = -\frac{i\omega}{U_\infty}\hat{\Gamma}e^{\frac{iw}{U_\infty}(b-x)} \tag{5.28}$$

Substituting these expressions into the wake pressure condition (Equation 5.19) by making use of Equation 5.20, the second term of Equation 5.19 can then be written as:

$$\frac{\partial}{\partial t}\int_{-b}^{x}\gamma(\xi)d\xi = \frac{d\Gamma}{dt} + \frac{\partial}{\partial t}\int_{b}^{x}\gamma_w(\xi)\,d\xi = \left(i\omega\hat{\Gamma} + i\omega\int_{b}^{x}\hat{\gamma}_w(\xi)d\xi\right)e^{i\omega t} \tag{5.29}$$

The expression for $\hat{\gamma}_w(\xi)$ given by Kelvin's theorem can be substituted in equation 5.29:

$$\int_{b}^{x}\hat{\gamma}_w(\xi)d\xi = -\frac{i\omega\hat{\Gamma}}{U_\infty}\int_{b}^{x}e^{\frac{i\omega}{U_\infty}(b-\xi)}d\xi \tag{5.30}$$

The expression for flow tangency (Equation 5.16) rewritten with Equation 5.28 leads to an expression for a harmonically oscillating airfoil:

$$-\frac{1}{2\pi}\int_{-b}^{b}\frac{\hat{\gamma}_a(\xi)}{x-\xi}d\xi + \frac{i\omega}{2\pi U_\infty}\hat{\Gamma}\int_{b}^{\infty}\frac{e^{i\omega\left(\frac{b-\xi}{U_\infty}\right)}}{x-\xi}d\xi = i\omega\hat{z}_a(x) + U_\infty\frac{\partial\hat{z_a}(x)}{\partial x} \tag{5.31}$$

The integral equation has been solved for $\hat{\Gamma_a}$ by Theodorsen and Schwartz, with $\hat{za}(x)$ for a harmonically oscillating flat plate. Solutions of this integral are expressed in terms of Theodorsen's function, where the reduced frequency $k = \frac{\omega b}{U_\infty}$, describing the unsteadiness of the flow.

$$C(k) = F(k) + iG(k) = \frac{H_1^{(2)}(k)}{H_1^{(2)}(k) + iH_0^{(2)}(k)} \tag{5.32}$$

Figure 5.5 shows Theodorsen's function in a complex plane, showing the effect of unsteadiness on the real part (amplitude) and imaginary part (phase) of Theoodorsen's function.

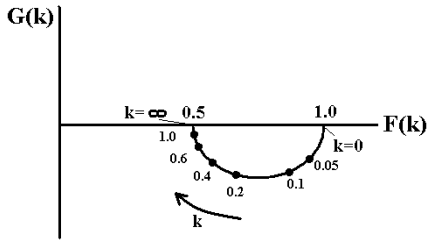

Figure 5.5: Components of Theodorsen's function C(k)=F(k)+iG(k)

$H_n^{(2)}$ are Hankel functions of the second kind. The parameter $k \equiv (\omega b)/U_{infty}$ is the reduced frequency, describing the ratio of periods for oscillation and wake convection.

The lift and nose up moment can be expressed in the form as depicted in equation 5.33 and 5.34.

$$L = \hat{L}e^{i\omega t} = \pi\rho_\infty b^2 \left[\ddot{h} + U_\infty\dot{\theta} - ba\ddot{\theta}\right] + 2\pi\rho_\infty U_\infty bC(k)\left[\dot{h} + U_\infty\theta - b\left(\frac{1}{2} - a\right)\dot{\theta}\right] \tag{5.33}$$

$$\begin{aligned} M = Me^{i\omega t} &= \pi\rho_\infty b^2\left[ba\ddot{h} - U_\infty b\left(\tfrac{1}{2} - a\right)\dot{\theta} - b^2\left(\tfrac{1}{8} + a^2\right)\ddot{\theta}\right] \\ &+2\pi\rho_\infty U_\infty b^2\left(\tfrac{1}{2} + a\right)C(k)\left[\dot{h} - U_\infty\theta - b\left(\tfrac{1}{2} - a\right)\dot{\theta}\right] \end{aligned} \tag{5.34}$$

The first term in the lift and moment equation are known as the non-circulatory component, whereas the second group is refered as the circulatory component due to the fact that they arise because of the satisfaction of the Kutta condition. The circulatory component is a function of the instantaneous vertical velocity at 3/4 chord position $w_{frac34c} = [\dot{h} + U_\infty\theta + b(\frac{1}{2} - a)\hat{\theta}]$.The non circulatory components are referred as apparent mass terms, as they are proportional to accelerations felt by a fluid cylinder with radius b. With $k = 0$, $C(k) = 1$ the steady flat-plate solution is recovered. Figure 5.6 illustrates the variables used in Equations 5.33 and 5.34.

5.8 Theodorsen's foundation for unsteady aerodynamics

The physical considerations treated by Theodorsen, give an insight in unsteady aerodynamic theory. Firstly, the reduced frequency k is measure, describing the ratio of periods for oscillation and wake convection. In this way it defines the unsteadiness for harmonically oscillating airfoils. The drive behind vortical convection is Kelvin's theorem in

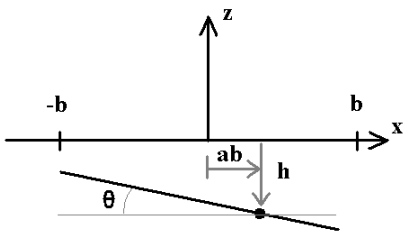

Figure 5.6: Definition of the variables for the flat plate solution

combination with the Kutta condition. A change in the airfoil condition at a certain instant of time, will result in shedding of vorticity from the trailing edge. This vorticity shed shows its influence on the forces on the flat plate. In combination with the unsteadiness level k, Theodorsen's function is a powerful tool defining the phase lag and amplitude of the force for a certain unsteadiness level k. Thereby Theodorsen's function quantifies the influence of the vorticity dynamics for oscillating airfoils, of which a qualitative desription is given in Chapter 3. Although this function is especially written for a plunging and/or pitching airfoil, it also gives an insight in the unsteady aerodynamics created by an actuated flap as presented in this thesis. The physcial considerations of shedding vorticity, when a change in the airfoil condition is felt, also holds for an oscillating flap. The shedding of vorticity is in this case governed by the motion of the flap.

Chapter 6

Panel method

The fundamental equations for the development of a panel method are described in this chapter. The method presented is based on the surface distribution of singularity elements. A solution must be found for the distribution of strength of the different singularity elements. In this way, an economical approach is obtained, which does not have to evaluate the entire flow domain for capturing the force on the body. However, this method only holds for inviscid incompressible flows. The methodologies of the panel code presented in this chapter are based on J. Katz et al [2001] and Dixon [2008].

Section 6.1 describes the general mathematical model for the potential flow simulation. Thereafter the aspect of vorticity is presented in Section 6.2. Section 6.3 gives a short overview of the circulation as applied in the method. In Section 6.4 all boundary conditions are described which are necessary to solve the equations for potential flow. Therafter, Section 6.5 describes the elementary flow models that can be used as building blocks for the panel method solution. These elements are combined to build the actual panel model in Section 6.6. Section 6.7 finalizes by a short discussion on the kutta condition.

6.1 The Laplace Equation and the Velocity Potential

The Navier-Stokes equations (Chapter 4) can be simplified reducing the computational effort. For low subsonic speeds, meaning Mach number below 0.3 and a Reynolds number in the range of 10^5 and 10^6, the flow may be assumed to be incompressible, adiabatic and inviscid. Only the boundary layer includes frictional effects which should be treated as discussed in Chapter 4 in order to reflect the physics of this phenomenon. The assumption of incompressible, adiabatic and inviscid flow reduces the set of the N-S equations, leading to the Euler equations as described in Chapter 4:

$$\nabla \cdot q = 0 \tag{6.1}$$

$$\frac{\partial \vec{q}}{\partial t} + \vec{q} \cdot \nabla \vec{q} = \vec{f} - \frac{\nabla p}{\rho} \tag{6.2}$$

,

where q is the local velocity, f is the bodyforce and p is the pressure.

Equation 6.1 defines how boundary information is communicated throughout the flow domain. Since the fluid is incompressible this continuity equation transfers the information through the domain at an infinite speed. Due to this assumption of incompressibility, a change in the boundary condition in time, allows for an instantaneous solution. Therefore, time dependent boundary conditions enforce time dependent solutions, while not explicitly containing time dependent terms.

The velocity field can be represented by a scalar potential, known as the velocity potential. Using this concept, the Laplace equation is introduced, thereby rewriting Equation 6.1:

$$q = \nabla \Phi \tag{6.3}$$

$$\nabla^2 \Phi = 0 \tag{6.4}$$

Equation 6.2 gives the relationship between the local fluid pressure and the velocity. Hence this equation can be used for determining the lift, drag and moment on a surface. Basically the local fluid pressure is a function of the local velocity and its derivative.

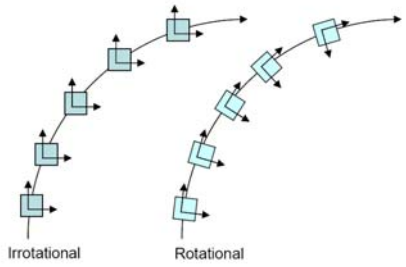

Figure 6.1: Irrotational versus rotational (Dixon [2008])

By posing the assumption that the flow is inviscid, meaning that no friction is present in the domain, the flow must be 'irrotational' (Figure 6.1), setting the curl of the local velocity field equal to zero:

$$\nabla \times \vec{q} = 0 \tag{6.5}$$

This equation contains the fact that the orientation of fluid particles cannot change due to the absence of shear stresses.

6.2 Vorticity

For modelling unsteady behaviour, purely irrotational flow is an invalid assumption, leading to unphysical results lacking the effect of viscosity and thereby vorticity. Viscosity drives the friction between infinitesimal volumes of air which introduces a rotation of these volumes of air driven by the tangential components acting on these volumes. By neglecting the local rotations, known as vorticity (local rotational rate), no forces will act on the body and an unphysical situation is obtained. The concept which respresents this local rotational field is known as vorticity and is defined in 6.6. Lacking the tangential friction component, means that only forces in the normal direction are valid. In this situation drag and lift cannot exist. However, if this effect of the tangential component, known as vorticity, is introduced in the flow domain, forces can actually exist.

Lift can only be produced by allowing vorticity at singular points, which are excluded from the computational domain, but do have their influence on the flow. Knowing this, the vortex singularities need to be modelled, such that the equations of potential flow hold everywhere except at these singularities. So the concept of irrotationality is still valid, whereas the physical features of friction are introduced by means of this 'artificial' vorticity.

$$\vec{\varsigma} = \nabla \times \vec{q} \tag{6.6}$$

6.2.1 Transport of Vorticity

With the concept of vorticity it is not possible within the Euler equation to create, destruct or diffuse vorticity. Though, the transport of vorticity is possible and hence vortices convect with the flow. Application of the curl operator to Equation 6.2 gives the following:

$$\frac{D\vec{\varsigma}}{Dt} = \frac{\partial \vec{\varsigma}}{\partial t} + \vec{q} \cdot \nabla \vec{\varsigma} = \vec{\varsigma} \cdot \nabla \vec{q} \tag{6.7}$$

In two dimensional flows, the gradient of the vorticity is perpendicular to the vorticity and hence Equation 6.6 can be written as Equation 6.8.

$$\frac{D\vec{\varsigma}}{Dt} = 0 \tag{6.8}$$

Equation 6.8 implies that the total amount of vorticity is conserved.

6.3 Circulation

Circulation is defined as the sum of the local velocity along a closed path in a two dimensional flow. For undisturbed ideal fluids which exclude the circumscription around a rotational singularity, this quantity should be zero. Vorticity is related to circulation by Stokes' theorem:

$$\Gamma \equiv \oint_C \vec{q} \cdot dl = \int_S \vec{\varsigma} \cdot \hat{n} dS = \int_S \nabla \times \vec{q} \cdot \hat{n} dS \tag{6.9}$$

As discussed, potential flow alone cannot produce net forces on two dimensional objects. Circulation must be part of the description in order to resemble physical phenomenon. A new condition has to be setup in order to relate lift to circulation. Kutta and Joukowsky indepently arrived at the proportionality (J. Katz et al [2001]) as described in Equation 6.10:

$$L = \rho U_\infty \Gamma \tag{6.10}$$

This result in combination with the Kutta condition, which will be described in Section 6.7, provides a way to solve for the amount of circulation around a given body.

Another important parameter is the time rate of change of the circulation, by taking the substantive derivative of the circulation:

$$\frac{D\Gamma}{Dt} = \frac{D}{Dt} \oint_C \vec{q} \cdot dl = \oint_C \frac{D\vec{q}}{Dt} \cdot d\vec{l} + \oint_C \vec{q} \cdot \frac{D}{Dt} d\vec{l} \tag{6.11}$$

Substituting Equation 6.12 and Equation 6.13 into Equation 6.11 and setting the last term to zero, because the integral of an exact differential around a closed path is zero, the following is obtained as denoted in Equation 6.14:

$$\frac{D\vec{q}}{Dt} = \vec{a} = -\nabla \left(\frac{p}{\rho} \right) + \vec{f} \tag{6.12}$$

$$\frac{D}{Dt} d\vec{l} = d\vec{q} \tag{6.13}$$

$$\frac{D\Gamma}{Dt} = -\oint_C d\left(\frac{p}{\rho} \right) + \oint_C \vec{f} \cdot d\vec{l} \tag{6.14}$$

Since the flow is incompressible the density is constant and can be taken out of the integral leaving an exact intergral over dp, giving zero. The second term, f which is gravity, evaluated on a closed contour will also be zero, leaving:

$$\frac{D\Gamma}{Dt} = 0 \tag{6.15}$$

Equation 6.15 is Kelvin's theorem, stating that for incompressible, inviscid and irrotational flows, the time rate of change of circulation is zero. At any moment the total amount of circulation in the domain stays constant. Conservation of circulation, Kelvin's theorem implies that when an airfoil in rest suddenly accelerates, circulation is generated. In order to be conservative with Kelvin's theorem, this circulation must be counteracted by an equally large circulation with opposite sign, namely the starting vortex.

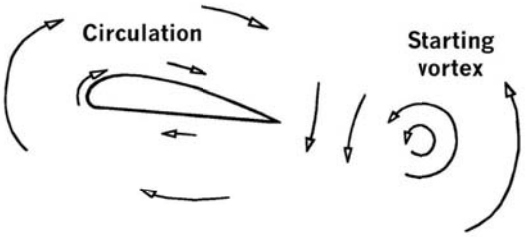

Figure 6.2: Starting vortex shed by 2D airfoil (Dixon [2008])

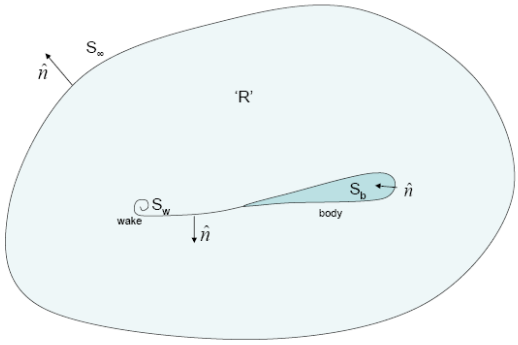

Figure 6.3: The solution domain

6.4 Domain and Boundary Conditions

Equation 6.4 is solved on a computational region R (Figure 6.3). As described in Section 6.2, singular points are not part of this computational domain. However, the singularities do influence the region R. On basis of these singularities (sources, sinks and vortices) the body and wake can be constructed. By excluding the singularities form the domain, the velocity potential in region R satisfies the Laplace equation. This mechanism is used for the construction of panel methods. The assumption that the flow is inviscid means that the 'no-slip' condition cannot exist, hence there cannot be a boundary layer in potential flow. Since air cannot flow through surfaces only tangential velocities exist at the boundaries, so the normal component to the surface is zero. The velocity at the surface exists out of the induced velocity due to body and wake and the local kinematic velocity stemming from translation, $\vec{V}_{origin}$ deformation $\vec{v}_{rel}$, and rotation $\vec{\Omega} \times \vec{r}$.

Equation 6.16 only holds for the condition at the surface of the airfoil.

$$\frac{\partial \Phi}{\partial n} + \left(\vec{V}_{origin} + \vec{v}_{rel} + \vec{\Omega} \times \vec{r}\right) \cdot \vec{n} = 0 \tag{6.16}$$

$$\nabla \Phi_{\infty} = 0 \tag{6.17}$$

In a fixed frame of reference, the fluid is initially at rest and should remain in this condition at an infinte distance from the moving surface. This boundary condition should apply for

all singular solutions, i.e. the perturbation should go to zero at infinity. In order to have a unique solution a secondary assumption has to be made throughout the observations of physics, the Kutta condition.

6.5 Singular Solutions to the Laplace Equation

Different singular solutions can be used which all satisfy the Laplace equation. The elementary flow elements used are the source,the sink,the doublet and the vortex. In this section the mathematical models of these elements will be described.

6.5.1 Source, sink and doublet

One of the solutions to the Laplace equation is the source/sink. The potential of this singular element, placed at the origin of a spherical coordinate system is:

$$\Phi = -\frac{\sigma}{4\pi r} \tag{6.18}$$

Using the ∇-operator, the velocity $\vec{q}$ due to this element is obtained as:

$$\vec{q} = -\frac{\sigma}{4\pi}\nabla\left(\frac{1}{r}\right) = \frac{\sigma}{4\pi}\frac{\vec{e_r}}{r^2} = \frac{\sigma}{4\pi}\frac{\vec{r}}{r^3} \tag{6.19}$$

Which, in spherical coordinates, is

$$q_{(r,\theta,\varphi)} = \left(\frac{\sigma}{4\pi r^2}, 0, 0\right) \tag{6.20}$$

Observation of this formula shows that fluid is emanating from this source when σ is positive and fluid is absorbed by the sink when σ is negative. These two singularities can be added together forming a doublet. In Figure 6.4 the source and the doublet are shown.

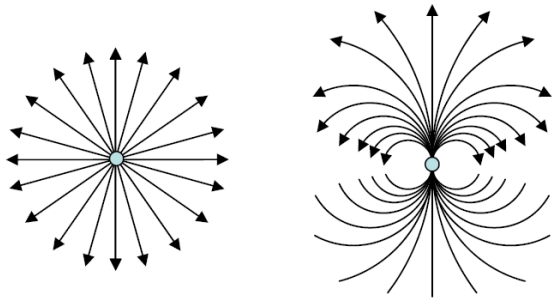

Figure 6.4: Point source and doublet where the arrows indicate the direction of velocity emanating from the singularity at the origin

This addition is possible due to the linear character of the Laplace equation. The velocity $\vec{q}$ and potential Φ induced by a doublet of strength μ are:

$$\Phi = -\frac{\vec{\mu} \cdot \vec{r}}{4\pi r^3} \tag{6.21}$$

$$q_{(r,\theta,\varphi)} = \left(\frac{\mu \cos\theta}{2\pi r^3}, \frac{\mu \sin\theta}{4\pi r^3}, 0 \right) \tag{6.22}$$

These elements can be distributed over lines, surfaces or volumes forming complex geomtries. Strengths can vary from point to point and can take any order of distribution. In Figure 6.5 a 2D constant source panel is depicted, showing the distribution of multiple sources over a panel.

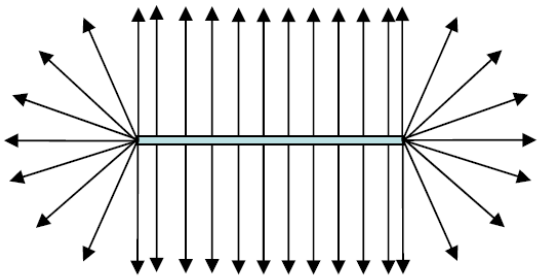

Figure 6.5: 2D constant source panel

In Figure 6.6 the velocity profile of a distribution of doublets over a panel is illustrated.

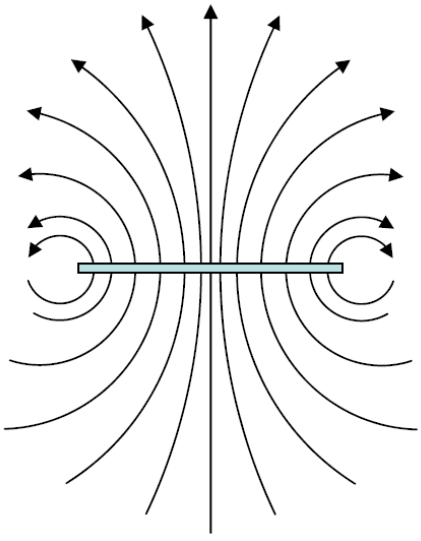

Figure 6.6: 2D constant doublet panel

6.5.2 The vortex

Other than doublets, sources and sinks, another singularity is a vortex, where only the tangential component exists and is decaying in the same sense as the source (with the inverse of radius). The velocity components are:

$$q_{(r,\theta,\varphi)} = \left(0, \frac{-\Gamma}{2\pi r}, 0\right) \tag{6.23}$$

6.6 General Solution of the Laplace Equation

Having the building blocks, the Laplace equation can be solved over an arbitrary geometry, representing a body submerged in a flow, and hence the flow properties can be calculated at any point. The solution method is based on method presented in J. Katz et al [2001].

The surface integral is taken over all the boundaries S as depicted in Figure 6.3:

$$S = S_B + S_W + S_\infty \tag{6.24}$$

Where S_B is the boundary surrounding the body, S_W is the boundary for the wake and S_∞ is the boundary at infinity.

Now assume that Φ_1 and Φ_2 are solutions to the Laplace equation. Taking these solutions and forming the vector quantity, $\Phi_1 \nabla\Phi_2 - \Phi_2 \nabla\Phi_1$ and then applying the divergence theorem gives:

$$\int_S (\Phi_1 \nabla\Phi_2 - \Phi_2 \nabla\Phi_1) \cdot \hat{n} dS = \int_V \left(\Phi_1 \nabla^2\Phi_2 - \Phi_2 \nabla^2\Phi_1\right) dV \tag{6.25}$$

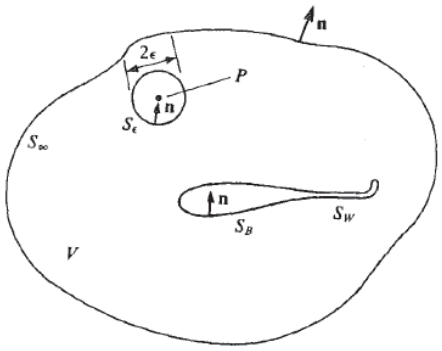

Figure 6.7: Domain with indication of the singularity element P

With the general thought that the flow elements have a solution to the Laplace equation everywhere except for the origin, it can be concluded, that the elements itself need to

be excluded from the solution domain. Φ_1 and Φ_2 are solutions to the Laplace equation hence the right hand side of Equation 6.25 is zero. Setting $\Phi_1 = \frac{1}{r}$ (because this is one fundamental solution to the Laplace equation) and $\Phi_2 = \Phi$. Φ is the potential of the flow of interest in V and r is the distance from a point P(x,y,z), the position of the flow element, as shown in Figure 6.7. Φ_1 is the potential of a source and is unbounded as P is approached and $r \to 0$. If P is outside V, Φ_1 and Φ_2, the Laplace equation is satisfied and Equation 6.25 becomes Equation 6.27.

$$\int_S \left(\frac{1}{r}\nabla\Phi - \Phi\nabla\frac{1}{r}\right) \cdot \hat{n} dS = 0 \tag{6.26}$$

When point P is inside the region a different approach is needed. Point P is introduced in the domain circumferenced by a sphere of radius ϵ, creating a subdomain. Outside of this subdomain and inside region V, the potential Φ_1 satisfies the Laplace equation ($\nabla^2(1/r) = 0$). Similarly $\nabla^2\Phi_2 = 0$ and Equation 6.25 becomes:

$$\int_{S+sphere\epsilon} \left(\frac{1}{r}\nabla\Phi - \Phi\nabla\frac{1}{r}\right) \cdot \hat{n} dS = 0 \tag{6.27}$$

The domains are additive and hence two integrals can be written over the two domains. Spherical coordinates are introduced for the small domain, leaving:

$$-\int_{S_{sphere}} \left(\frac{1}{r}\frac{\partial\Phi}{\partial r} - \frac{\Phi}{r^2}\right) dS + \int_S \left(\frac{1}{r}\nabla\Phi - \Phi\nabla\frac{1}{r}\right) \cdot \hat{n} dS = 0 \tag{6.28}$$

Let the radius of the sphere go to zero, then the sphere integral is reduced to $4\pi\Phi(x)$ and 6.6 becomes:

$$\Phi(x) = \frac{1}{4\pi}\int_S \left(\frac{1}{r}\nabla\Phi - \Phi\nabla\frac{1}{r}\right) \cdot \hat{n} dS \tag{6.29}$$

If point P lies on the surface of the body, then Equation 6.29 is divided by 2π instead of 4π which is representative of a surface integral over a hemisphere as opposed to a full sphere.

Observing Equation 6.29 one can see that for calculating all flow properties only the velocity potential and its normal derivative on the surface are necessary, making it a powerful tool for evaluation. The panel method therefor significantly saves computational cost compared to methods where it is required to compute the solution over the entire domain.

In order to solve the potential equation boundary conditions have to be set. There are two distinct ways of describing the boundary condition:

1. *Dirichlet problem*
2. *Neumann problem*

For the Dirichlet problem the internal potential is specified at the boundary. This concept can be used when thickness is significant. For the Neumann concept the derivative of the potential, the velocity, is prescribed at the boundary pointing in the normal direction of the boundary.

Practically both, conditions can apply to the same simulation, however the majority of panel codes use the combination of the source doublet formulation in combination with the Dirichlet boundary condition, because of stability of the solution. For other approaches the reader is referred to J. Katz et al [2001].

6.6.1 Source Doublet Formulation

Now consider a situation when the flow of interest occurs inside the boundary of S_b and the resulting internal potential is ϕ_i. For this flow the point P (which is in the region V) is exterior to S_b, thereby Equation 6.29 becomes:

$$\int_S \left(\frac{1}{r}\nabla\Phi_i - \Phi_i\nabla\frac{1}{r}\right)\cdot\hat{n}dS = 0 \tag{6.30}$$

If we then add this result to Equation 6.29 when considering the region external to the body, we are left with the following (where 'i' represents internal quantities).

$$\Phi(x) = \frac{1}{4\pi}\int_{S_B}\left(\frac{1}{r}\nabla(\Phi-\Phi_i) - (\Phi-\Phi_i)\nabla\frac{1}{r}\right)\cdot\hat{n}dS - \frac{1}{4\pi}\int_{S_W}\left(\Phi\nabla\frac{1}{r}\right)\cdot\hat{n}dS + \Phi_\infty(x) \tag{6.31}$$

If we then set μ to be equal to the potential jump across the boundary, and σ to be the jump in normal velocity,

$$-\mu = \Phi - \Phi_i \tag{6.32}$$

,

$$-\sigma = \frac{\partial\Phi}{\partial n} - \frac{\partial\Phi_i}{\partial n} \tag{6.33}$$

the well known Source-Doublet formulation is produced:

$$\Phi(x) = \frac{1}{4\pi}\int_{S_B}\left[\sigma\frac{1}{r} - \mu\frac{\partial}{\partial n}\left(\frac{1}{r}\right)\right]dS + \frac{1}{4\pi}\int_{S_W}\left[\mu\frac{\partial}{\partial n}\left(\frac{1}{r}\right)\right]dS + \Phi_\infty(x) \tag{6.34}$$

The fundamental problem is then to find an appropriate combination of sources and doublets that satisfies Equation 6.34. Non-lifting flows can be solved by simply setting the doublet terms to zero and solving for the appropriate source terms- likewise, thin airfoil applications (sails, slender wings) can be solved by setting the source terms to zero and finding the appropriate doublet terms.

In applications where the geometry has appreciable thickness and generates lift, both

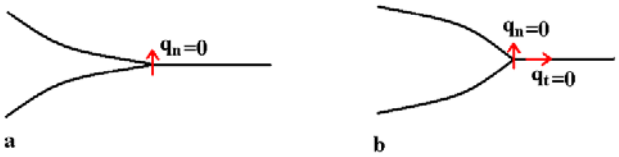

Figure 6.8: (a) A cusp trailing edge (b) A finite trailing edge

source and doublet terms must be used to obtain an accurate solution. In this case there are many distributions which will satisfy Equation 6.34. An extra condition must be imposed in order to find a unique solution that is representative of physical flows- This is known as the 'Kutta Condition'.

6.7 The Trailing Edge Kutta Condition

The Kutta Condition requires that the flow leaves the TE smoothly and continuously. Furthermore it secures that the velocity there is finite. The consequences for the flow depend on the geometry of the modeled airfoil. If the trailing edge has a finite angle as depicted in Figure 6.8 (b), the normal and tangential component of the velocity must be zero. This results in a stagnation point. If the trailing edge is represented by a cusp (Figure 6.8 (a)), the edge point does not necessarily need to be a stagnation point. A finite tangential velocity can exist but the no normal component is set to 0. In general, there should exist no pressure difference between the upper and lower surface at the trailing edge and no pressure difference over the wake surface.

Implementation of the Kutta condition depends on the model scheme used. In case of a doublet source formulation, the doublet strength at the trailing edge is set to zero. By posing this condition to zero, the strength of the shed wake is determined by this Kutta condition. Doublet/Vortex singularities are responsible for turning the flow. It follows that there can be no local turning at the trailing edge while keeping the velocity finite. This states that the local circulation at the trailing edge must be zero as denoted in Equation 6.35. A sharp trailing edge is a region of infinite curvature, and for the flow to move around such a geometry would require infinite velocity which is clearly non-physical.

$$\gamma_{TrailingEdge} = 0 \tag{6.35}$$

Chapter 7

General considerations on experimental aerodynamics

This chapter describes the main considerations in experimental aerodynamics. Section 7.1 gives an overview on the advantages of experimental aerodynamics versus a numerical and theoretical approach. Section 7.2 describes the terminology *accuracy* and *precision* and the associated errors with these two terms. Section 7.3 gives an overview of the common errors in experimental aerodynamics. Finally, Section 7.4 is devoted on a short discussion on spatial and temporal resolution concerning experiments.

7.1 Three methodolgies for determining aerodynamic performance

Several means of analysis exist to determine the aerodynamic performance of some interaction of a body with a fluid: experimental, theoretical and numerical. Through the years all the methods are developed and applied in the above order. The methods are complementary and usually the best result is obtained by combining the three methods. Individually, the methods show advantages and disadvantages which are summarized in Table 7.1.

7.2 Measurement errors

Every quantity measured in an experiment has an uncertainty, which is expressed as the error ϵ. The measurement accuracy is defined as the complementary to 1 or 100 % of the absolute difference of the measured value M_G and the actual value V_G divided by the full range value of the measurement system. The accuracy of a system is evaluated through the calibration of the system, where M_G and A_c are compared to capture this uncertainty.

	Experimental	Theoretical	Numerical
Advantages	Deals with real flows Accuracy High Reynolds Number Turbulent flow	Exact solution Boundary conditions	Easy variation of parameters Boundary conditions Seperate effects and phenomena Time required and costs
Disadvantages	Experimental errors Similarity hypothesis Limited test ranges Boundary conditions Time required and costs	Specified conditions Simplified equations Very simple geometries	Numerical errors Low Reynolds numbers Turbulence properties Mathematical models

Table 7.1: The advantages and disadvantages of the experimental approach versus the theoretical and numerical approach, as taken from *Experimental Aerodynamics* [2007]

$$M_G = V_G \pm \epsilon \tag{7.1}$$

The accuracy can be calculated by:

$$Accuracy \equiv 1 - (|M_G - V_G|/V_{GMAX}) = 1 - |\epsilon|/V_{GMAX}) = 1 - |\epsilon_r| \tag{7.2}$$

,

where ϵ_r represents the relative measurement error.

In general two types of error exist:

- Systematic errors
- Random errors

"Systematic errors are difficult to detect, since the deviation shows a constant offset compared to the real value. Random errors appear as random deviations of the measured value due to imperfections in the measurement chain." *Experimental Aerodynamics* [2007]

The term precision is generally related to the random error, where the accuracy is given by the precision minus the bias errors, which makes the accuracy always smaller than the precision.

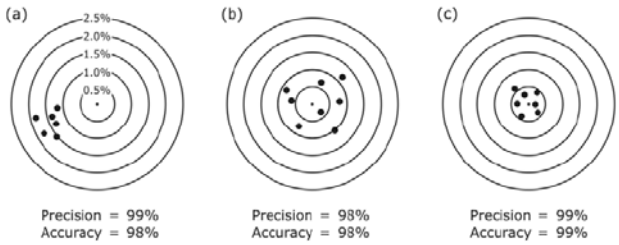

Figure 7.1: Cases showing the concept of accuracy and precision

In Figure 7.1 shows case (a) showing a high precision since the dots are clustered relatively close together. Case (b) shows a cluster of dots scattered around the actual solution, showing relatively low precision and thereby also low accuracy. Case (c) is clustered around the actual value with high precision and high accuracy.

The random error can be split into a maximum error and a statistical error, where the maximum error can be described as:

A maximum error is introduced when even in presence of the fluctuation of the quantity to be measured, the instrument alwyas returns the same value

and the statistical error can be described as:

A statistical error is introduced because of the intrinsic variation of the quantity to be measured. Such variation may be caused by fluctuations of the quantity. The variations show a mean M_G and a standard deviation σ_G:

$$\bar{M_G} = \frac{1}{N} \sum_{n=1}^{N} M_{G_n} \tag{7.3}$$

$$\sigma_G = \left[\frac{1}{N} \sum_{n=1}^{N} \left(M_{G_n} - \bar{M_G} \right)^2 \right]^{1/2} \tag{7.4}$$

Equation 7.4 describes the statistical error. If a Gaussian distribution is used, the measured values occur within an interval of $[-3\sigma_G + 3\sigma_G]$,

The measurement accuracy increases with the number of observations N:

$$\bar{M_G} = V_G \pm \frac{\sigma_G}{2\sqrt{N}} \tag{7.5}$$

The errors described are only valid in the case that the quantity of interest is measured directly. If a quantity is derived from a measured quantity the error propagation mechanism is needed. For a discussion of this mechanism the, reader is referred to *Experimental Aerodynamics* [2007].

7.3 Typical errors in experimental aerodynamics

There are three general errors concerned in the execution of a windtunnel experiment: flow facility related errors, errors due to measurement instruments and fluctuations due to turbulence and statistical errors.

Flow facility related errors stem from the fact that experiments are conducted in a limited environment, such as a wind tunnel. Due to the presence of model supports, undesired variations of flow quantities (pressure, temperature and velocity), presence of wall (boundary layer growth) and their interference with the model (blockage). These errors

are usually of systematic nature, sometimes they can be of the random type. This is the case considering turbulent fluctuations present in the wake.

Every measurement instrument has a specific precision depending on the physical principle of the measurement method. Also the procedure for capturing the desired quantities determines the precision. In order to determine what the precision is a calibration is required. Calibration errors can also exist due to geometrical, electrical or optical quantities that are required for the determination of the calibration parameters. Furthermore errors due to the transition from analog to digital (A/D) exist or the use of filters in a Data Acquisition System. Furthermore noise is a common error present in all types of measurement systems. This error is referred to be a statistical error.

Fluctuations due to turbulence and statistical errors exist even if systematic and random errors are not present. The fluctuations are present in the flow and the determination is one of the objectives of the measurement campaign.

7.4 Measurement spatial and temporal resolution

The measurement instrument directly interacts with the physical quantity to be measured, which is the sensitive element of the device. The region where it extracts the data from the flow is the measurement volume V_M. The measurement is performed within a certain time, referred to be the measurement time T_M. These two parameters define the measurement system in terms of precision in spatial and temporal resolution. The measurement volume defines the lower limit of the spatial fluctuations to be measured, where the measurement time defines the shortest time interval for a quantity to be measured. If turbulent fluctuations are strongly evolving, a relatively high spatial and temporal resolution are required to capture the physics. If the flow can be considered as steady lower resolution in both space and time will suffice.

Chapter 8

Particle Image Velocimetry

Particle Image Velocimetry (PIV) is a measurement technique which can determine the velocity vectors over an entire flow domain instantaneously on basis of the illumination of tracer particles. In this chapter the basic procedure is described for acquiring PIV images adressing flow seeding techniques, illumination of the flow, imaging optics and postprocess techniques. This chapter is formed on basis of the theory described in Markus Raffel et al [2007] and *Experimental Aerodynamics* [2007].

Section 8.1 shows the basics of Particle Image Velocimetry and describes why Particle Image Velocimetry is a promising technique. On basis of this general outline, flow seeding techniques are introduced in Section 8.2, describing the demands on the seeding of particles to the flow, which is key in performing proper PIV measurements. Section 8.3 considers the technique to illuminate the particles, which are seeded to the flow. Section 8.4 describes the optical conditions for capturing the particles in focus on an image. Section 8.5 describes the concept of seeding density. Thereafter, Section 8.6 describes the principle of digital cameras and finally the interpretation of the images is discussed on basis of the explanation of postprcocess techniques in combination with optimization criteria in Section 8.7 and 8.8.

8.1 General outline of PIV

Particle Image Velocimetry is a measurement technique which allows for rapidly capturing velocity information. This technique has its roots already in the beginning of the twentieth century when Ludiwg Prandtl was performing flow visualization on wings and bodies in a water tunnel. In this way Prandtl was observing the flow in a qualitative way and only in the eighties of that same century, with the increase of laser and computer power, possibilities emerged for quantitavely describing the flow. Starting in laboratories PIV seeped to other fields in fundamental and industrial research.

The principle of Particle Image Velocimetry is summarized in Figure 8.6. Basically what is shown is a windtunnel with seeding particles, which are illuminated by the laser in a plane and recorded at two distinct times (t and t'). The shift of the particles between the two consecutive shots is used for the determination of the velocity vector. Different interrogation windows for a pair of images are analyzed, such that each of these interrogation window results in a velocity vector. As a basis for the determination of these vectors different statistical methods are used such as auto and cross correlation methods.

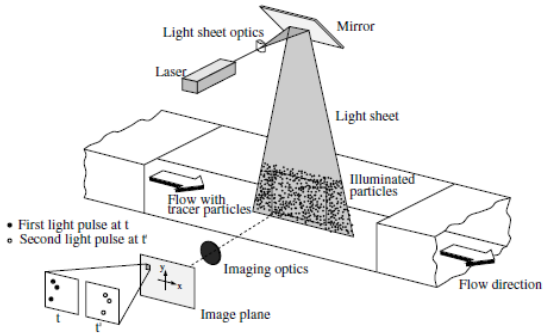

Figure 8.1: The principle of Particle Image Velocimetry explained; a seeded flow is illuminated and recorded at time t and t+Δt

Particle Image Velocimetry is non-intrusive meaning that no probes or pressure orifices are emerged in the flow, which might cause disturbances in the flow, especially at high speed flows or in boundary layers close to a wall. The technique allows the measurement of large parts of flow fields in a variety of applications in gaseous and liquid media. This feature of covering a large part of the flow is unique in that sense that other techniques that measure velocity only measure velocities in a single point. It is also possible to measure unsteady phenomena. By selecting larger particles it is easier to perform the recording of the particles (illumination can be less, while obtaining enough scattered light for the photographic film), but a velocity lag might be introduced. It is important to check whether the tracer particles follow the motion of the fluid particles. Smaller particles will follow the flow better. So a compromise between following the flow and illumination has to be found. By capturing the images the duration of the illumination pulse should be short enough to 'freeze' the motion of the particles. The time delay between to consecutive pulses should be long enough to be able to determine the displacement between the tracer particles, without having them leaving the light sheet due to out-of-plane velocity components. Medium density homogeneously distributed is desired for high quality evaluation. The two pulses mean two recordings, which can be stored on one image, or on two different images. An important fact is that the size of the interrogation windows should be chosen such that the influence of the velocity gradients is minor in the evaluation of the velocity vector.

Fluid	Material	Diameter [μm]	Desnity [kg/m^3]
Air	DEHS	1-3	10^3
Air	Glycol water solution	1-3	10^3
Air	Vegetable oil	1-3	10^3
Air	TiO_2	0.2-0.5	1-4 x 10^3
Water	Latex	5-50	10^3
Water	Sphericell	10-100	0.95-1.05 x 10^3
Water	Silver coated hollow glass spheres	30-100	¿10^3

Table 8.1: Suitable particles for performing PIV

8.2 Flow seeding and seeding techniques

Microscopic particles introduced in the flow with an appropriate amount of around 10^9 and 10^{12} particles/m^3 generally do not affect the flow. Beyond this limit the flow might behave as a multiphase flow. This process is governed by the relation of $m_{fluid}/m_{particles}$. Tracer particles are randomly distributed and convected along the local flow trajectory. Having the proper fluid-particle ratio it is of major importance so that the particles scatter light efficiently in order to be captured by the camera. The particle diameter d_p and the index of refraction relative to the fluid (n/n_f) are the major parameters in determining the scattering of the tracers. There is a balance between the scattering of the particle and the abillity of the particle to follow the flow. Therefore a trade-off needs to be found for optimal performance. Suitable particles for the fluid air and water are summarized in Table 8.1.

A performance parameter of a particle following the flow is the characteristic response time τ on a step input on the flow (gasflow is considered):

$$\tau_p = d_p^2 \frac{\rho_p}{18\mu} \tag{8.1}$$

In general it can be stated that the response time should be lower than the smallest time scale of the flow, which sets high requirements for turbulent flow. This relation can be captured by the particles Stokes number S_k:

$$S_k = \frac{\tau_p}{\tau_f} \tag{8.2}$$

where τ_f is the flow characteristic time, that can be modelled by $\tau_f \approx \frac{L_f}{\Delta V}$.

Other requirements for the choice of seeding material have to do with health and safety aspects. The material should not be hazardous and toxic if inhaled. Also it should not be reactive or corrosive in contact with parts of the flow facility. Seeding material that naturally evaporates leaving minimum residues contaminate the facility and optical devices in a less extent.

The scattering efficiency of tracer particles are dependent on the ratio of the refractive index, the wavelength (λ^{-4}) and on the particle diameter d_p. The scattering of light for particles as large as the wavelength occurs in the Mie-regime. The phenomenon is characterized by a maximum forward scatter at 180 degrees and another relative maximum at 0 degrees. Side scatter efficiency is very low in this regime.

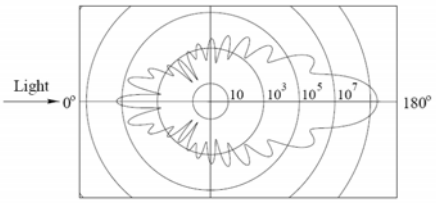

Figure 8.2: A scatter profile of a particle with maximum scatter at 180 degrees

8.3 Illumination of the flow

Finite observation times are required for the detection of the particle motion. For the determination of magnitude and direction of a tracer particle the particles should be illuminated twice within the time of separation. The duration of the illumination is governed by the equation 8.3. Streaks and dots are avoided by applying this relation.

$$\delta t \ll \frac{d_\tau}{VM} \tag{8.3}$$

Another requirement is that only particles lying within the thin sheet as determined by the laser optics are illuminated. The position of the lasersheet controls the in-depth direction. Thirdly, it is important that the digital imaging devices can capture the scattered light. Planar illumination requires that the thickness of the light sheet is of the order of 1% of the height and width.

For the illumination, a laser is used because of the easiness to define a lasersheet and the fact that the source is monochromatic. A solid state Nd:YAG laser is often used for experiments, emitting a wavelength of 532 nm. This laser exists of two laserheads firing independently at the required pulse seperation. Repetition rates are in the range of 10-50 Hz.

For the formation of the lasersheet different arrangements of lenses can be applied. Figures 8.3 and 8.4 show different arrangements. The left case shows a cylindrical lens expanding the beam, where the second spherical lense compensates the effect of the first lens. The result is beam expander along the vertical direction. In this way uniform illumination along the propagation direction is achieved. However, illumination areas can only be relatively small. The requirement for achieving a lasersheet with constant width is found in Equation 8.4 For larger areas the setup in Figure 8.4 is required achieving a diverging lasersheet, which is governed by Equation 8.5. In case of a dual head laser it is important that the two laser sheets (coming from the seperate laserheads) overlap for about 80 %, to reach a proper quality for the laser sheet.

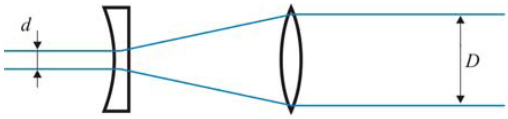

Figure 8.3: Optics for achieving a constant width sheet

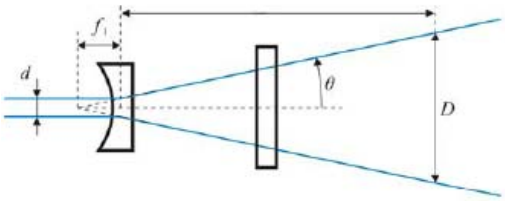

Figure 8.4: Optics for achieving a diverging sheet

$$D = \frac{f_2}{f_1} d \tag{8.4}$$

$$D = 2L \tan\theta + d \tag{8.5}$$

where $\theta = \arctan \frac{d/2}{f_1}$

8.4 Imaging optics

By using Particle Image Velocimetry one has to deal with the simple rules of optics. In Figure 10.21 the optics parameters are summarized.

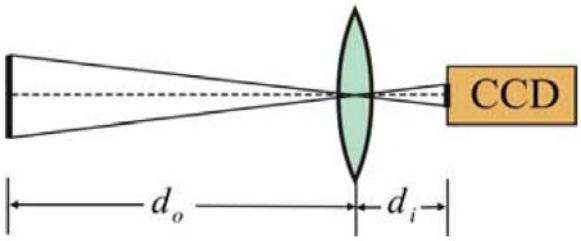

Figure 8.5: The distance from lense to chip d_i is the image distance and the distance from lense to object d_o is the object distance

$$\frac{1}{d_i} + \frac{1}{d_0} = \frac{1}{f} \tag{8.6}$$

Through basic optics an estimation of the focal length of the lens can be determined (equation 10.8). The magnification factor corresponding to this setup is defined in equation 10.9.

$$M = \frac{z_0}{Z_0} \tag{8.7}$$

On basis of equation 10.10 the diffracted minimum image diameter can be calculated. In this equation $f_\#$ is the focal number, which is the focal length divided by the aperture

diameter. The minimum image diameter is only found when using very small particles, otherwise (for larger particles or magnifications) the geometric imaging is more important. If lens abberations are neglected then the particle image diameter δ_τ is determined by equation 10.11.

$$d_{diff} = 2.44 f_{\#}(M+1)\lambda \tag{8.8}$$

$$\delta_\tau = \sqrt{(M d_p)^2 + d_{diff}^2} \tag{8.9}$$

With this diffracted image diameter it is possible to calculate the field of depth. With Equation 10.12 it is possible to deduce which parameters influence the field of depth. By analysis one can say that the higher the focal number, the larger the focal depth. So reducing the aperture increases the field of depth, or the other way around, increasing the focal length decreases the field of view. Reducing the aperture means that less light can be captured by the object glass, which might cause problems (particles are less visible) with the illumination intensity of the laser system.

$$\delta_z = 2 f_{\#} d_{diff}(M+1)/M^2 \tag{8.10}$$

8.5 Imaging seeding density

The seeding density in a PIV image is defined by the number of particles per unit pixel area. Also the source density can be expressed. In Equation 8.11 the source density is expressed, where the first fraction denotes the number of particles per unit area the second fraction is the area of the single particle image. The image density is expressed in Equation 8.12, where D_I^2 is the area of an integration window. In both equations, C is the tracer concentration in particles per m^3, Δz_0 is the light sheet thickness in meters, M_0 is the image magnificiation, D_I the interrogation spot diameter [m] and d_τ the particle image diameter [m].

$$N_S = \frac{C \Delta z_0}{M_0^2} \times \frac{\pi}{4} d_r^2 \tag{8.11}$$

$$N_I = \frac{C \Delta z_0}{M_0^2} \times D_I^2 \tag{8.12}$$

When the typical distance between particle images becomes smaller than the distance travelled between exposure, individual tracking of the particles is not possible anymore and tracking of an image ensemble is necessary, which is PIV.

8.6 Digital Image Recording

A CCD (charge couple device) converts photons into free electrons. While discharging of the CCD, current and voltage are propertional to accumulated charge. An array of these elements pixels form a grid on which an image can be recorded. The voltage cannot be read locally per pixel, but is read out per line. The readout is typically done at a rate of 10 MHz. However, the sensor architecture allows recording rates of only 10 Hz. For PIV this is too slow and hence an interline transfer CCD architecture is necessary for capturing the two subsequent exposures in the order of micro seconds. The interline transfer CCD contains a charge buffer close to the original pixel, in which the charge can temporarily be stored. The pixel is then ready for new exposure after this transfer time. Then at the end of two exposures the sensor must be read through.

Imaging small particles on a CCD requires some considerations from sampling theory. The size of a typical CCD pixel is of the order of 10 μm. Sometimes the pixel size is larger than the individual particle image, thereby losing the information of the flow. It is then said that the particle image field is optically undersampled and discretization effects will limit the accuracy of the particle motion estimation. In case the particles are between 1 and 3 pixels large, reconstruction from the different light intensity on the pixels is possible. However if the pixels are too large the spatial resolution decreases. The optimum is $d_\tau = 2 - 2.5$.

8.7 Evaluation of particle image motion

In order to determine the velocity vectors over an entire PIV image some postprocessing is required. The following list shows the 4 steps required for a proper determination of the velocity vectors.

- Image windowing
- Cross-correlation analysis
- Correlated sub-pixel interpolation
- Divide by time and scaling

Figure 8.6 shows the *image windowing* in which, the entire image is partitioned into cells (interrogation windows) containing a considerable amount of tracer particles. In each of these cells a velocity vector is determined.

Consequently, a *cross-correlation analysis* is performed, which is a statistical tracker operator that is applied to the corresponding interrogation windows of the two exposures. This process returns the discrete cross-correlation map in which the peak positions relative to the origin describe the average particle image displacement. Equation 8.13 describes the discrete correlation function, where I and I' have been described in Figure 8.6.

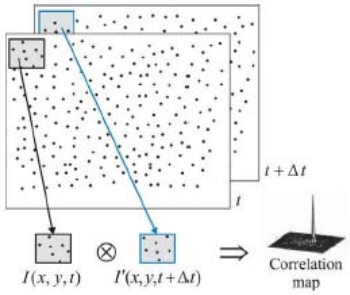

Figure 8.6: Discrete cross correlation

$$\varphi(m,n) = \frac{\sum_{i,j=1}^{I,J} I(i,j) \cdot I'(i-l, j-m)}{\sqrt{stdev(I) \cdot stdev(I')}} \tag{8.13}$$

The correlation peak of the discrete correlation map can be interpolated to reach sub-pixel accuracy. Figure 8.7 shows the interpolated location of the maximum peak

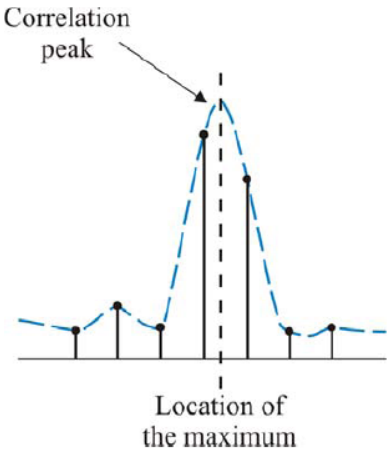

Figure 8.7: Discrete cross correlation with a peak at sub pixel level

There are several interpolation schemes available which are the center of mass method, the parabolic fit and the Gaussian fit, in which the latter one shows the best performance in general. The position of the interpolated maximum is then the displacement measured. The velocity is then obtained by dividing by the known time seperation between the laser pulses, multiplying by the size of the pixel and dividing by the imaging magnification.

8.8 Optimization rules

The time seperation between two laser pulses should such that the majority of particles are imaged in the same window at both exposures, such that the number of particle pairs is large. The maximum in-plane displacement should be smaller than 1/4 of the

window size. The maximum out-of plane displacement should be less than 1/4 of the light sheet thickness. And the maximum in-plane variation of particle displacement should not exceed the particle image diameter.

Chapter 9

Momentum flux equation

The momentum flux equation is the tool which will be used to calculate the unsteady forces from the acquired images by Particle Image Velocimetry (PIV). The foundation of this method is described in Section 9.1. In Section 9.2 the practical procedure to calculate the force is explained. Section 9.3 is devoted to the analysis of the momentum flux equation on a vortex generated flow. This section is meant to demonstrate the characteristic terms, which contribute to the force. Thereafter, the effect of homogenous noise, applied to the vector field is analyzed in Section 9.4. The flowfield generated in Section 9.3 is used and an addition of random noise is applied to this vector field. An analysis is performed on the behaviour of the separate contributions to the force with the random noise applied. Since the vector fields obtained by Particle Image Velocimetry are affected by random noise, it is important to know the mechanisms due to noise for the separate contributions to the force. Section 9.5 describes two statistical methods that can be applied to reduce the error due to the random noise created in Section 9.4. A different type of error is the systematical error. In Section 9.6 two forms of inhomogeneous errors applied to the vortex generated velocity field. The errors are based on the fact that a flow domain consists of multiple Fields of View (FOV), which are partitions of such a flow domain. The errors addressed are the misalignment error and the error on basis of measurements taken at different flow conditions. Section 9.7 is based on a Reynolds Averaged Navier Stokes model, in which a two dimensional flow is generated for two different flow situations. The effect of contour radius, spatial grid resolution and the number of contour points is evaluated. In Section 9.7.4 an analysis with multiple contours is performed on basis of the procedure described in 9.5. The chapter finalizes with a discussion on alternative methods for the determination of the lift (by circulation) in Section 9.8.

9.1 Definition of the momentum flux equation

The application of the momentum flux equation lies in Particle Image Velocimetry. Through this method the possibility exists to determine the forces in a non-intrusive way with only

the knowledge of the velocity field and its spatial and temporal derivatives. The different terms in the flux equation correspond to different flow characteristics such as vorticity. By combining the visualization of the flow through PIV and the analysis of the different contributions to the force by using the momentum flux equation, a powerful method exists in understanding aerodynamic phenomena.

The work of F. Noca et al [1999] describes that when a bluff body is submerged into a fluid in relative motion, the body experiences a force. The force acting on the body can be determined from the external force which is needed to hold the body onto a given trajectory and is referred to be an extrinsic force determination technique. By using e.g. strain gauges the extrinsic force can be determined.

Alternatively, the forces on the body can be derived from the fluid mechanics equations on basis of flowfield quantities, which is referred to be an intrinsic force determination method. Todays experimental work allows the determination of the flow quantities by for example Digital Particle Image Velocimetry.

An intrinsic method can be used when extrinsic methods are not practical. In addition, intrinsic methods yield a quantitave functional relationship between the fluid-dynamic forces and the vorticity in the near wake.

The fundamental equation for the intrinsic method is the momentum equation in integral form (Equation 9.1), where $\vec{u}$ is the flow velocity, $\vec{u_s}$ is the body wall velocity, p is the pressure, I is a unit tensor and T is the viscous stress tensor.

$$\vec{F} = -\frac{d}{dt}\int_{V(t)} \vec{u} dV + \oint_{Sb(t)} \hat{n}\cdot\left[-pI - (\vec{u}-\vec{u}_s)\,\vec{u} + T\right] dS - \oint_{S(t)} \hat{n}\cdot(\vec{u}-\vec{u}_s)\,\vec{u} dS \tag{9.1}$$

In order to evaluate Equation 9.1 the pressure field p is required. This can be overcome by rewriting this equation into the momentum flux equation. Equation 9.2 shows the momentum equation in flux form, referred to as the momentum flux equation:

$$\frac{F}{\rho} = \oint_{S(t)} \vec{n}\cdot\gamma_{flux} dS - \oint_{Sb(t)} \vec{n}\cdot[(u-u_s)u] dS - \frac{d}{dt}\oint_{Sb(t)} \vec{n}\cdot(ux) dS \tag{9.2}$$

$$\begin{aligned}\gamma_{flux} &= \tfrac{1}{2}u^2 I - uu - \tfrac{1}{N-1}u(x\times\Omega) + \tfrac{1}{N-1}\Omega(x\times u)\\ &-\tfrac{1}{N-1}\left[\left(x\cdot\tfrac{\partial u}{\partial t}\right)I - x\tfrac{\partial u}{\partial t} + (N-1)\tfrac{\partial u}{\partial t}x\right]\\ &+\tfrac{1}{N-1}\left[x\cdot(\nabla\cdot T)\,I - x\,(\nabla\cdot T)\right] + T\end{aligned}$$

where $\vec{n}$ is a unit vector, N is the dimension of the flow field, u is the flow velocity (in vector form), u_s is the body wall velocity (in vector form), I a unit tensor and T is the viscous stress tensor with μ the coefficient of dynamic viscosity. The viscosity term is denoted in Equation 9.3. The derivation of this equation is written in F. Noca et al [1999]

$$T = \mu\left(\nabla u + \nabla u^T\right) \tag{9.3}$$

Figure 9.1 shows a body submerged in a flow bounded by the boundary $S_b(t)$ in a volume V(t) bounded by boundary S(t). The geometrical definitions in this figure form a basis for the determination of the force experienced on the body as denoted in Equation 9.2.

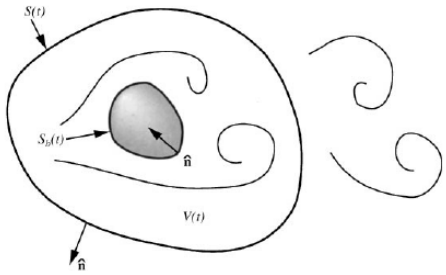

Figure 9.1: Domain of integration for the evaluation of fluid-dynamic forces on a bluff body (F. Noca et al [1999])

By enclosing the body by a predefined contour, the force acting on the body on basis of the first integral of Equation 9.2, can be determined by the momentum flux equation. The only information needed for evaluating the equation is the velocity data in a flow domain that encloses the body. Velocity fields can for example experimentally be obtained by application of Particle Image Velocimetry. The flux equation in time dependent form can produce time-dependent forces over a contour surrounding a body submerged in a flow, which is of interest in unsteady aerodynamics.

The second term of Equation 9.2 represents the slip condition at the boundary S_b as shown in Figure 9.1. This term will vanish, since in this experiment there is no suction or blowing applied. The third part, the time derivative of the surface integal of Equation 9.2, contributes when an acceleration of the body S_b is felt in the flow. This acceleration can be caused by a deformation of the body in time.

9.2 The application of the momentum flux equation

In order to understand the momentum flux equation, the equation is separated in the components specified in Table 9.1.

Part	Term	Mathematical expression
I	Inviscid term	$\frac{1}{2}u^2 I - uu - u(x \times \omega) + \frac{1}{N-1}\omega(x \times u)$
i	Momentum term	$\frac{1}{2}u^2 I - uu$
ii	Vorticity term	$-u(x \times \omega) + \frac{1}{N-1}\omega(x \times u)$
II	Time dependent term	$[x \cdot \frac{\partial u}{\partial t} I - x\frac{\partial u}{\partial t} + \frac{\partial u}{\partial t} x]$
III	Viscous term	$\frac{1}{N-1}\left[x \cdot (\nabla \cdot T)\, I - x\,(\nabla \cdot T)\right] + T$

Table 9.1: The break down of the flux term into an inviscid term, a vorticity term, a time dependent term and a viscous term

The first part is known to be the inviscid term, which consists of a momentum term ($\frac{1}{2}u^2 I - uu$) and a vorticity term ($-u(x \times \omega) + \frac{1}{N-1}\omega(x \times u)$). The time dependent term

(II) acts when an acceleration in the flow is felt ($\frac{du}{dt} \neq 0$). Term III is referred to be the viscous term, which is only non zero for viscous flows.

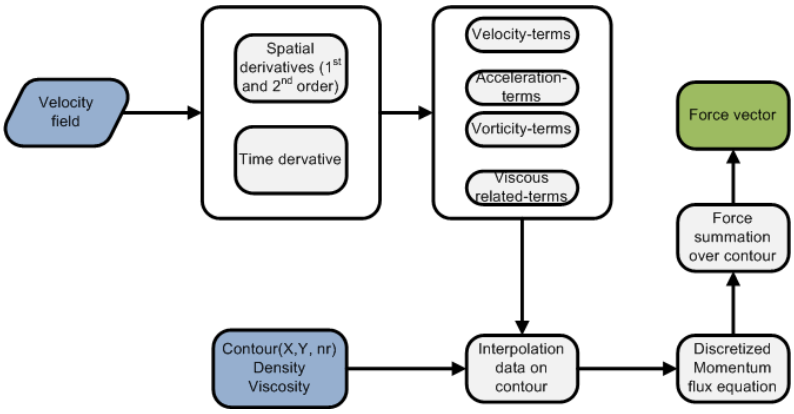

Figure 9.2: Procedure for obtaining the force vector on a body submerged in a flow

The flowchart in Figure 9.2 shows the procedure for deriving the force vector on a body submerged in a flow. The blue blocks indicate the input that is defined by the user. The velocity fields can either be obtained through experiments or numerical calculations (Computational Fluid Dynamics). On basis of this velocity field, contours can be defined by specifying the x- and y-coordinates and the spacing between adjacent points. The spatial and temporal derivatives that are necessary for the determination of the force are obtained by the application of finite difference schemes on the original flow field data, yielding the acceleration, the vorticity and the viscosity (2^{nd} order derivative). An interpolation is applied such that the determined flow field data is projected onto a contour. For vorticity a change of coordinates of the contour is necessary as written by C.J. Simao Ferreira et al [2008]. "The asymptotic variation of the vorticity over the contour as it crosses the wake can result in a significant numerical integration error. This difficulty can be overcome by a change of reference frame, where the origin is set where $\|\frac{d\omega}{dS}\|$ is maximum, thus reducing the influence of the correct estimation of the peak ω (C.J. Simao Ferreira et al [2008])." For every node on the contour the contribution of the momentum flux equation is calculated. The final step is the summation of the individual contributions, yielding the force vector.

9.3 The momentum flux equation in a vortex generated velocity field

For the analysis of the terms addressed in Table 9.1 a velocity field needs to be generated in order to apply the momentum flux equation. A vortex flow singularity as described in Chapter 6 is used as a basis for the generation of the flow field. The mathematical model for generating a two-dimensional point vortex is denoted by Equation 9.4.

$$\begin{bmatrix} u \\ v \end{bmatrix} = \frac{\Gamma}{2\pi\left((x-x_0)^2+(z-z_0)^2\right)} \begin{bmatrix} 0 & 1 \\ -1 & 0 \end{bmatrix} \begin{bmatrix} x-x_0 \\ z-z_0 \end{bmatrix} \tag{9.4}$$

The addition of the vortex generated flow and a uniform flow field yields a velocity field which induces a force perpendicular to the uniform incoming flow. This force produced by this model can be evaluated using Equation 9.5. This in turn is the reference force for all the cases presented in this section.

$$\vec{F} = \begin{bmatrix} u \\ v \\ w \end{bmatrix} \times \begin{bmatrix} \Gamma_x \\ \Gamma_y \\ \Gamma_z \end{bmatrix} \tag{9.5}$$

In order to evaluate the flux equation a contour must be selected on which the integral can be evaluated. Four ellipse contours are defined in the vortex generated flow domain as depicted in Figure 9.3. The flow field considered is on basis of the parameters shown in Table 9.2.

Parameter	**Value**	
Undisturbed windspeed	21	[m/s]
Density	1.205	$[\frac{kg}{m^2}]$
Gamma	2	$[\frac{m^2}{s}]$
Lift	50.61	[N]
Drag	0	[N]

Table 9.2: The conditions for a vortex generated flow

With the vortex model presented, two separate cases can be defined:

- fixed vortex addressing the inviscid term of the momentum flux equation
- moving vortex addressing the time dependent term of the momentum flux equation

For the fixed vortex it is assumed that the vortex has a fixed position in reference with an incoming undisturbed flow. The force produced is due to the evaluation of part I (the inviscid term, according to Table 9.1) only. Table 9.3 shows that the definition of the contour does not influence the force produced in the case when a vortex has a fixed position. The contours selected are depicted in Figure 9.3.

For the moving vortex one defines V_∞=0. And by giving the vortex the velocity V=$V_{\infty,fixed}$ = $21m/s$, yields the same result in terms of total force as found in the fixed vortex case, but the contributing part of the equation is entirely shifted to the time dependent term. In Figure 9.4 the time derivative of the x-velocity is shown. The illustration shows a movement of the vortex to the left. In this example it is important that the contour encloses the moving vortex in the specified time interval in which the movement takes place.

This demonstration shows that the contribution to the lift force shifts from the inviscid term to the time dependent term, by changing from the perspective of a fixed vortex submerged in a flow to a perspective where the body actually moves in the flow.

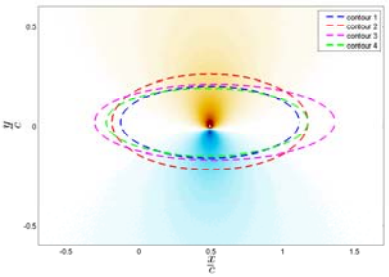

Figure 9.3: Total velocity field of a fixed vortex in a uniform flow ($U_\infty = 21m/s$, $\Gamma = 2m^2/s$). The inviscid term is responsible for the force.

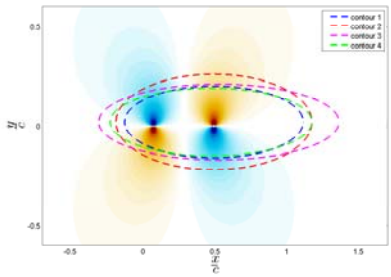

Figure 9.4: The acceleration field of a moving vortex ($U_{vortex} = -21m/s$), $\Gamma = 2m^2/s$. The time dependent term is responsible for the force.

Contour	Flux [N]	Inviscid [N]	Time term [N]	Viscous [N]
1	50.609	50.609	0	0
2	50.610	50.610	0	0
3	50.609	50.609	0	0
4	50.609	50.609	0	0
Ref.	50.61	50.61	0	0

Table 9.3: The effect of contour position on lift for a fixed vortex submerged in a uniform flow ($V_\infty = 21m/s$, $\Gamma = 2m^2/s$

Contour	Flux [N]	Inviscid [N]	Time term [N]	Viscous [N]
1	50.609	0	50.609	0
2	50.610	0	50.610	0
3	50.610	0	50.610	0
4	50.611	0	50.611	0
Ref.	50.61	0	50.61	0

Table 9.4: The effect of contour position on lift for a moving vortex submerged in a uniform flow

9.4 The force error on a velocity field with random noise

Some artificial noise on basis of a Gaussian distribution is added to velocity field in Figure 9.3. The generation of the noise is done in two fold on basis of a Gaussian distribution, where one percent of the undisturbed velocity is taken as the standard deviation for the x-components of the separate velocity vectors; and 0.25% of the undisturbed velocity for the y-component. These percentages are selected on basis of the analysis performed in *Experimental Aerodynamics* [2007], in which the PIV error is estimated on basis of the resolution. Equation 9.6 shows the formula for the modelling of a Gaussian noise distribution.

$$P(x) = \frac{1}{(\sigma\sqrt{2\pi})} e^{(-(x-\mu)^2/(2\sigma^2))} \tag{9.6}$$

The mean of the introduced error μ is set to 0 for both the x and y velocity, the standard deviation $\sigma_x = 0.01 \cdot U_\infty$ and the standard deviation $\sigma_y = 0.0025 \cdot U_\infty$. For the moving vortex two velocity fields are generated, which both are subjected to the defined random noise. Thereafter the time derivative is taken.

The effect of noise can be found on the lift force for the fixed and moving vortex as denoted respectively in Table 9.5 and Table 9.6. In the case when no noise is considered the entire contribution is due to respectively the inviscid term and time term only. Now

by introducing homogeneous noise over the vector field, artificial viscosity is found. The error found in the inviscid term can be more than 50 % with the noise level as prescribed. For the time dependent term the errors are considerably less.

Contour	Flux [N]	Inviscid [N]	Time term [N]	Viscous [N]
1	50.339	50.332	0	0.007
2	57.589	57.599	0	-0.010
3	28.357	28.353	0	0.004
4	63.753	63.735	0	0.018
Ref.	50.61	50.61	0	0

Table 9.5: The effect of noise on the inviscid lift term for a fixed vortex submerged in a uniform flow

Contour	Flux [N]	Inviscid [N]	Time term [N]	Viscous [N]
1	49.404	-0.840	50.238	0.006
2	51.246	0.437	50.810	-0.001
3	51.538	0.821	50.719	-0.002
4	53.508	3.820	49.694	-0.006
Ref.	50.61	0	50.61	0

Table 9.6: The effect of noise on the lift time term for a moving vortex submerged in a uniform flow

Although drag cannot exist in the generated velocity field, Tables 9.7 and 9.8 show that noise introduces an artificial drag component. Again the fixed vortex case shows a larger drag component than the moving vortex case.

Contour	Flux [N]	Inviscid [N]	Time term [N]	Viscous [N]
1	3.100	3.102	0	-0.002
2	-0.719	-0.723	0	0.004
3	-1.236	-1.237	0	0.001
4	1.377	1.374	0	0.003
Ref.	0	0	0	0

Table 9.7: The effect of noise on the inviscid drag term for a fixed vortex submerged in a uniform flow

Contour	Flux [N]	Inviscid [N]	Time term [N]	Viscous [N]
1	0.715	0.574	0.143	-0.002
2	0.242	0.378	-0.143	0.007
3	-0.642	-0.159	-0.484	0.001
4	-0.689	-0.076	-0.612	-0.001
Ref.	0	0	0	0

Table 9.8: The effect of noise on the drag time term for a moving vortex submerged in a uniform flow

The fact that the moving vortex case shows a smaller error than the fixed vortex case, can be explained by the mathematical nature of the inviscid term. By definition it uses a multiplication of the velocity vectors (or velocity vector times velocity derivative vector), which amplifies the error. This effect is not found in the definition of the time dependent term and hence the effect of noise is less.

9.5 Random error reduction methods

In every PIV measurement random noise exists. By taking multiple samples it is possible to average out the random noise and hence a proper force evaluation can be done. The random error observed is in two fold as described in Chapter 7, which are the statistical error and the fluctuations due to turbulence, leaving a mean part and a fluctuating part as repeated again in Equation 9.7.

$$P = P_{mean} \pm P_{flux} \tag{9.7}$$

By taking a phase locked average [1], the random error can be reduced. The following example shows the reduction of the error by taking multiple samples.

The analysis is performed for contour 1 in the fixed vortex case as depicted in Figure 9.3. According to Table 9.9, the accuracy and precision as defined in Section 7.2, increase by increasing the number of observations.

number of observations	$M_{Lift}+\sigma_{lift}$ [N]	$M_{Drag}+\sigma_{drag}$ [N]
1	50.8 ± 7.9	0.0 ± 1.2
10	50.6 ± 3.5	0.3 ± 0.6
20	50.43 ± 1.8	0.03 ± 0.5

Table 9.9: The mean and standard deviation of the lift force for the averaged fields

Table 9.10 and 9.11 show the build up of the lift force in terms of the inviscid part, the time dependent part and the viscous part for the four previously defined contours in the fixed vortex case. The contribution is due to the inviscid part only, although some minor influence of the noise is felt in the viscous term.

Contour	Flux [N]	Inviscid [N]	Time term [N]	Viscous [N]
1	50.774	50.774	0	0.000
2	43.525	43.521	0	0.004
3	52.053	52.053	0	0.000
4	47.795	47.787	0	0.008
Ref.	50.61	50.61	0	0

Table 9.10: The lift calculated on an averaged flow field of 10 samples

Contour	Flux [N]	Inviscid [N]	Time term [N]	Viscous [N]
1	52.248	52.247	0	0.006
2	53.297	53.297	0	0.000
3	51.469	51.469	0	0.000
4	49.881	49.881	0	0.000
Ref.	50.61	50.61	0	0

Table 9.11: The lift calculated on an averaged flow field of 20 samples

In general, it can be stated that the accuracy is increased with increasing number of observation governed by Equation 7.5.

Fifteen contours are taken for the case with a fixed vortex and the case with a moving vortex, showing the mean and the fluctuation of the force as determined on the different contours. The effect of taking multiple contours shows that the random error can be reduced in this way as shown in Table 9.12, where sigma indicates the deviation measured in the force.

Case	μ_{lift} [N]	σ_{lift} [N]	μ_{drag} [N]	σ_{drag} [N]
Inviscid term (fixed vortex)	50.8	7.9	0.0	1.2
Time term (moving vortex)	51.7	2.0	-0.1	0.5

Table 9.12: The mean force and fluctuation of fifteen contours

As already demonstrated the time term suffers less from the introduction of the noise in the velocity field than the inviscid term. The values measured within the set of contours

[1] An average over a set of similar observations in time

range from $P_{mean} \pm 3\ \sigma$, showing a large range of values for the inviscid term. However, for both terms the random error is reduced by taking multiple contours enclosing the body (vortex). The accuracy increases again according to Equation 7.5.

9.6 The force error on a velocity field with systematical errors

A flow field does not show only random errors and hence the statistical reduction technique presented in Section 9.4 does not work in all cases. In case of a PIV experiment, scratches and smudges on windows can obscure the camera view, causing systematical errors in the measurements which need to be analyzed and, if possible, extracted from the data sets. The combination of taking multiple velocity fields and multiple contours would improve the result on the force evaluation, reducing the random error of the measurement only. However, the systematical errors are still part of the solution. It is important to identify and quantify these errors, in order to state that the obtained results are reliable or not. The inhomogeneous errors related to PIV measurements which will be analyzed, are:

- the misalignment error due to shifts in the fields of view
- measuring at different wind tunnel conditions for each different field of view

The PIV setup is such that the flowdomain associated with these errors must have been obtained by partitioning the flow domain in multiple Fields of View, where per FOV an acquisition is performed at a different time instant.

Misalignment errors For the misalignment error every recording per FOV is performed by changing the camera position that can lead to unwanted misalignment errors between the separate fields of view due to errors in the positioning system of the cameras. The concept of misalignment is depicted in Figures 9.5 and 9.6.

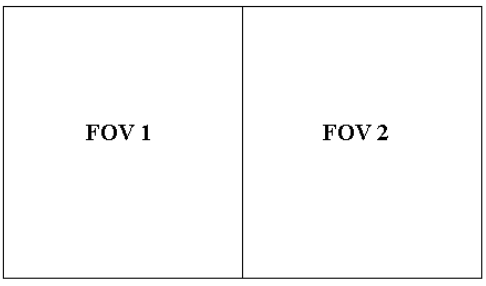

Figure 9.5: The assumed positions of the two Fields of View

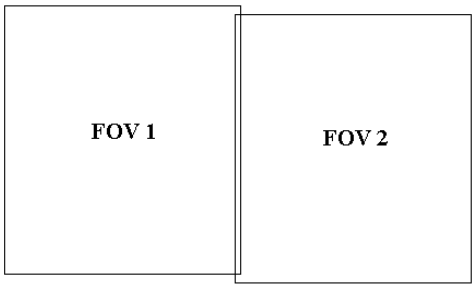

Figure 9.6: The actual positions of the two Fields of View

In order to mimic a misalignment due to experimental tolerances, the fields are randomly shifted 5 mm from eachother. On the edges artificial vorticity is observed (Figure 9.8). In this specific case the error can be quantified for the fixed vortex case and the moving

Case	μ_{lift} [N]	σ_{lift} [N]	μ_{drag} [N]	σ_{drag} [N]
Inviscid term misalignment (fixed vortex)	50.36	0.21	-0.11	0.09
Time term misalignment (moving vortex)	50.39	0.43	-1.10	0.36

Table 9.13: The effect of misalignment on the evaluation of 15 contours

vortex case. The analysis is performed over a set of 15 contours, where the mean and fluctuating part of the force are denoted in Table 9.13.

From the results it can be concluded that the time term shows more influence to this type of error than the inviscid term.

Measuring at different conditions The second type of systematical errors is taking measurements at different conditions per field of view. The cause for the deviation in the wind tunnel conditions, lies in the fact that the measurements are performed at different time instances. Figure 9.7 shows the situation of the different conditions. The figure shows a difference in the uniform flow speed.

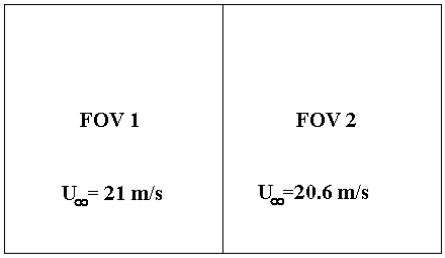

Figure 9.7: Two adjacent Fields of View obtained at different uniform flows

In this vortex flow, the undisturbed velocity is changed for several fields of view. In the vorticity plot at regions where a change is felt, again artificial vorticity is detected. The undisturbed velocity for the different fields of view varies from 20.5 m/s up to 21 m/s. At the interfaces of the fields of view, artificial vorticity is detected. The same effect is detected with the misalignment of the fields of view.

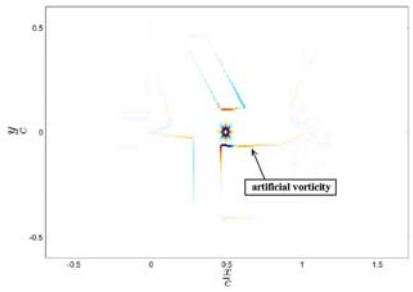

Figure 9.8: The indication of misalignment errors and errors due to measurements at different uniform flow speeds is the detection of artificial vorticity at the interfaces of adjacent Fields of View.

Since the evaluation of the force in case of testing at different conditions is dependent on multiple variables nothing can be said about the error observed.

9.7 The force evaluation on a DU96W180 airfoil in viscous flow

In this section the program Fluent is used for the generation of a velocity fields around a NACA0015 and a DU96W180 at $\alpha = 0$. In case of inviscid flow as prescribed in the previous section in which a vortex element was used for the generation of the flow field, the time dependent term and the inviscid term are analyzed. The cases, which are considered with Fluent, also include viscosity. A Reynolds-Averaged Navier-stokes model with a κ-ϵ turbulence model is chosen. The undisturbed velocity is set to $30m/s$ corresponding to $Re = 2 \cdot 10^6$ at a chord of 1 meter.

For the generation of the results two walls are introduced on the top side and lower side of the domain as read in, in Fluent (Figure 9.9). Further more a velocity inlet and a pressure outlet are used for the generation of the result, leaving a computational domain with a high resolution at the surface of the airfoil to a more course grid at the outside of the computational domain. The data produced by Fluent is exported and the velocity field is then interpolated in matlab.

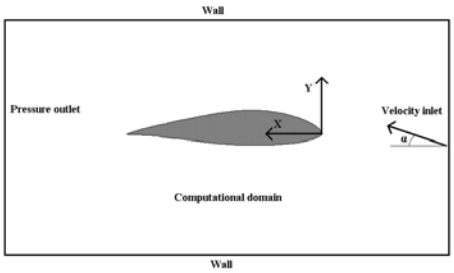

Figure 9.9: Definition of boundaries in Fluent

Figure 9.10 shows a thin wake at $\alpha = 0$. Due to the symmetry of the airfoil the forces are very small. The last case is the DU96W180 windturbine profile designed for high L/D-ratios, showing a more pronounced wake at $\alpha = 0$ (Figure 9.11).

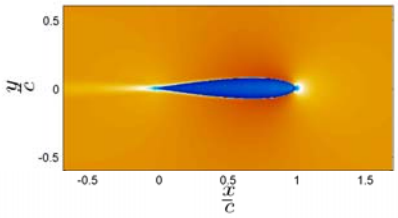

Figure 9.10: NACA0015 profile at $\alpha = 0$

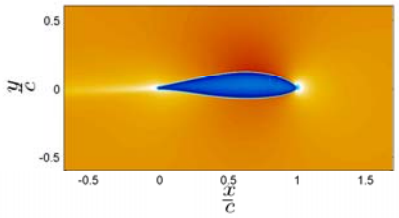

Figure 9.11: DU96W180 profile at $\alpha = 0$

Table 9.14 shows the forces obtained by Fluent, which will be used as reference forces for determining the quality of the momentum flux equation procedure. A convergence

study on the grid size versus the force is not performed, since the interest lies on the reproduction of the force by applying the momentum flux equation. In this case the determination of the actual physics is less important.

Case	Airfoil	Angle of attack	Lift	Drag
1	NACA0015	0 degrees	1.13 N	6.88 N
2	DU96W180	0 degrees	154.82 N	19.02 N

Table 9.14: Two airfoil testcases with a relatively low and relatively high loading

In this section the following items will be addressed:

- Influence of contour radius on the momentum flux force
- Influence of spatial grid resolution on the momentum flux force
- Interpolation errors
- Influence of specific test case on the momentum flux force

9.7.1 Influence of contour radius on evaluated forces

Firstly, the effect of increasing contour on the force prediction is demonstrated for the DU96W180 airfoil at $\alpha = 0$. In Figure 9.12 the vorticity field of this specific case is shown with a set of fifteen body enclosing integration contours.

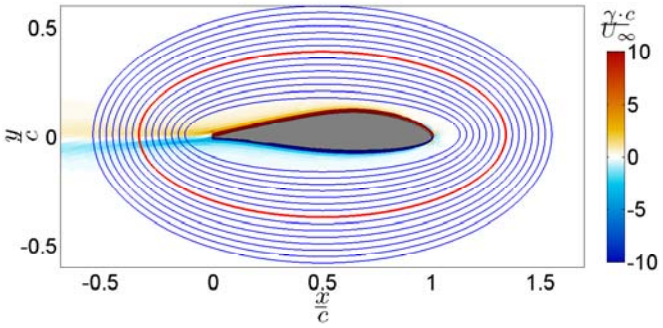

Figure 9.12: Vorticity field with increasing contour showing two distinct regions: the inner region and the outer region

The red contour divides the region in two parts, where the inner region shows large errors and the outer region relatively low errors as illustrated in Figure 9.13. The inner region shows relatively large errors up to ΔC_L=0.03 and the outer region ΔC_L=0.01. The vorticity field shows that the error is reduced when vorticity is less pronounced. This is an indication that the vorticity is a large contributor to the error in the inner region.

In Figure 9.14, the force is decomposed in the momentum term and the vorticity term. The viscous term almost shows no contribution to the force. In the inner region, the momentum term is increasing, where the vorticity stays constant. In the outer region,

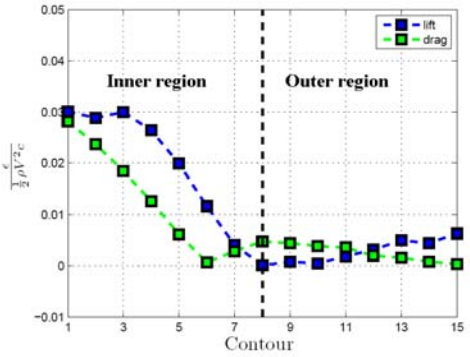

Figure 9.13: The dimensionless error for both lift and drag for a resolution of 2 mm

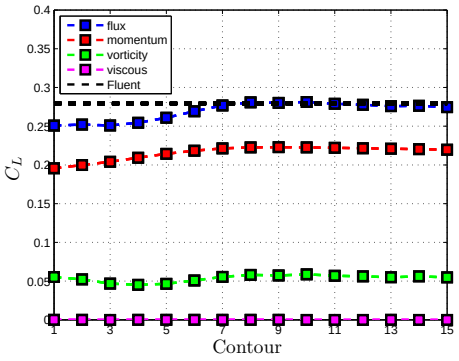

Figure 9.14: The decomposition of the lift term

the momentum term reaches a maximum, where the vorticity term remains the same according to Figure 9.12. The error which is found in the inner region is caused by the finite resolution, the interpolation and the finite difference scheme which is used to calculate the gradients. In the next Section 9.7.2, the sensitivity of the momentum term and vorticity term to gridsize is investigated, showing which term is likely the cause for the observed error in the inner region.

9.7.2 Influence of spatial grid resolution

The influence of spatial grid resolution is tested on two contours, where one contour is selected in the inner region and one contour is selected in the outer region. The contours which are being tested are shown in the vorticity plot in Figure 9.15, where a clear seperation is given by the red ellipse seperating the inner from the outer region.

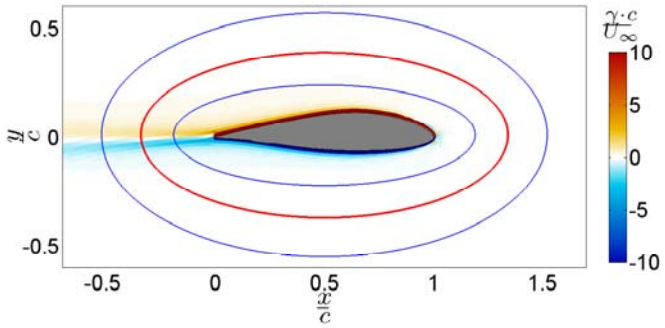

Figure 9.15: The tested contours for the vorticity region and the momentum region

Figure 9.16 shows the influence of increasing grid size on the decomposed lift terms in the inner and outer region. From this figure, one can state that grid sizes larger than 8 % of the chord in the inner region result in errors growing with grid size. This is due to the fact that for this flow phemomena the gradients and therefore the vorticity are not properly determined anymore. This plot shows that the vorticity term is most sensitive to

the gridsize. For drag the same trend is observed as for the analysis with the decomposed lift coefficient. However, drag is heavily influenced for grid sizes beyond 5 %c in the inner region, shown in Figure 9.17. For the outer region the influence of gridsize is felt after 8%c.

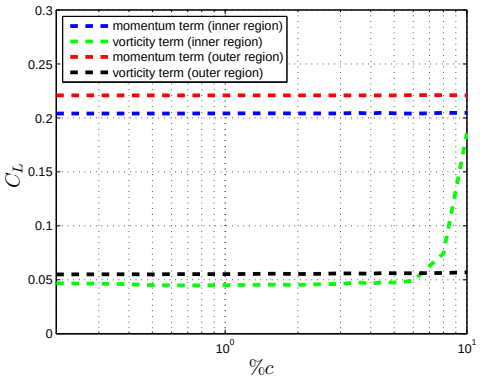

Figure 9.16: The vorticity lift term in the inner region is most susceptible to grid size reduction

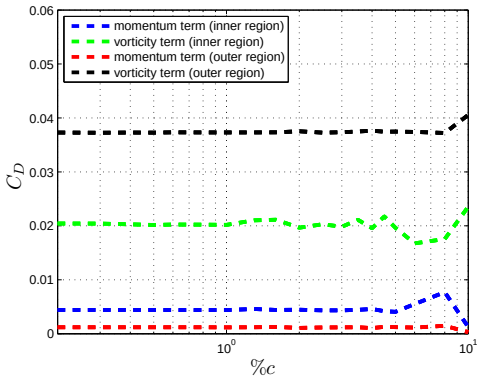

Figure 9.17: The vorticity drag term in the inner region is most susceptible to grid size reduction, already noticable at grid resolutions beyond 1%

The analysis in this section firstly shows that the inner region is more sensitive for the gridsize, secondly the vorticity term is most sensitive to a reduction in resolution independent of the region. The combination of these two facts is that the inner region is very sensitive to the determination of the vorticity term. The next section shows the influence of the interpolation scheme used for the determination of the velocity components and its derivatives to the contour.

9.7.3 Interpolation error

This section puts its focus on the number of contour points that define the integration contour in combination with three different interpolation schemes used, which are:

- nearest neighbour interpolation
- linear interpolation
- cubic interpolation

For lift and drag the result of number of points defined on the contour is evaluated for the three methods as listed, illustrated in Figures 9.18 and 9.19.

The interpolation scheme does not show a large difference on the evaluated force when the number of contour points is large. A decomposition of the force is plotted for the lift force in Figure 9.19. The figure reveals that the vorticity term suffers the most from a reduction in contour points.

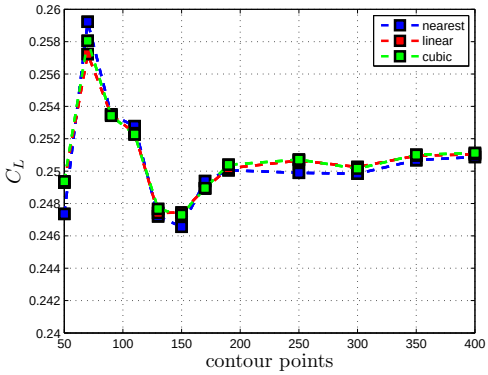

Figure 9.18: The performance of three different interpolation schemes as a function number of contour points for the inner region

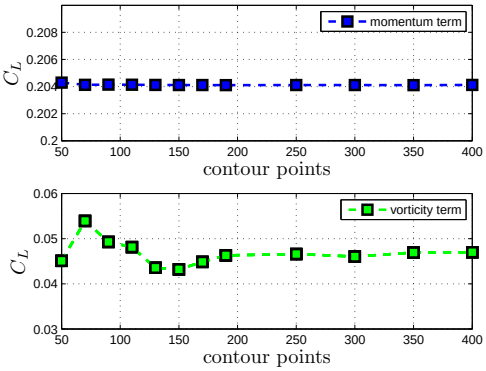

Figure 9.19: The figures show respectively the momentum term and the vorticity term as a function of nr of contour points

9.7.4 Analysis with multiple contours

This section uses the statistical error reduction method as posed in Section 9.5. The method applies fifteen contour integrations for both the inner region and the outer region for the two cases described in Table 9.14. The NACA0015 airfoil is loaded by relatively low lift and drag forces, whereas the asymmetrical DU96W180 is more heavily loaded. The methodology applied for the inner and outer region, results in a mean lift and drag value (μ) with an indication of the fluctuating value (σ). The standard deviation (σ) is a measure how accurate the force is predicted and the mean value (μ) shows the offset from the value as determined by Fluent. This offset is expressed as the accuracy of the force predictor tool, which is defined in Equation 9.8, where R_{fluent} is the reference value as obtained through the CFD software.

$$A_c = 1 - \frac{|\mu - R_{fluent}|}{R_{fluent}} \tag{9.8}$$

For the two airfoil cases in the two specified regions, μ, σ and *accuracy* A_c are denoted in Table 9.15.

Case		μ_{lift}	A_c	σ_{lift}	μ_{drag}	A_c	σ_{drag}	L_{Fluent}	D_{Fluent}
NACA0015@ 0 degrees aoa	Close contours	1.21	93%	0.48	6.74	98%	0.28	1.13	6.88
	Far contours	1.20	94%	1.06	7.11	97%	0.31		
DU96W180 @ 0 degrees aoa	Close contours	142.24	92%	2.67	6.99	27%	2.41	154.82	19.02
	Far contours	152.98	99%	1.73	19.81	96%	0.55		

Table 9.15: The table specifies the performance of the evaluation of fifteen contours for the inner region and outer region. The mean lift and drag (indicated by μ)are determined in correspondence with the accuracy. The fluctuations in the measured force are indicated by the σ symbol

From this table it can be concluded that the accuracy of the lift is most accurately calculated in the far region in the case with the largest force, which is the DU96W180 airfoil. However, the inner region shows the worst performance of all measured lift forces. Next to that the drag in this same inner region shows a very low accuracy. This has to do with

the vorticity term as adressed in the previous sections. This case shows a larger wake compared to the symmetrical NACA0015 airfoil. Therefore, more vorticity is found in the flow domain yielding less accurate results.

The method presented in this section makes use of statistical error reduction by applying multiple contours to calculate total lift and drag. However, increasing the number of integration contours, might not reduce the error on the force, since systematical errors are not targeted in this approach. This method will be used in the analysis of acquired PIV data, despite the lack of the reduction of the systematical error.

9.8 Alternative methods for force determination

Two alternative methods exist for the calculation of lift and drag. Lift can be calculated on basis of the circulation in correspondence with Equation 6.10, where Stokes' theorem relates vorticity to circulation. Drag can be calculated by the deficit of momentum in the wake. Both methods will be compared with the momentum flux equation.

9.8.1 Lift force and circulation

By means of the circulation the lift can be calculated. The circulation is determined by Equation 9.9

$$\Gamma = \oint_C \vec{q} \cdot dl \tag{9.9}$$

Consequently, the lift can be calculated by Equation 9.10

$$L = \rho U_\infty \Gamma \tag{9.10}$$

In Figure 9.20 the force on basis of Equations 9.9 and 9.10 are plotted for the contours as shown in Figure 9.12. As seen in the figure the method shows a tendency of the force towards the reference Fluent value for increasing radii because the method requires to enclose both the airfoil and wake to determine the circulation responsible for the lift force. The integral path must be in the region where the flow can be estimated by potential flow, otherwise the method cease applicability J. Katz et al [2001]. However, for the domain and the contours considered the lift cannot be accurately determined by the method of circulation, where the momentum flux equation predicts the force well for outer contours.

9.9 Conclusions

The chapter describes the performance of the momentum flux equation in an inviscid flow and a viscous flow (Reynolds-Averaged Navier-Stokes). The inviscid flow model is

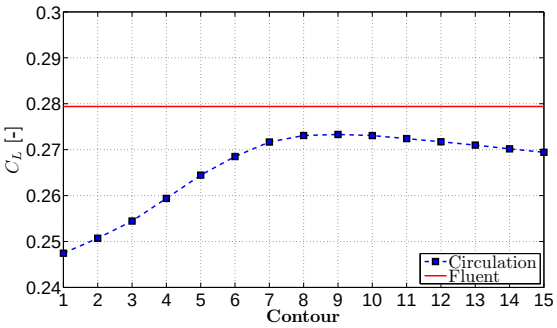

Figure 9.20: The tested contours for the vorticity region and the momentum region

created by the generation of a vortex and a subsequent addition of a uniform flow field. The first analysis on this flow field shows that independent of contour position, the force is accurately calculated. By generating the same vortex, letting U_∞ be zero and giving the vortex the velocity of the uniform flow field as in the fixed case, the same total force is obtained. This analysis shows that the contributing part for the total force shifts from the inviscid term in the fixed vortex case to the time dependent term in the moving vortex case.

In the second analysis of this inviscid flow field, noise is added to the velocity vectors. The evaluation of the force shows that the inviscid term is more sensitive to the addition of noise than the time dependent term. Two statistical error reduction methods are provided based on the increase of number of observations and the application of multiple force evaluations over different integration contours.

In the third analysis inhomogeneous errors in the flow domain are considered. Inhomogeneous errors can be caused by misalignment due to multiple fields of view and measurements taken for each field of view at different wind tunnel conditions. It is hard to quantify the actual error in PIV images, because of the systematical nature of the error. However, the indication of such an error is possible by the detection of artificial vortcicity.

In the fourth analysis the RANS flow field over two different airfoils is used as a basis for the evaluation of the force. In this analysis the influence of contour position is demonstrated. This analysis reveals two distinct regions denoted as the inner region and the outer region. In the inner region, which is close to the airfoil surface, the vortcity is much more pronounced than the outer region. The conclusion of this analysis shows that the inner region cannot predict the reference force as good as the outer region. The analysis with varying gridsize shows a large sensitivity of the vorticity term compared to the momentum term. Also in the analysis with a varying number of contourpoints, the vorticity term is most sensitive. These results state that vorticity is likely to give the major errors in the the force results. Finally, a demonstration is given on the use of multiple contours in the case of a NACA0015 and a DU96W180 airfoil in both the inner region and the outer region. Again in the case where vorticity is much more pronounced, errors occur in the evaluation of the force.

The lift is calculated with an alternative method on the DU96W180 airfoil, that is not limited by the time resolution. The lift force converges to the reference value, but can only be well captured if the contour encloses the airfoil and wake such that the integral path must be in the region where the flow can be estimated by potential flow. So if the flow domain is limited to regions close to the airfoil, this method cannot predict the lift force accurately.

Part II

Experiment

Chapter 10

Wind tunnel experiment description

The wind tunnel experiment is described in this chapter. Firstly the cases to be considered in the experiment are given. In correspondence with these test cases, the setup of the experiment is illustrated on basis of the hardware used and the acquisition scheme provided. The components and handlings which have an influence on the PIV measurement are identified and if possible quantified. For the PIV part all the characteristics in this experiment will be demonstrated in order to capture the flow in ultimate conditions. In Section 10.1 the experiments that are considered in the wind tunnel test will be described on basis of aerodynamic considerations. Section 10.2 gives an overview of all the apparatus concerning the windtunnel, the wing and the actuation of the flap. In Section 10.3 an outline on the setup of PIV in this particular resreach is given, Thereafter, the procedure for the acquisition of the PIV images is described in Section 10.4. Finally, experimental errors and difficulties are discussed in Section 10.5.

10.1 Experimental test cases

The test cases considered in this section are performed on a DU96W180 airfoil model with actuated 0.2c trailing edge flap. The airfoil model has a chord c=0.5m and a span b=1.8m. All the cases considered in the experiment are performed with a freestream velocity U_∞=21 m/s. This research addresses steady and unsteady aerodynamic conditions. The level of unsteadiness is expressed as the reduced frequency, which is defined in Equation 10.1, describing the ratio of periods for oscillation and wake convection (see Section 5.7).

$$k = \frac{\pi f c}{U_\infty} \tag{10.1}$$

Table 10.1 contains the test cases which are considered in the experiment. All experiments are performed at an angle of attack $\alpha = 0\,\text{deg}$ and Reynolds number Re=$7 \cdot 10^5$.

Testcase	Angle of attack α [deg]	Flap angle β [deg]	Reduced frequency [$k = \frac{\pi f c}{U_\infty}$]	Reynolds number [-]
1	0	0,2,4,6	0	$7 \cdot 10^5$
2	0	3± 3	0.1	$7 \cdot 10^5$
3	0	1± 1	0.2	$7 \cdot 10^5$
4	0	3± 3	0.2	$7 \cdot 10^5$

Table 10.1: Four test cases of which Case 1 is performed in steady conditions and the other cases are conducted in unsteady conditions

For the steady cases the flap has a fixed position. For the unsteady cases the motion of the flap is assumed to be sinusoidal of the form denoted in Equation 10.2, where A denotes the equilibrium flap position in degrees, B is the flap amplitude in degrees, f is the frequency in Hertz and t is time in seconds.

$$\beta = A + B \sin 2\pi f t \tag{10.2}$$

Case 1 in Table 10.1 shows steady conditions ($k = 0$) for flap angles β=0, 2, 4 and 6deg flap down. Case 2 is conducted at a reduced frequency $k = 0.1$, where the associated frequency f=1.34 Hz. The sinusoidal motion is performed with equilibrium position $A = 3°$ and an amplitude B=3°. Case 3 and case 4 are performed at k=0.2, which corresponds to f=2.67 Hz, where case 3 is defined by A=1° and B=1°, and case 4 by A=3° and B=3°.

The amplitude of the motion (B) is not incorporated in the expression of the reduced frequency, but is a parameter that shows to have an influence on the unsteadiness of the flow. Insight is gained in the influence of amplitude B and reduced frequency k on the field of unsteady aerodynamics, by addressing the test cases of Table 10.1.

10.2 Experimental apparatus and conditions

This section is devoted to the description of the experimental apparatus and conditions required for performing the experiment. The wind tunnel conditions and the main characteristics of wing and flap are described. Furthermore the procedure for actuation of the flap is discussed and finally all the equipment and procedures for Particle Image Velocimetry (PIV) are explained.

10.2.1 Windtunnel conditions

The low-speed Low-Turbulence Tunnel (LTT) is an atmospheric closed-throat single-return type tunnel, with a contraction ratio of 17.8. A six bladed fan is driven by a 525 kW DC motor, producing a maximum test section velocity of around 120 m/s. In case of two dimensional testing the section allows Reynoldsnumber up to 3.5 million. A relative low turbulence level can be achieved, i.e. 0.015% at 20 m/s to 0.07% at 75 m/s. The test section is 1.80 m wide, 1.25 m high and 2.60 meters long. Figure 10.1 shows the closed section and indicates where the contractions are. The testsection is indicated with the letter A. The windtunnel experiment is performed in the atmospheric conditions stated in Table 10.2.

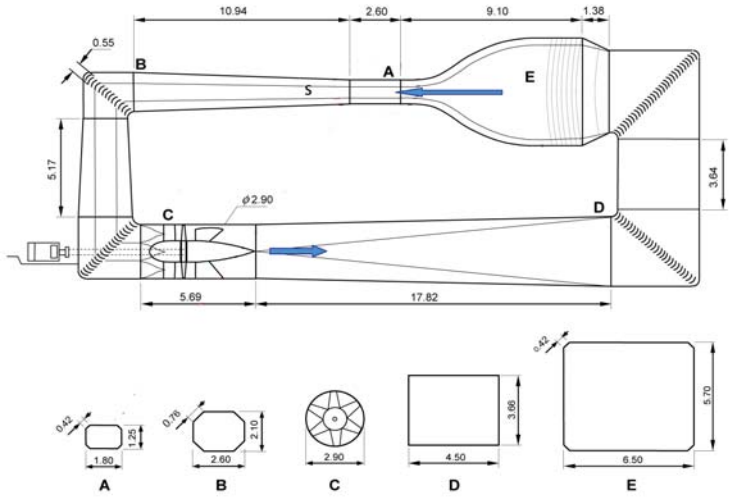

Figure 10.1: The layout of the low speed Low Turbulence Tunnel (LTT) where the test section is indicated by A

Temperature T	[deg C]	$\mu_T = 19.05$	σ_T =0.62
Pressure P	$[hPa]$	$\mu_P = 1011.63$	σ_P =8.94
Density ρ	$[\frac{kg}{m^3}]$	μ_ρ =1.205	σ_ρ =0.004
Freestream velocity	U_∞ $[\frac{m}{s}]$	V_{min}=20.6	V_{max} =21.1
Reynolds number Re	[-]	Re_{min}=$6.8 \cdot 10^5$	Re_{max}=$7.1 \cdot 10^5$

Table 10.2: The mean and standard deviations (Gaussian distribution) of the windtunnel conditions encountered in the experiment and their influence on the Reynolds number

The result of the atmospheric fluctuations have an effect on the Reynolds number in the windtunnel, which fluctuates between $6.8 \cdot 10^5$ and $7.1 \cdot 10^5$ as based on Equation 10.3, where ρ is the density, c is the chord and μ is the dynamic viscosity.

$$Re = \frac{\rho c U}{\mu} \tag{10.3}$$

The dynamic viscosity is a function of temperature T as written in Equation 10.4, where S is an effective temperature; for air S=111, $T_0 = 273$ K and $\mu_0 = 1.716 \cdot 10^{-5}$.

$$\frac{\mu}{\mu_0} = \left(\frac{T}{T_0}\right)^{\frac{3}{2}} \frac{T_0 + S}{T + S} \tag{10.4}$$

10.2.2 The airfoil model

The DU96W180 airfoil will be used in this research, which is designed for wind turbine applications. The airfoil is tested through the years at different Reynolds numbers of which at least one experiment is performed at Re=$7 \cdot 10^5$. Lift and drag polars from these steady measurements in clean configuration are shown in Figure 10.3. The stall region is beyond $\alpha = 15°$, where the drag increases exponentially with angle of attack. In this thesis only cases at angle of attack $\alpha = 0$ are conducted, which correspond to $C_{L_{\alpha=0}}$=0.3 and $C_{D_{\alpha=0}}$=0.02 of the steady experiment performed by Rooij [2008].

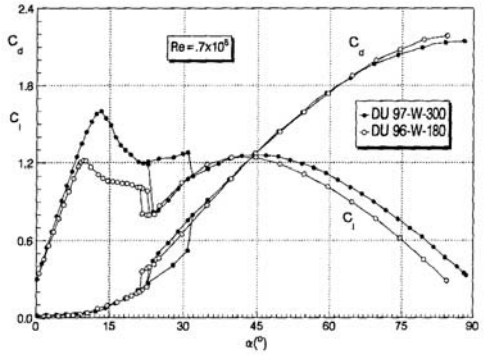

Table 10.3: Lift and drag polar of the DU96W180 at $Re = 7 \cdot 10^5$

Airfoil	DU96W180
Span b	1.80 m
Chord c	0.5 m
Maximum thickness	18 %
Material	Carbon composite
High lift device	0.2c TE flap

Table 10.4: The physical characteristics of the DU96W180 airfoil model

The dimensions and characteristics of the airfoil model are found in Table 10.4. The span of the airfoil model b=1.8 meters, such that it fits horizontally in the LTT windtunnel. The chord of the model c=0.5 meter and the maximum thickness percentage is 18 %c, which implies a thickness of 9 centimeter.

The airfoil model has a 0.2c trailing edge flap on the pressure side. The hinge point is indicated in Figure 10.2. Figure 10.4 demonstrates the extreme positions for the maximal flap angle range ($\beta = 3 \pm 3°$) as denoted in Table 10.1 (case 2 and case 4).

Figure 10.3 illustrates the offset between the original designed DU96W180 airfoil and the airfoil model at midspan position. The curvature of the wing at the pressure side up to

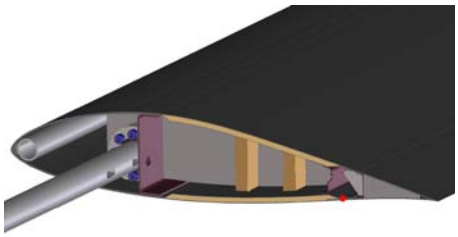

Figure 10.2: A side view of the DU96W180 airfoil model where the flap hinge position is indicated with the red dot

0.2c differs from the original shape. A decreasing offset from leading edge to trailing edge is detected meaning a slight difference in curvature over the entire suction side. The flap shows an added thickness on the lowerside. The interface between the main wing and the flap is discontinuous on the lower and upper side because of a plastic strip closing the gap, preventing flow leakage between the pressure and suction side of the airfoil. Hereby a solid boundary is created, which is desired in this experiment.

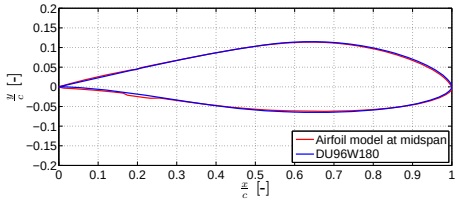

Figure 10.3: Airfoil model shape at midspan compared to the original DU96W180 airfoil

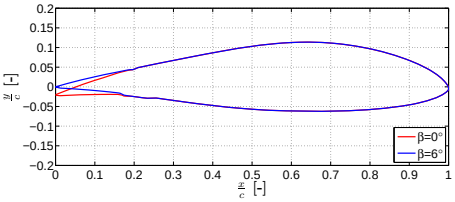

Figure 10.4: The flap angle range addressed in this research, $0° \leq \beta \leq 6°$

10.2.3 Fixation of the wing in the windtunnel

The model is fixed horizontally in the windtunnel with the suction side of the airfoil surface face up as depicted in Figures 10.5 and 10.6.

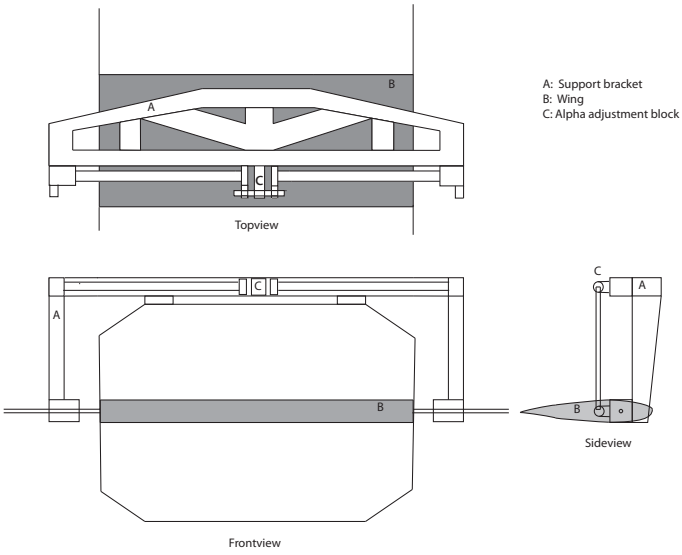

Figure 10.5: The model fixation bracket (A) is attached to the topside of the wind tunnel. The wing (B) is attached to the bracket by two axes. The α-adjustment block (C) fixes the orientation of the wing (α) with the horizontal (sideview)

The supporting structure as shown in Figure 10.7 keeps the wing in place, where the α-adjustment block of Figure 10.5 is depicted.

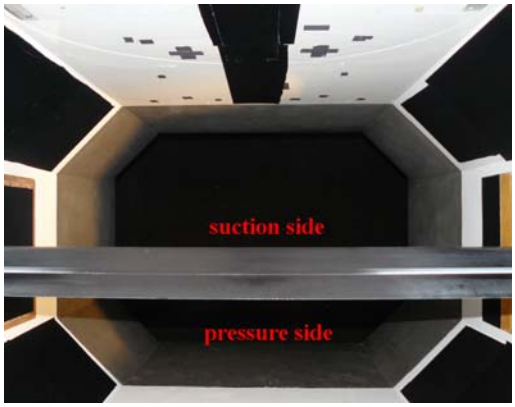

Figure 10.6: The wing is attached in the wind tunnel with the suction side face up

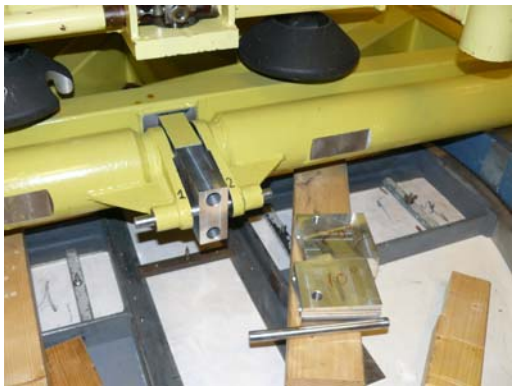

Figure 10.7: Model support structure with aluminum α-adjustment block

In this fixed position the wing is levelled with a waterlevel on top of a negative mould of the wing, where the horizontal is used for the allignment of the wing. The setup of this calibration is depicted in Figure 10.8. Once the model is levelled, the angle of attack can easily be adjusted by a range of α -adjustments blocks. Figure 10.5 shows the upper part

of the bracket where the α -adjustments blocks can be attached. At α=0° the 0-block is fixed in the bracket.

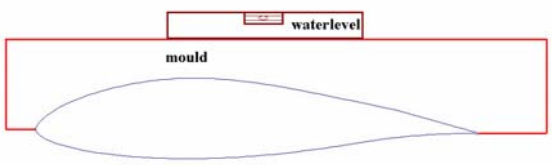

Figure 10.8: The calibration of the angle of attack is performed with the aid of a negative mould and a waterlevel.

The low speed low turbulence tunnel is equiped with an accurate balance system, which can measure forces and moments in three directions. Only with static measurements the support bracket A from Figure 10.5 can be hooked up to a balance system, determining the forces and moments applied to the model. However, the balance system does not allow for unsteady measurements and hence the support bracket cannot be attached to the balance system lacking a way of validating the forces as determined by the momentum flux equation.

10.2.4 Transition strips

Transition strips are used for the experiment in order to have a controlled position for the change of laminar flow to turbulent flow. The transition strips induce a more pronounced two dimensional flow compared to a clean configuration. This controlled transition position can also be applied in Computational Fluid Dynamics (CFD) models, such that the transition point of the experiment matches the transition point of the numerical CFD approach. The transition strips are glued to the wing at 0.02 c and 0.1 c for respectively the suction side and pressure side of the airfoil. The thickness of the strips is chosen on basis of Equation 10.5, where k is the roughness height, x is the position from LE to roughness particle, R_x is the Reynolds number on basis of the length from LE to roughness particle and the free stream velocity $\frac{Ux}{\nu}$ and η_k is the nondimensional height in the boundary layer based on roughness height.

$$k = \frac{2 \cdot x\eta_k}{\sqrt{R_x}} \tag{10.5}$$

Using charts for the determination of η_k, for both the pressure and suction side, 40 μm thickness should induce transition from laminar to turbulent flow.

10.2.5 Aerodynamic characteristics of the DU96W180

The coordinates of the original DU96W180 are used in a two dimensional simulation with XFOIL (Drela [2001]) determining lift, drag and moment coefficients. In this way the characteristics of the profile are estimated in steady conditions. The variation of the lift- and dragcoeffcient with flap angle β at $\alpha = 0$ is illustrated in Figures 10.9 and 10.10. Moment coefficient and transition as function of β are found in Figures 10.11 and 10.12.

For the generation of the results the flap hinge position in the XFOIL model is set to the lower surface of the airfoil, where the actual hinge is found on the airfoil model. The lift as a function of β for $0 \leq \beta \leq 6$ is almost linear, where $0.25 \leq C_L \leq 0.52$. The maximum drag coefficient at β=$6^{\text{deg}} = 0.014$. Furthermore it can be stated that transition will not occur more upstream than the $\frac{x}{c}$ positions of the transition strips. For convenience the lift, drag and moment coefficient are also plotted with varying angle of attack α and are found in Appendix D.

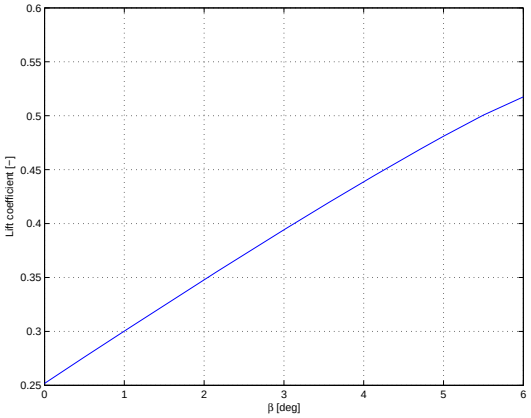

Figure 10.9: Lift coefficient as function of flap angle β

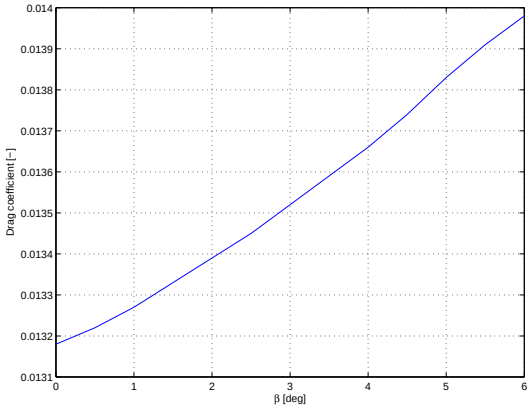

Figure 10.10: Drag coefficient as function of flap angle β

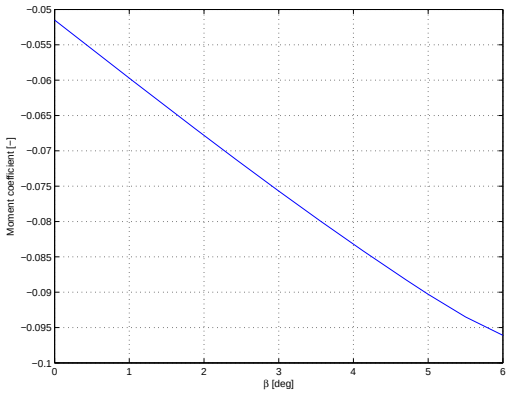

Figure 10.11: Moment coefficient as function of flap angle β

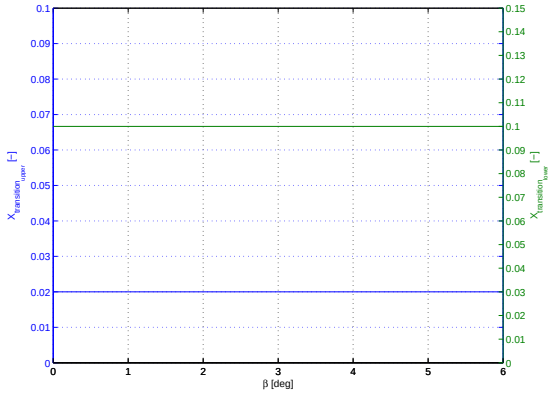

Figure 10.12: Transition as function of flap angle β

10.2.6 Actuation of the flap

In order to create the unsteady conditions as posed in Table 10.1. The flap needs to be actuated in a controlled way. By definition unsteady conditions of $k = 0.1$ and $k = 0.2$ are created by obeying, Equation 10.6. Equation 10.6 is a rewritten form of Equation 10.1.

$$f = \frac{k \cdot U_\infty}{\pi \cdot c} \tag{10.6}$$

where f is the flap frequency, k is the reduced frequency, U_∞ is the freestream velocity and c is the chord length. Filling in the appropriate parameters, the frequencies of the flap are determined to be f=0 Hz, f=1.34 Hz and f=2.67 Hz for respectively k=0, k=0.1 and k=0.2. A linear actuator drives the sinusoidal motion with the determined frequencies. The flap is actuated from the side and is considered stiff enough against torsional loads, such that the entire span follows the same sinusoidal motion. On the opposite side of the actuator an angle meter is attached, to measure the flap angle β. The output of the anglemeter is voltage and hence a calibration is done linking the voltage to the actual angle. The calibration is performed for flap angles $0 \leq \beta \leq 6$.

The actuator used is the Parker PRA25 with a COMPAX3 system providing control over the motion of the actuator. A dSPACE system is used for the software part of driving the actuator. The actuator is controlled through a simple feedback loop. The sinusoidal motion of the flap as a function of flap amplitude B and flap frequency f is laid up by a linear translation of the actuator arm. A coupling device as illustrated in Figure 10.13 transforms the linear motion into a rotational motion.

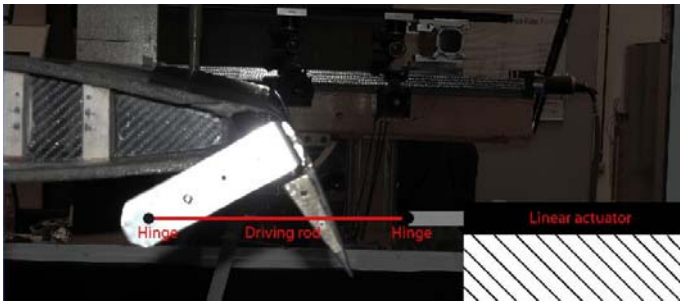

Figure 10.13: The coupling between the linear motor and the flap is applied at the side.

The effect of the coupling is visible in the motion of the flap in Figure 10.14, where the desired motion and the actual motion (averaged over multiple periods) are depicted. A Fast Fourier Transform (FFT) is used to determine the dominant frequencies in the signal of the flap motion measured. The main frequency matches the frequency of 1.34 Hz, corresponding to a reduced frequency k=0.1. The shape of the obtained signal is constant over time and therefore the principle of phase-locked averaging of the flow can be applied.

Phase-locked averaging is necessary for the determination of unsteady/turbulent flow phenomena, in which the average flow behaviour (and fluctuations) can be determined. The principle is based on the averaging of multiple observations (velocity measurements) at the same position in a period. Since the motion of the flap is periodic, a phase-locked averaging can be performed.

10.2.7 Blockage

Solid blockage increases the dynamic pressure over the wing. Assuming the model represents a blunt body, the maximum blockage occurs at the highest flap angle (6 degrees flap down) leading to a blockage of 9.5 %. The flow speed increases relatively with respect to the free stream velocity in the region where the blockage occurs. Thereby the pressure

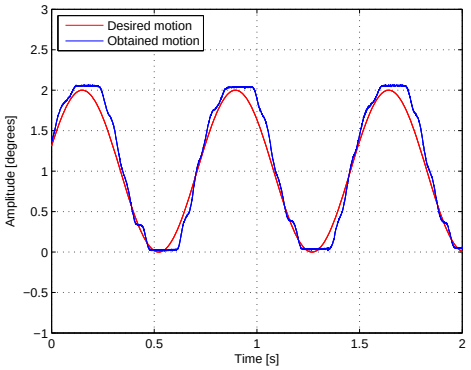

Figure 10.14: The desired sinusoidal motion compared with the obtained quasi sinusoidal motion as determined by the angle meter

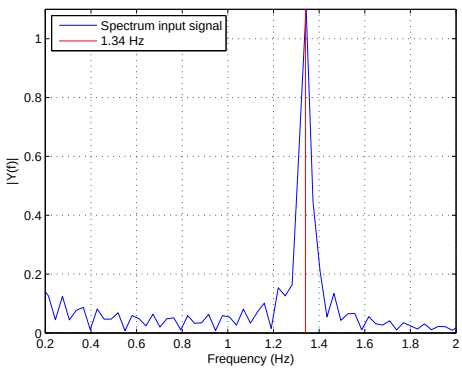

Figure 10.15: Frequency analysis on the obtained quasi sinusoidal signal, where a peak is detected at the desired frequency of 1.34 Hz

decreases with respect to the initial entry pressure. Another type of blockage is the wake blockage, which is associated with the boundary induced flow acceleration formed due to the developing viscous wake. It is also formed because of the presence of the test section walls due to the effect of the viscous displacements effect of the wake.

10.3 Particle Image Velocimetry test setup and apparatus

The PIV experiment will be performed according to the theory explained in Chapter 8. Figure 10.19 shows the PIV experimental setup for the research as part of this thesis.

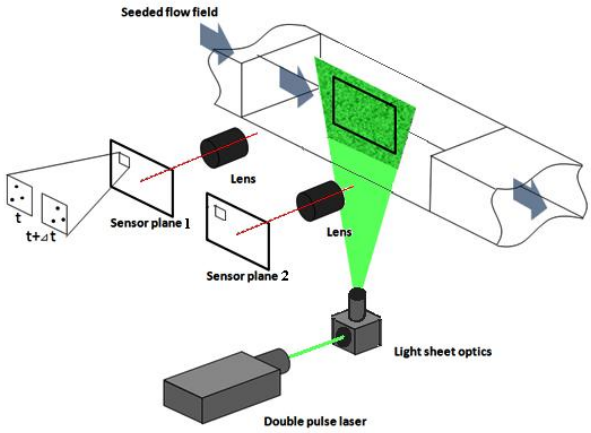

Figure 10.16: The principle of Particle Image Velocimetry; A seeded flow is recorded at time t and Δt. The displacement of the particles between the two recordings are used to determine the velocity vector.

At time t and t+Δt, the flow is recorded by two cameras, producing two partitions of the

flow domain referred to as Fields of View (FOV). The orientation of these two cameras is known as the co-planar orientation for planar (2D) velocity measurements.

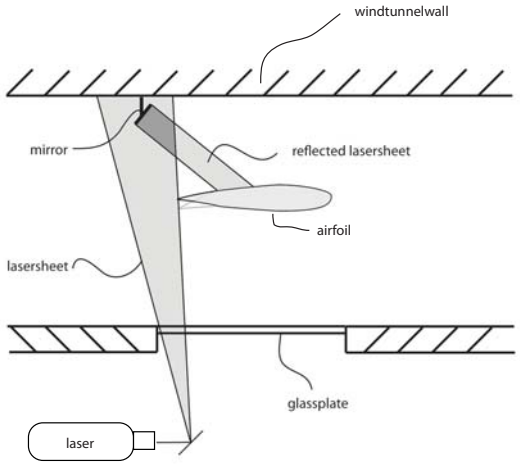

Figure 10.17: The top surface of the model is illuminated by application of a mirror on the upper wind tunnel wall

A traverse system is used for the orientation of the cameras with respect to the flow. With this traverse system it is possible to adjust the image distance and to translate in both x-direction (chordwise) and y-direction (to change from pressure to suction side).

A double pulsed laser is used for the generation of the laser sheet such that at time t and time t+Δ t a recording of the flow can be performed. The laser produces a laser-beam and through laser optics the sheet is generated. The laser is positioned underneath the test section, where a glass plate on the lowerside of the section provides a window for illumination purposes. Through a traverse system the laser can be moved up and donwstream providing a dynamic system for orienting the lasersheet in correspondence with the cameras. The setup of the laser with respect to the model is depicted in Figure 10.17. The illumination of the pressure side is performed without using a mirror for the reflection of the laser sheet. The figure reveals the layout for the illumination of the suction side of the airfoil model, where a mirror is used to illuminate the upper surface.

The position of the smokegenerator is downstream of the airfoil model. This ensures that the seeding particles convect in the flow, such that a homogeneous distribution of particles is obtained upstream. This condition only holds for closed type wind tunnels.

10.3.1 Particle Image Velocimetry basic equipment

Smokegenerator For the seeding of the flow a smoke generator is used. The smokegenerator provides droplets with a diameter of about $1\mu m$. Since the windtunnel is a closed type section, the smoke is constantly pumped through the tunnel. However some leakage occurs and therefore the smokegenerator is constantly seeding the flow with particles to keep the density of particles constant. Due to the setup and low control capabilities of

the smokegenerator inhomogeneous seeding occurs. The cornervanes as shown in Figure (10.1) and natural convection makes sure that at the test section the particles are quasi homogeneously distributed.

Figure 10.18: Smoke generator producing droplets of 1 μm

Figure 10.19: Laser setup underneath the windtunnel

Laser Illumination of the tracer particles is perormed by a Nd:YAG laser, which is a pulsed laser with a repetion rate varying from 10 to 30 Hertz, where the pulse energy varies from 20 to 500 mJ. The wavelength per laser head is 532 nm. Two laser heads deliver two pulsed lasers independently. The two beams are combined by a mirror and polarizing beam combiner. It is important that the two laser beams from the two separate laser heads are aligned with each other, such that at time t and t+Δt (see Figure 10.19) the same region of the flow domain is illuminated for proper capturing of the flow field. The Nd:YAG laser produces seperate pulses of 1064 nm. A doubling crystal doubles the frequency to the green laser light of 532 nm. The laser is equiped with an optical system (see Figure 10.19), which uses two diverging lenses to create a diverging lasersheet.

Camera The two cameras used are of the type LaVision Imager Intense. Imager Intense is a high sensitivity digital 12 bit camera, featuring an interline transfer chip with a 16 MHz progressive scan readout. Exposure times can be as short as 500 ns. Table 10.5 shows some characteristics of the camera.

Double shutter	Two images with 500 ns interframing time
Number of pixels	1376 x 1040 pixels
Pixel size	6.45 x 6.45 μm
Sensor format	2/3”
Spectral range	290 - 1100 nm
Dynamic range	12 bit
Readout rate	16 MHz
Readout noise	5-6 e- @ 16 MHz

Table 10.5: Camera specifications of the LaVision Imager Intense

Scheimpflug If the camera (subject plane) has an angle with the image plane, regions of the image are not in focus if the focal depth is relatively small. In order to reduce the out-of-focus region a Scheimpflug can be used. The concept of the scheimpflug is explained by Figure 10.20. In this figure the lens is oriented such that the subject plane, the lens plane and the image plane coincide in one point, the Scheimpflug point. In this situation the entire image can be captured in focus if the lens (focus) and Scheimpflug are properly adjusted.

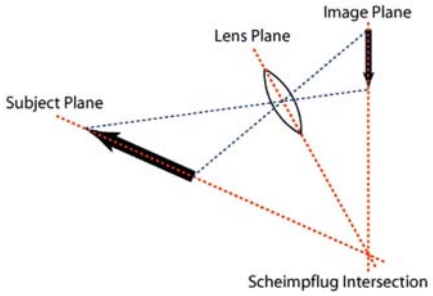

Figure 10.20: The scheimpflug orients the lense, such that the three planes coincide in the Scheimpflug point

10.4 Experimental PIV preparations and procedures

This section discusses the calculation of the resolution in relation with the Field of View. Furthermore the determination of the imaging parameters as described in Section 8.4 is performed. Thereafter a discussion is given on the calibartion of the cameras in co-planar orientation and finally the acquisition procedure is illustrated.

10.4.1 Field of View characteristics

As demonstrated in Chapter 8 several parameters need to be determined for the experimental setup of PIV. It is started with the determination of the FOV with interrogation windows of 32x32 pixels. An interrogation window is a partition of an entire Field of View in which the mathematical correlation is performed, to obtain a single velocity vector. The desired resolution to capture the flow is 1%c, which corresponds to 5 mm per interrogation window. Equation 10.7 demonstrates how the size of the FOV is determined on the constraint of reaching one percent of the chord per 32 pixels.

$$S_{FOV} = \frac{W_{pix}}{S_{int}} \cdot R_{PIV} = \frac{1376}{32} \cdot 0.005 = 0.215m \tag{10.7}$$

where S_{int} is the interrogation window size (1D), W_pix is the amount of pixels on the camera in x-direction and R_{PIV} is the desired resolution, which is one percent of the chord. The height recorded on a photo is related to the size of the CCD chip, which turns out to be 16.88 cm.

Imaging optics

In order to capture the particles in focus one has to deal with the optical setup as shown in Figure 10.21. In this figure Z_0 is the distance from the plane of interest to the lens which is measured to be 1.1 meter. The distance from the lens to the CCD chip is referred to be z_0.

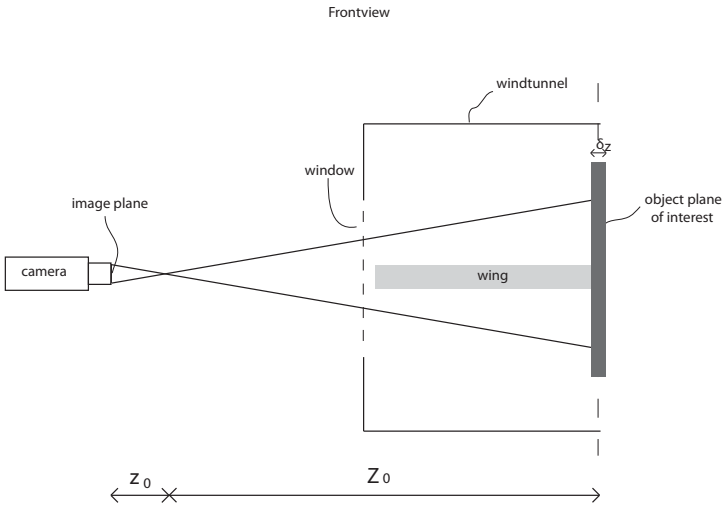

Figure 10.21: Front view of the PIV test setup

With a focal length of 60 mm, the objective distance is $z_0 \simeq 0.06m$ according to eq:focal$_l ength$.

$$\frac{1}{z_0} + \frac{1}{Z_0} = \frac{1}{f} \tag{10.8}$$

A magnification factor of 0.06 is calculated through Equation 10.9.

$$M = \frac{z_0}{Z_0} \tag{10.9}$$

On basis of Equation 10.10 the diffracted minimum image diameter [1] can be calculated, where $f_\#$ is the focal number, which is the focal length divided by the aperture diameter.

$$d_{diff} = 2.44 f_\# (M + 1)\lambda \tag{10.10}$$

The lens used has a range of focal numbers from 2.8 to 32. By changing this number the focal depth can be determined through equations 10.10 up to 10.12. Depending on camera position and orientation, focal numbers of 2.8 and 5.6 are used in this experiment.

The minimum image diameter is only found when using very small particles, otherwise (for larger particles or magnifications) the geometric imaging is more important. If lens

[1] The diffraction limit spot results from the finite resolution of the optical system due to diffraction effects, *Experimental Aerodynamics* [2007]

abberations are neglected then the particle image diameter δ_τ is determined by equation 10.11.

$$\delta_\tau = \sqrt{(Md_p)^2 + d_{diff}^2} \tag{10.11}$$

Equation 10.12 determines the field of depth. By analysis one can say that the higher the focal number, the larger the focal depth. So reducing the aperture increases the field of depth, or increasing the focal length decreases the field of view. Reducing the aperture means that less light can be captured by the object glass, which might cause problems (particles are less visible) with the illumination intensity of the laser system.

$$\delta_z = 2f_\# d_{diff}(M+1)/M^2 \tag{10.12}$$

Specifying the focal number to be either 2.8 or 5.6, such that most of the laser light is captured a focal depth of respectively $6.35 \cdot 10^{-5}m$ and $1.27 \cdot 10^{-4}m$ is found. Meaning that it is easier to focus the particles at a larger focal number, however less light is captured by the CCD chip.

Since PIV deals with two frames that need to be captured for the determination of the velocity vectors it is assumed that one quarter window size of movement of the particles is optimal *Experimental Aerodynamics* [2007]. Thereby the time between two consecutive frames can be calculated through Equation 10.13.

$$\Delta t_{0.25w} = \frac{0.25 S_{int}}{U_\infty} \simeq 7 \cdot 10^{-5} s \tag{10.13}$$

where $S_i nt$ is the interrogation window size in meters and U_∞ is the freestream velocity.

The duration of the illumination of the particles is determined by Equation 10.14. As stated the diameter of the particles is 1 μm, leads to t_{ill} of 1.73 $\cdot 10^{-7}$ s.

$$t_{ill} = \frac{d_{tau}}{V \cdot M} \tag{10.14}$$

10.4.2 Camera Calibration

The cameras are oriented in 2D co-planar orientation as illustrated in Figure (10.22). By making use of a calibration plate it is possible to calculate the orientation of the camera with respect to the plane of interest. This is necessary in order to dewarp the images such that proper velocity data is obtained. An image of the calibration plate is taken and succesively the software program Davis[2] calculates the corresponding dewarping matrix. The calibration of the cameras is performed by placing a calibration plate in the wind tunnel at the spanwise position at which the PIV measurement takes place. Through this calibration it is also possible to see whether the desired size of the FOV is obtained.

[2] A software program suited for the acquisition and postprocessing of PIV images

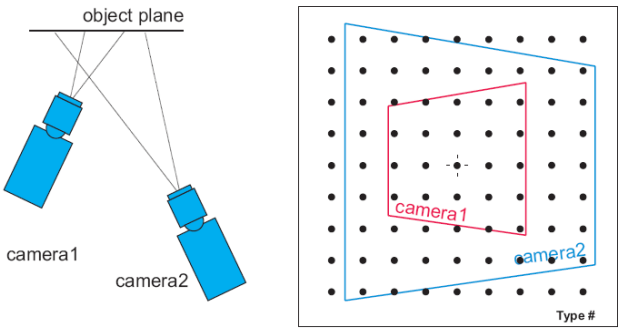

Figure 10.22: 2D co-planar camera orientation in calibration mode, where both cameras are focussed on the calibration plate

10.4.3 Acquisition

For the acquisition the software of La Vision **?** is used, which is specialized in flow visualization. For Particle Image Velocimetry the Davis software package is used, which both performs the acquisition and the postprocessing of the acquired images. For the acquisition a programmable timing unit is required, which triggers the cameras at the desired time t. In this experiment a phase-locked average (see Section 10.2.6) is performed for the determination of the averaged mean flow, meaning that at fixed intervals the motion will be recorded multiple times at the same repeated instance in time. The motion is divided in phases on basis of a phase angle, which is related with time t by Equation 10.15,

$$t = \frac{\phi}{360}\frac{1}{f} \tag{10.15}$$

where basesteps of 45 degrees of phase and ministeps of 5 degrees of phase are used, which all correspond to a certain position in the period of the flap. At these phase angles all the results (flowfields and forces) are considered in this reserach. The ministep is used for acquiring the time dependent terms, by knowing that a phase shift represents an actual timestep represented in Equation 10.15, where ϕ is the phaseshift observed and f represents the frequency of the motion.

In the acquisition procedure, firstly the difference in time is calculated between the trigger signal and the half period as indicated in Figure 10.23.

This difference is then used as a delay such that the reference phase angle at a half period is guaranteed throughout the entire recording. Then from the reference phase angle each recording phase angle is then adressed by the programmable timing unit by calculating a time difference with respect to the reference phase/time. In this way all measurements are taken at the very same instant in time for all the recordings with respect to the reference phase (corresponding to a certain flap position).

In Figure 10.24 the flow chart for the acquisition is shown. There are two inputs which are defined by the user. One of the inputs is the flap motion determined by the equilib-

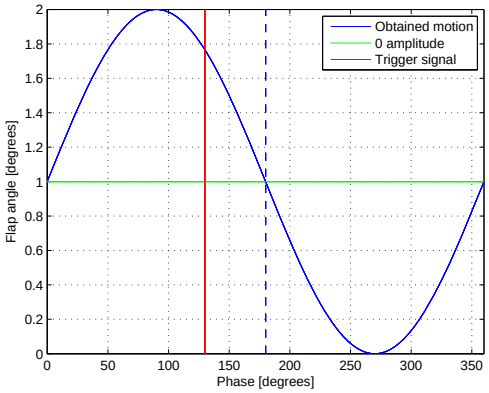

Figure 10.23: The phase is set by calculating the time between trigger signal and half period and adding a delay for the desired phase.

rium position A, the frequency f and the amplitude B, where the flap amplitude B is calibrated with the stroke length of the linear actuator.

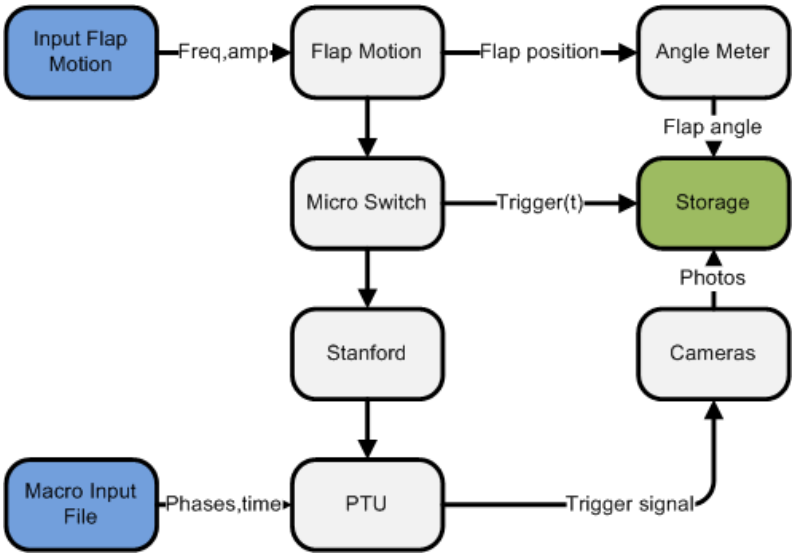

Figure 10.24: Acquisition flow chart

The second input is determined by the macro inputfile. The programmable timing unit (PTU), responsible for the triggering of the cameras and the laser, is fed by two signals. These signals are the actual trigger signal and the signal as produced by the macro file. The actual signal is produced by the linear motor hitting a micro switch, which consequently generates a voltage that is fed into the Stanford device. The Stanford device outputs an appropriate TTL signal which is then fed into the PTU, responsible for the image acquisition signal.

10.5 Experimental errors and difficulties

Timing errors Timing errors are associated with the equipment used to trigger the cameras. The resolution of the timing unit is 10 ns. With the cases considered in this experiment the timing resolution is in the order of milliseconds. Therefore, the PTU will not have a significant error contribution to the defintion of the phases within the sinusoidal motion of the flap.

Flap angle determination The determination of the flap angle is performed with a large uncertainty estimated to be β=$\pm$1deg. The calibration of the flap angle is performed multiple times, in which a waterlevel is used with an accuracy of 0.1 degree. The flap angle determination is based on the principle to align the flap with the horizontal, by the use of a negative mould of the flap (as described in Section 10.2.3). This procedure seemed to be error sensitive.

Laser light illumination difficulties The mirror is inside the wind tunnel section and therefore in direct contact with the particles. Due to skinfriction, particles will accumulate on the mirror reducing the quality of the laser sheet. The area of accumulation is a function of angle of attack of the mirror. A situation is drawn in Figure 10.25. The result of the accumulation leads to a deterioration of the illuminated area in the image.

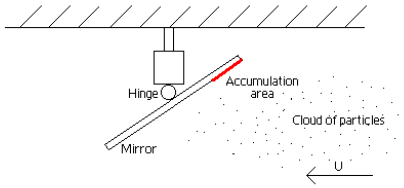

Figure 10.25: Accumulation of particles on the mirror

The suction side of the airfoil model is illuminated by the reflection of the laser light by the mirror mounted to the upper wind tunnel wall (see Figure 10.17). The length that the light has to travel compared to the path for the pressure side is larger. Therefore a difference in intensity of the laser sheet is obtained for the two airfoil surfaces. In Chapter 11, the difference of the quality of the PIV correlation for both sides is illustrated.

Furthermore interference patterns in the laser sheet exist as a function of the orientation of the mirror with respect to the laser light. These patterns are detected in the acquired images and are discussed in Chapter 11.

Chapter 11

Evaluation of 2D PIV experimental results

The chapter describes how the raw untreated images obtained by Particle Image Velocimetry (PIV) are processed. Multiple methods exist for the determination of the velocity vectors. It is important to identify the characteristics of these methods in order to obtain the most accurate result, which is important for the quantification of the unsteady force.

In Section 11.1 preprocessing methods are described that are used to prepare the images for the correlation procedure, responsible for the determination of the velocity vectors. The section is devoted to the analysis of the quality of the different images obtained in the experiment. Subsequently, appropriate methods are presented for improving the quality of the image. Section 11.2 gives an overview of the different correlation methods that exist to determine the velocity vectors. Each method is tested on a partition of the flow field (FOV) containing the wake. In Section 11.2.2 the encountered post processing errors are identified and discussed. Section 11.3 describes the reconstruction of the flow domain on basis of the separate flow field partitions (FOVs). Section 11.4 describes how the velocity data is used for the determination of the temporal and spatial derivatives. Finally, Section 11.5 reveals the velocity field, the vorticty field and the acceleration field of the recorded flow domain.

11.1 Preprocessing of the images

The software used for the determination of the velocity vectors is a program which is developed by LaVision, called Davis LaVision [2005]. Through a GUI all kind of routines can be applied for obtaining the velocity fields. It is important to carefully select the options required for obtaining the correct velocity fields. Before doing the correlation necessary for the actual determination of the vectors, some preprocessing techniques can

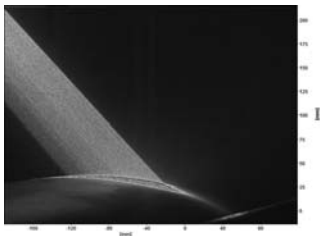

Figure 11.1: The laser sheet reveals an interference pattern

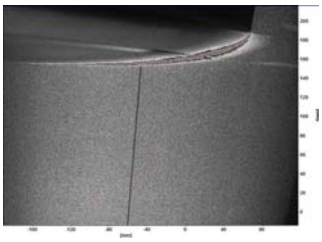

Figure 11.2: The laser sheet shows a large non-illuminated area

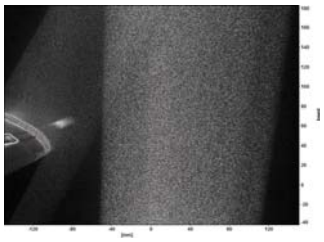

Figure 11.3: Illuminated leading edge with large difference in intensity

be used to increase the quality of the image. This would result in a better quality of the correlation. In Figures 11.1 to 11.3, examples are shown, illustrating several features in the image that have an influence on the actual correlation.

Figure 11.1 reveals a stripe pattern which is due to the reflection of the lasersheet on the mirror. To overcome this problem the mirror should reflect on the front surface of the mirror instead of at the surface behind the glass. Depending on the angle of the mirror with respect to the incoming laser light interference might occur. Snell's law dictates that at the interface of glass and air, part of the laserlight is deflected and consecutively reflected at the back surface of the mirror. Due to the fact that the laserlight has differences in the path length, an interference pattern is detected, depending on the difference of path lengths of two independent waves. There are two types of interference which are constructive and destructive interference. For PIV both types have a destructive effect on the correlation of a frame pair. Destructive interference occurs when a trough and a peak of the lightwave come together, this is the case when a difference of half a wavelength is found between the two lightwaves. Constructive interference is detected when two peaks or two troughs occur at the same instant.

Figure 11.2 shows the pressure side of the airfoil close to the leading edge. As depicted in Figure 10.17 the light has to travel through glass. The black stripe in the middle of the image in Figure 11.2 is due to scattering of the laser light because of a scratch in the glass plate below. This discontinuity is a function of time driven by the accumulation of particles in the scratch of the glass. Without cleaning the scratch in the glass, the black line in the laser sheet increases, yielding a larger impact on the results at the end of the recording of a set of images. The discontinuity in the laser sheet has a major effect on the correlation in that specific area. Other discontinuities close to the wing are reflections of the light on the wing surface and the transition strip. This effect is destructive for the to be determined velocity vectors close to the surface. In order to reduce the impact of this discontinuity use can be made of the subtraction of minimum intensity of a set of observations recorded progessively in time. The routine searches for the minimum intensity (expressed in counts), and subtracts this intensity from all the observations in the set. This routine reduces the local high intensities in the image and thereby highlights the previously undetected particles. This processing technique improves the result of the

final correlation method.

Figure 11.3 shows the image taken at the leading edge of the wing. The laser light enters the section from below and is reflected on the mirror on the upper windtunnel wall. The reflected lasersheet has a low intensity compared to the non-rfelected sheet at the right hand side of the image. Along the path the laser has to travel, power is dissipated. So the longer the path of the laser light, the lower the intensity will be. The loss of power translates in a difference of intensity, which is clearly visible in Figure 11.3. Also visicle in the image is the reflection found at the leading edge, which can be reduced by applying subtraction of the minimum intensity over a set of images.

By analysis of the three images (Figures 11.1 to 11.3) several important features in the images that deteriorate the results in this experiment are described. In general the effect of travelled path of the laser light, the interference effect due to the use of the mirror and the effect of accumualtion on the mirror apply on the fields of view on the suction side of the wing. The largest reflections are found at the leading edge. Another type of reflection is found at the trailing edge, where the flap angle β dictates the angle of incidence of the light with the surface and in this way the intensity of the reflection. For both the leading edge field of view and the trailing edge field of view, transition from high to low power regions exist. At these transitions the correlation function will perform poorly without preprocessing of the images.

As prescribed one of the preprocessing techniques is the subtraction of the minimum intensity, this is to minimize the high reflections at the surface. Another technique is to homogenize the laser intensity by normalizing the laser intensity of a Field of View and thereafter stretching. Equation 11.1 is applied, where N(x) is the normalized local intensity as found in the set of images on location (x) and $I_{min}(x)/I_{max}(x)$ the local sliding minimum and maximum intensity over a set of images.

$$I_{normal}(x) = \frac{N(x) - I_{min}}{I_{max} - I_{min}} \tag{11.1}$$

where

$$N(x) = \frac{I(x) - I_{min}(x)}{I_{max}(x) - I_{min}(x)}$$

Equation 11.1 can be interpreted as firstly calculating the local normalized intensity. Thereafter, the minimum and maximum of the entire frame of one observation is calculated, and inserted in Equation 11.1. Effectively, the images are homogenized in terms of intensity and in this way better correlation results are obtained. An example is given in Figure 11.4.

Per field of view the intensity level changes in time as a function of the position of the Field of View and the described phenomena occuring like accumulation of particles on the mirror. On the wake field of view an analysis is given how these methods have an influence on the acceleration of the flow, which is an important term in the evaluation of the unsteady force due to the actuation of the flap.

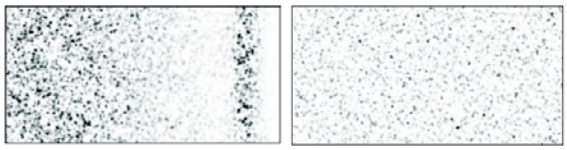

Figure 11.4: The normalization of intensity leads to a homogeneous distribution of intensity (LaVision [2005])

11.2 Postprocess of PIV data

Davis is a software package by LaVision responsible for both the preprocessing (e.g. minimum subtraction) and the postprocessing (correlation) of images obtained by Particle Image Velocimetry. Davis includes different correlation schemes for the evaluation of the data. In order to find the best scheme for the experimental data in relation with the force evaluation method, some criteria need to be setup. The peak ratio is a byproduct of the correlation method used for the determination of the forces. This ratio determines how well the data is correlated. By a matrix of peak ratios one can determine whether a defined integration contour (see Chapter 9) will result in a proper force determination. With this knowledge the position of the integration contour can be optimized.

In relation with the momentum flux method, a parameter susceptible to noise, is the time dependent term in the flux equation. For very small time steps the noise becomes significant and hence the time dependent force in the flux equation cannot be determined properly. Since a sinusoidal motion is divided into multiple phases the time in between two consecutive velocity fields decreases as the frequency of the motion is increased. The quality of the time dependent term decreases due to smaller time steps, therefore it is more difficult to analyze highly unsteady behaviour.

Two methods are used for the validation of the PIV data of this experiment, which are the evaluation of the peak ratio, the quality analysis of the time dependent term as a function of frequency. Before this analysis is performed, the pairs of images need to be correlated, which is described in the next section.

11.2.1 Mathematical correlation models by Davis

There are two main methods for the evaluation of the vectorfield. One method is sequential cross correlation in which two consecutive frames are cross correlated based on the scheme as depicted in Figure 11.5. Since phase locked averaging is used multiple samples exist per field of view and hence it is possible to do a statistical analysis on the results, by calculating the mean and the fluctuation (standard deviation). High fluctuations show that either a highly turbulent phenomena is measured or that non-negligeble noise exist in the data set.

The second method is the sum of correlation (Figure 11.6) which is normally used when the illumination by the laser sheet is non homogeneous or when parts of the images are out of focus. By using this method generally better results are obtained with low quality

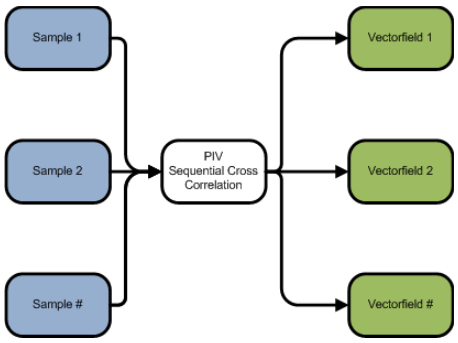

Figure 11.5: Sequential cross correlation; each image corresponds with one vector field

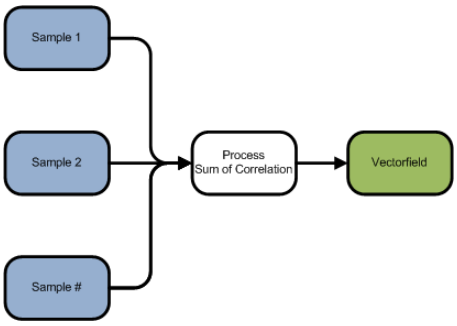

Figure 11.6: Sum of correlation; each set of images corresponds with one vector field

samples. However, statistical analysis on each observation/sample is not possible since all the greytype images, which only show the particles and not the vectors, are "averaged" and only one vector field is obtained.

In both methods it is possible to apply multi pass mode which allows for more accurately defining the velocity vectors and to avoid spurious vectors because of a lack of information for correlating the pair of images. In essence the method uses the velocity calculated from the pair of images of the first pass (iteration) to shift the correlation window in the second image of the pair of images corresponding to this calculated velocity. This ensures that the same particles are correlated with each other even if small interrogation windows are used. The principle is shown in Figure 11.7.

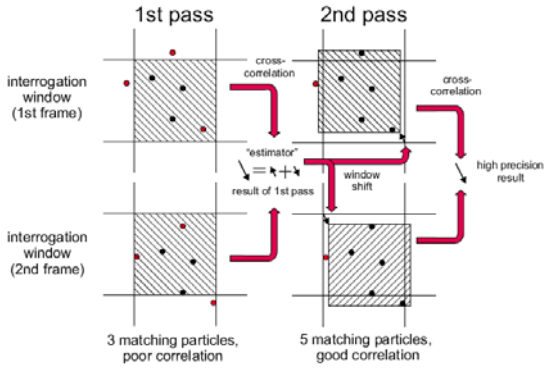

Figure 11.7: The multipass principle for defining accurate velocity vectors

The correlation function for all the methods used in this thesis is defined as the 'standard' method with zero padding according to the Davis manual. The correlation function is described in Equation 11.2.

$$C(dx,dy) = \sum_{x=0,y=0}^{x<n,y<n} I_1(x,y)I_2(x+dx,y+dy), -\frac{n}{2} < dx,dy < \frac{n}{2} \tag{11.2}$$

C gives the correlation strength between the two interrogation windows. Where n is the size of the interrogation window and usually also the size of the correlation plane, where $\frac{n}{2}$ is the maximum displacement computed. The method described is the standard cyclic FFT-based algorithm used by LaVision [2005]. In this case cyclic means that the correlation is computed as if the the two interrogation windows are repeated again in 2D-space which is then used for the computation of the correlation strength C. In order to reduce computational time a 2D fast fourier transformation is used. The complex 2D-FFT is calculated for each sample of the pair of images. Thereafter the two results are multiplied complex conjugated and the inverse FFT is computed, which is then in the form of Equation 11.2. A disadvantage of this method is that a weighting is introduced on basis of a displacement (0,0), in which the weighting is 1. For a half window displacement the weighting factor is half and for full window displacement the factor is 0. The principle of this is depicted in Figure 11.8, in which the grey area is the area that is correlated. "The right half of the first interrogation window is actually correlated with the wrong left half of the other interrogation window, only adding unwanted false random correlation noise" (LaVision [2005]).

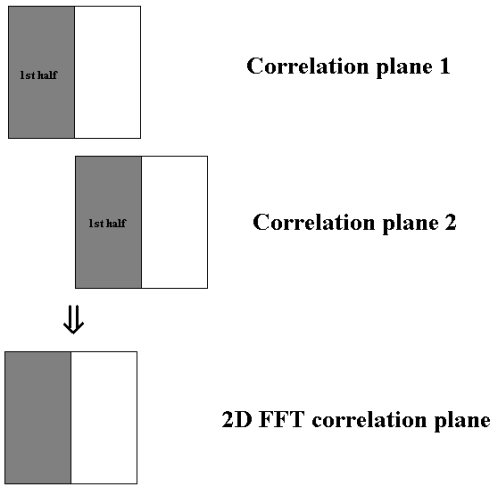

Figure 11.8: The weighting factor for a 16 pixel shift is half

In order to not introduce correlation noise, the window size should be big enough to accomodate possible large vectors. If the approximate vector length is known one can set the windowshift to this number, in which the vectors around this shift are weighted more than others. In this case the FFT method performs well. Another disadvantage is that the method introduces a bias towards smaller displacements, because of a shift of the Gaussian correlation peak to one which is slightly shifted. A peak locking bias effect exists due to the fact that the measured displacement is shifted to the next integer. The peak locking bias limits the accuracy of the vector computation. In general, this method should only be used if displacements less than 1/3 window size are found. Analyzing the pixel shift of the testrun per acquisition shows that this is a suitable function for correlation of the images LaVision [2005].

"The Whittaker algorithm is an option for image reconstruction. This reconstruction

type avoids any smoothing of the image (if the particle diameter is above 1 pixel) so that it should be able to restore the original image without loss of information if you apply the inverse transformation. The principle of the Whittaker reconstruction has been developed in signal theory. This explains how to rebuild signals of a limited bandwidth (i.e. images with structures of diameter ≥ 1 pixel) from sampling points (i.e. pixel information) with subpixel accuracy **?**." "The sampling theorem states that, under certain limiting conditions, a function x(t) can be recovered exactly from its samples, $x[n] = x(nT)$, by the WhittakerShannon interpolation formula denoted in Equation 11.3":

$$x(t) = \sum_{n=-\infty}^{\infty} x\,[n] \cdot \sin c\left(\frac{t - nT}{T}\right) \tag{11.3}$$

where $\mathrm{sinc}(x) = \frac{\sin(\pi x)}{\pi x}$ is the normalized sinc function, $T = 1/fs$ is the sampling interval and f_s is the sampling rate. Limitations for the use of the Whittaker-Shannon interpolation are the existence of the Fourier transform for a maximum frequency larger than twice the bandwidth which is larger than 0. "The interpolation formula reconstructs the original signal x(t), as long as these conditions are met. Otherwise, aliasing occurs; that is, frequencies at or above fs/2 are erroneously reconstructed." (Whittaker E.T. [1915])

In the correlation procedure 32x32 pixel interrogation windows are selected. One interrogation window corresponds with 1%c. In order to increase the resolution, an overlap of 50 % is applied. This overlap is explained by Figure 11.9, where the red box overlaps the original interrogation windows, producing an extra vector in the middle of the red box.

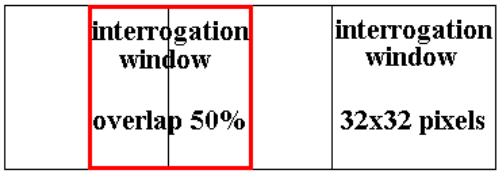

Figure 11.9: The interrogation window with 50% overlap is indicated with the red box. The original 32x32 interrogation windows are indicated in black.

11.2.2 PIV postprocessing errors

Theoretical PIV error

With the theory on subpixel interpolation for the determination of the correlation peak described in LaVision [2005], the error of the postprocessing routine can be determined. The error in the velocity due to spatial errors and timing errors is derived in Equation 11.4. Suppose a timing inaccuracy ($\sigma_{\Delta t}$) of 1 ns exists in which a time resolution between the two frames is dictated to be of the order of 10^{-5} s, the error is of the order of 10^{-4} s. The spatial error, $\sigma_{\Delta x}$, is between 0.1 and 0.2 pixels. The interrogation window size is set to 32 pixels, thereby, through Equation 11.5, the error is determined to be 1.25 % in the velocity components.

$$\begin{aligned}\bar{U} = \frac{\Delta\bar{X}}{\Delta t} \Rightarrow \varepsilon_U &= \sqrt{\left(\frac{\partial U}{\partial \Delta t}\varepsilon_{\Delta t}\right)^2 + \left(\frac{\partial U}{\partial \Delta x}\varepsilon_{\Delta x}\right)^2} \\ = \sqrt{\left(\frac{\Delta x}{\Delta t^2}\varepsilon_{\Delta t}\right)^2 + \left(\frac{1}{\Delta t}\varepsilon_{\Delta x}\right)^2} &= \frac{1}{\Delta t}\sqrt{\left(U\varepsilon_{\Delta t}\right)^2 + \left(\varepsilon_{\Delta x}\right)^2} \\ \frac{\sigma_U}{U} = \sqrt{\frac{1}{\Delta t^2}\left[\sigma_{\Delta t}^2 + \frac{\sigma_{\Delta x}^2}{U^2}\right]} \Rightarrow \frac{\sigma_U}{U} &= \sqrt{\left(\frac{\sigma_{\Delta t}}{\Delta t^2}\right)^2 + \left(\frac{\sigma_{\Delta x}}{U}\right)^2}\end{aligned} \tag{11.4}$$

$$\frac{\sigma_U}{U} = \frac{0.1}{(1/4)\cdot 32} = 1.25\% \tag{11.5}$$

For interrogation windows of 64x64 the error obviously reduces, because the localization with respect to the size of the interrogation window is on a different scale. The error of the position of the correlation peak is reduced by half for the cost of lower spatial resolution.

Time derivative analysis

In this section the influence of the post proccesing technique on the acceleration term is investigated. Several methods denoted in Table 11.1 are evaluated in order to see what the influence is of the selection of post processing function on the quality of the acceleration related to the time dependent term of the flux equation. For convenience the determination of the $\frac{du}{dt}$-term is denoted in equation 14.2. By applying this equation an error proportional to the timestep itself is introduced in the acceleration term.

$$\frac{du}{dt} = \frac{\vec{u}_{t+\Delta t} - \vec{u}_t}{\Delta t} + O(h) \tag{11.6}$$

On basis of the analysis of the error due to the postprocessing function, the randomness of the vectors is related to the error introduced in the velocity field by the inaccurate detection of the correlation peak. Suppose the error in the velocity for both velocity fields determining the acceleration of the flow is 1.25 % (see previous section), a maximum total error can be up to 2.5 % for the difference velocity of the vector for the two time instances. In this case a timestep of 0.005 and a velocity of 21 m/s are considered.

$$\Delta\frac{du}{dt} = \frac{2.5\% \cdot U}{\Delta t} = 100 m/s^2 \tag{11.7}$$

Using an interrogation window of 32x32 pixels the error in the acceleration can be as large as 100 m/s^2 at a velocity of 21 m/s. By using different schemes for the determination of the correlation peak the subpixel accuracy can be minimized and hence a smaller error can be achieved. The time step is an important parameter for the error as shown in Equation 11.7. Larger time steps imply smaller errors. Another way of reducing the error is the usage of a second order interpolation scheme to determine the acceleration vector. This thesis is confined to the analysis of the time dependent term on a first order scheme (Equation 14.2) and hence the variables for the determination of the error are the method determining the subpixel accuracy and the timestep. Another parameter determining the error is the velocity. In case low velocities, associated with small pixel shifts, are observed

	method 1	method 2	method 3
Correlation method	Sequential cross correlation	Sum of correlation	Sequential cross correlation
multi pass (1st)	64 x 64 0 overlap	64 x 64 0 overlap	64 x 64 0 overlap
multi pass (2nd)	32 x 32 50 overlap	32 x 32 50 overlap	32 x 32 50 overlap
correlation function	'standard'	'standard'	'standard'
Image correction	yes	yes	yes
Whittaker reconstruction	no	no	no
Minimum intensity subtraction	no	no	yes

	method 4	method 5	method 6
Correlation method	Sum of correlation	Sequential cross correlation	Sequential cross correlation
multi pass (1st)	64 x 64 0 overlap	128 x 128 0 overlap	64 x 64 0 overlap
multi pass (2nd)	32 x 32 50 overlap	64 x 64 50 overlap	32 x 32 50 overlap
correlation function	'standard'	'standard'	'standard'
Image correction	yes	yes	yes
Whittaker reconstruction	no	yes	yes
Minimum intensity subtraction	yes	no	no

Table 11.1: Particle Image Velocimetry postprocessing methods for the determination of the velocity vectors

the error of the correlation method becomes more dominant.

One field of view contains the near wake up to 30 % of the chord on the lower side of the wake. Most of the unsteady effects, which is created by the actuation of the flap, is found in the wake. Therefore, an analysis on the acceleration of the flow (time dependent term in the flux equation) is peformed in this specific field of view. Several methods influencing the subpixel accuracy are demonstrated in Table 11.1. The dependency of the error as a function of the method is investigated.

The results of the different methods from Table 11.1 are visualized in Figure 11.11. In order to analyze this data in terms of quality some qualifications need to be prescribed. A measure of the noise in the data set is the mathematical modelling of the randomness observed. In order to determine the randomness a statistical analysis is performed per obtained acceleration field. The results are shown in Figure 11.10. The statistical analysis integrates the random behaviour of the flow *and* the random noise. Since the flow phenomena is not known it is difficult to state what random noise is and what a physical phenomenon is. As stated the field of view containing the wake is used for evaluation of the time dependent term. Hundred samples of the flow are taken and averaged in case of sequential cross correlation. For the sum of correlation hundred samples are used as input. The acquired averaged vectors per field can be expressed in a mean and standard deviation of the observed acceleration, giving an indication on the performance of a specific method.

From Figure 11.10 it can be stated that the mean of the acceleration for all methods is of the same order, except for method 2. On basis of the analysis performed in Section 11.2.2 in relation with Equation 11.5, the 64x64 interrogation window would give the best result in predicting the actual velocity, since the error is low compared to the higher resolution methods (assuming optimal pixel shifts). The downside of this method is that the resolution is relatively low and that averaging of the flow is proportional to the area of the interrogation window, yielding an averaging four times larger than a 32x32 interrogation window. The averaging in the interrogation window might suppress the fluctuations on the acceleration present in the flow. However, independent of the method the mean of the acceleration of the flow over the entire flow domain, in reference with Figure 11.10, is best predicted by the low resolution method (method 5). By knowing this, method 2 does

not seem to predict the flow well, since the mean shows a large difference compared to method 5. Methods 2 and 4 show the largest fluctuations, which seemingly has to do with fact that both methods are based on the sum of correlation. This can be explained by the fact that for a very turbulent or unstable vector field, the summation of the correlation planes might not lead to a single correlation peak (LaVision [2005]). This can be solved by taking more samples to obtain a more averaged flow field, such that a more coherent correlation plane is obtained. In this case the second correlation peak reduces compared to the first correlation peak, yielding better results.

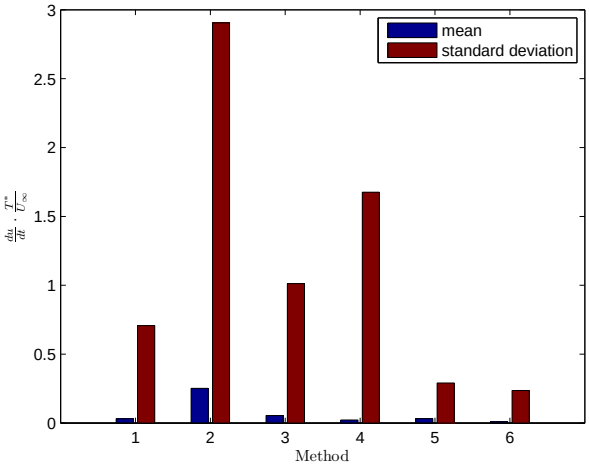

Figure 11.10: The mean and standard deviation of the acceleration for FOV 'wake'

From the deviations it can be concluded that the choice of method used for the determination of the acceleration of the flow has a large influence. Method 1 shows a distinct area of flow acceleration in Figure 11.11(a). The second and fourth method shows a less pronounced wake, this is likely the influence of the second peak in the correlation plane due to the absence of a large number of samples. In this case no coherent correlation map can be obtained. Comparing method 1 and method 3 the same wake structure is obtained. The difference between the two methods lies in the fact that method 3 uses a pre processing function, that suppresses reflections close to the surface. The effect of the pre processing is visible by comparing the right hand side of 11.11(a) and 11.11(b), where Figure 11.11(a) shows a much more pronounced flow structure. Method 5 and method 6 make use of Whittaker interpolation, which should increase the accuracy of the determination of the correlation peak.

The correlation peak ratio describes the correlation strength of a pair of images is. In general it can be stated that the larger the peak ratio, the more accurate the velocity vectors are determined. Table 11.2 and 11.3 show the comparisons between the methods which make use of sequential cross correlation. The tables denote the number of correlation peaks that are larger for a certain method compared to another method. This analysis is performed over an entire Field of View and the distinct wake region of that same Field of View.

In the tables, the method that has the largest number of largest peaks in this specific field of view is indicated a ratio showing the relative difference between the two selected

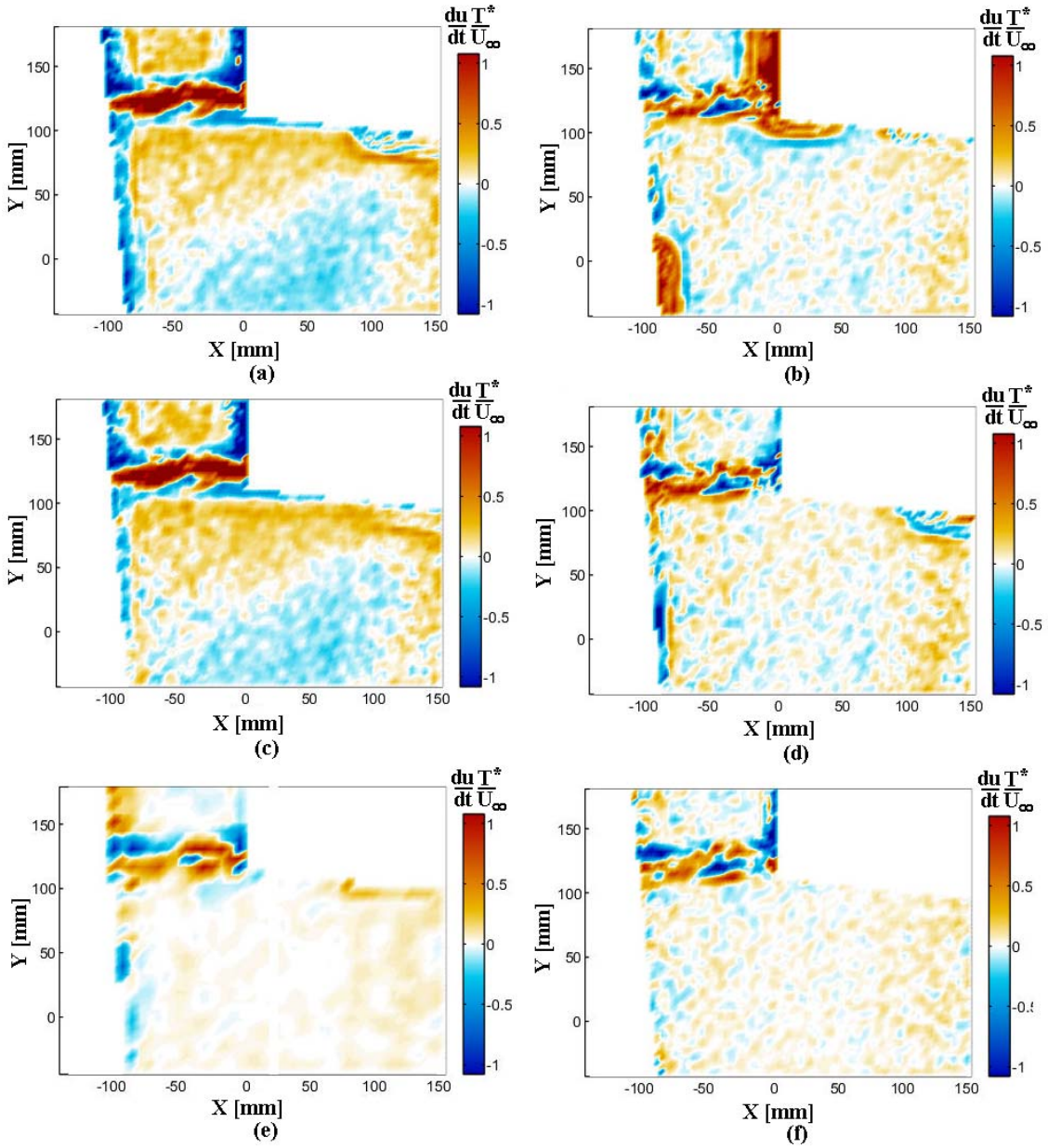

Figure 11.11: The post processing influence on the acceleration of the flow in the wake Field of View; (a) method 1: sequential cross correlation 32 x 32 50% overlap; (b) method 2: sum of correlation 32 x 32 50% overlap; (c) sequential cross correlation 32 x 32 50% overlap, minimum intensity correction; (d) method 4: sum of correlation 32 x 32 50% overlap, minimum intensity correction; (e) method 5: sequential cross correlation 64 x 64 50% overlap, Whittaker reconstruction; (f) method 6: sequential cross correlation 32 x 32 50% overlap Whittaker reconstruction

	method 1	method 3	method 5	method 6
method 1	X	m1 (0.58)	m5(0.94)	m6(0.77)
method 3	X	X	m5(0.93)	m6 (0.78)
method 5	X	X	X	m5 (0.95)
method 6	X	X	X	X

Table 11.2: Peak ratio method comparison for entire field of view

	method 1	method 3	method 5	method 6
method 1	X	m1 (0.54)	m5(0.92)	m6(0.75)
method 3	X	X	m5(0.92)	m6 (0.75)
method 5	X	X	X	m5 (0.90)
method 6	X	X	X	X

Table 11.3: Peak ratio method comparison for wake region

methods. For example if method 1 and method 6 are compared, the table states m6 (0.77), saying that method 6 performs best with 77% of the peaks larger than method 1. From both tables it becomes clear that method 5 with the lowest resolution shows the best result at the cost of low resolution. In general it can be stated that the grid resolution increases at the cost of the time resolution. Method 6 performs best with an interrogation window resolution of 32x32, compared to the other methods and seems to be the best candidate for determining the acceleration of the flow. Figure 11.12 shows the peak ratio over one entire field of view.

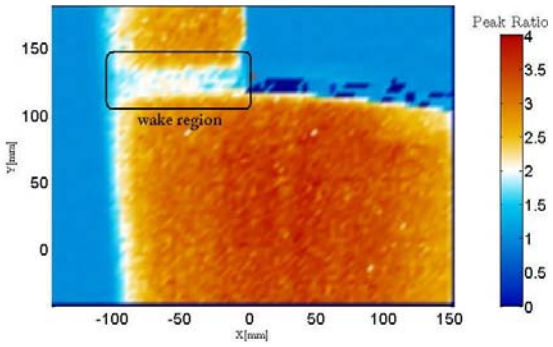

Figure 11.12: The correlation peak ratio of the wake domain evaluated by method 1

It shows that the region of the wake, is the region with the lowest peak ratios. This stems from the fact that lower pixel shifts apply and the error of the method becomes more dominant. This is the case, independent of the method used.

11.3 Reconstruction of the flow domain

From the experimental setup it follows that the flow domain is partitioned in mutliple Fields of View. Every FOV is is associated with the recording of a distinct region in the flow domain. Figure 11.13 shows the partioning of the flow domain of this experiment.

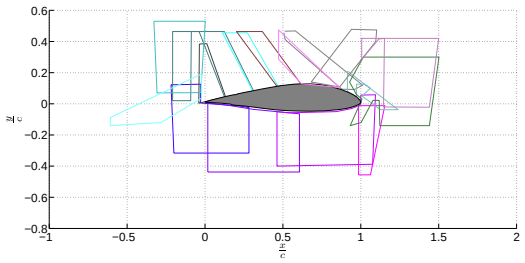

Figure 11.13: The partitioned flow domain that is reconstructed from the separate Fields of View.

In order to gain insight in the velocity over the entire flow domain a reconstruction of the FOVs is required, which is known as the stitching process. Before the actual stitching can be performed the separate velocity fields per FOV are processed according to the flow chart in Figure 11.14.

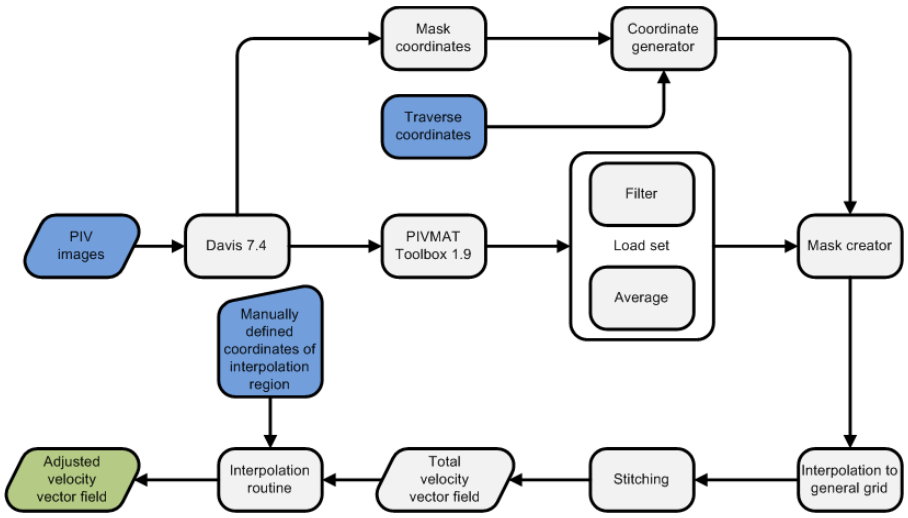

Figure 11.14: Flowchart for the reconstruction of the flow domain, where the blue boxes indicate the user input and the green box is the output of the process.

In order to translate all the velocity data into a general grid, a program is written on basis of the PIVMAT Toolbox written by La Vision **?**. This toolbox contains a dynamic link library which is able to convert the Davis vector fields into a MATLAB structure. A program is written which makes use of this Toolbox and interpolates and stitches the data into a general reference frame. The principle of this program is depicted in Figure 11.14. Once the (pre-processed) PIV images are subjected to the correlation methods in Davis, the vector fields are obtained. The different vector fields of the different fields of view are loaded by making use of the PIVMAT Toolbox. Per set of images of hundred samples the PIVMAT Toolbox is able to load and average all the samples. In this proces interpolation routines and filters on the vector field can be applied. These different operations in this program are confined to the interpolation of missing data and the application of a median filter. Interpolation of missing data is only applied if gaps exist in the field of view considered. The routine makes use of nearest neighbour principle and uses a weighted average to interpolate on basis of the surrounding data.

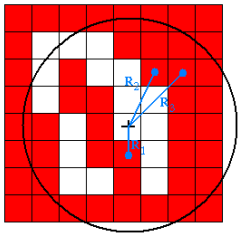

Figure 11.15: Interpolation procedure in which the red cells indicate the availability of proper velocity information, where the white cells indicate the lack of proper velocity information

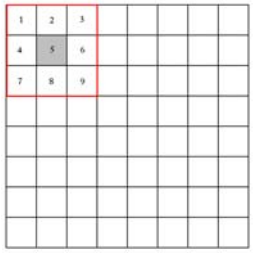

Figure 11.16: The principle of the median filter is summarized by taking the median of the red interrogation window

Figure 11.15 shows a grid, where the white cells indicate the missing or erroneous data points. At each red cell, velocity information is availaible. The circle contains the data points which should be used for the interpolation of the cell indicated with the cross. The radius to the neighbouring cells contained within this circle is determined as indicated by the blue lines. All the velocity information and corresponding radii are used as input in Equation 11.8, with $w_i = \frac{1}{R_i^3}$ and N the number of cells used for interpolation.

$$U_{interp} = \frac{\sum_{i=1}^{N} u_i \cdot w_i}{\sum_{i=1}^{N} w_i} \tag{11.8}$$

This equation holds for both the x- and y-component of the velocity. Dependening on the size of the circle, the interpolation uses the trend observed within this circle. This interpolation method works independently on the size of the area containing erroneous data.

The median filter is a filter which is used in digital processing to reduce noise in a measurement. For data of 2 dimensions, a window of 3x3 entries shifts over the domain. The values in this window are ordered from the smallest value to the largest value. The middle value is denoted as the median. In probability theory and statistics, the median is denoted as the numeric value separating the higher half of a sample, a population, or a probability distribution, from the lower half. The median of the set of 9 numbers replaces the value in the middle of the window of 3x3 entries Figure 11.16.

After the filter process the (filtered) velocity vector field for each specific FOV is translated to the general grid, where use is made of the position of the cameras and the coordinates based on the regions in the images in which particles are properly illuminated and hence accurate velocity vectors exist. The area with the correct velocity information is referred as the mask of the image.

Every field of view is translated to a predefined general grid only containing the data of that specific Field of View and all other entries set to 0. The reconstruction of the the entire flow domain is performed by adding all the separate grids containing the specific

Fields of View. The overlap regions of multiple FOV's are identified an treated separately. Coherent velocity structures of the overlapping regions should exist; i.e. if a discrepancy in both the x- and y-velocity is less than 1 percent, the mean of the velocity vectors is taken as the correct result. If this is not the case (e.g. due to difference in image quality) the user can apply an overruling criteria in which the dominancy of a specific FOV in that interpolation region can be specified. In that case the best data is used for creating the velocity fields.

With the previous step an entire velocity field for a specific time step is acquired. In the case that illumination patterns can change as described in section 11.1, the possibility exists that the user has to redefine the mask for each case. In this experiment the change in the definition of the different masks is minor and hence only small regions confined to several pixels at the interfaces of two fields of view show errors in time. These errors are filtered out by applying a post interpolation of data on basis of visual inspection. Other deteriorating features in the PIV images as described in Section 11.1 also give errors in the velocity vector field. In these regions the same post interpolation process based on Figure 11.15 is applied.

11.4 Determination of the velocity field derivatives

The program according to the flowchart shown in Figure 11.14 outputs the velocity field in vector format (u,v). Analyzing Equation 9.2, yields that both time and spatial derivatives are needed for the determination of the force vector. The derivatives are obtained by making use of the gradient function of Matlab. The gradient is defined in Equation 11.9.

$$\nabla F = \frac{\partial F}{\partial x} i + \frac{\partial F}{\partial y} j \tag{11.9}$$

For the edges Matlab uses a forward difference scheme denoted in Equation 11.10, with an associated error of the order $O(h)$, where h is the stepsize.

$$f'(x) = \lim_{h \to 0} \frac{f(x+h) - f(x)}{h} + O(h) \tag{11.10}$$

The central difference scheme is used for the interior points, with an error of the order $O(h^2)$. Equation 11.11 shows that twice the stepsize is needed for determination of the derivative in the central point.

$$f'(x) = \lim_{h \to 0} \frac{f(x+h) - f(x-h)}{2h} + O(h^2) \tag{11.11}$$

For the second order derivatives the gradient function is applied 2 times, yielding that Equations 11.10 and 11.11 also hold for the second step.

For the time step only a forward difference scheme is applied implying that an error of the order of the time step is found. Depending on the time step the truncation error can be reduced. In the experiment the smallest time step is $\Delta t = 0.005$, implying that

the error on the acceleration terms is at least of the same order of the time step. As stated in Section 11.2.2 the error in the acceleration is dominated by the error due to the correlation. Hence the impact of using a finite difference scheme with a higher order only yields better results, when the correlation error is reduced.

11.5 Visualisation of flow quantities

The velocity, vorticity and acceleration, which are visualized for case 4 (k=0.2,β=3 $\pm$ 3) at ϕ = 90 deg, 180 deg, 270 deg 360 deg in Figures 11.17 to 11.28 are inputs for the momentum flux equation. As discussed the quality of the velocity and its derivatives reflect the error in the

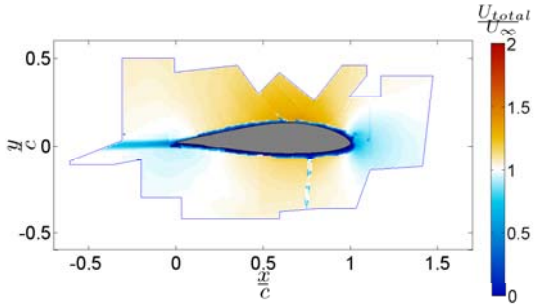

Figure 11.17: ($k = 0.2$, $\beta = 3 \pm 3$ deg, $\phi = 90$ deg)

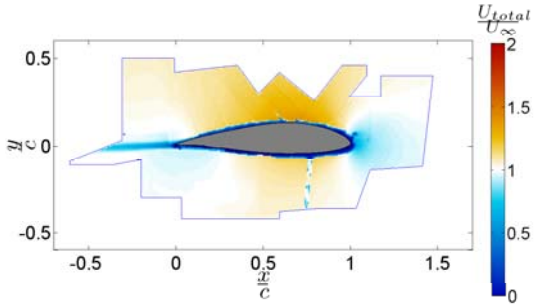

Figure 11.18: ($k = 0.2$, $\beta = 3 \pm 3°$, $\phi = 180°$)

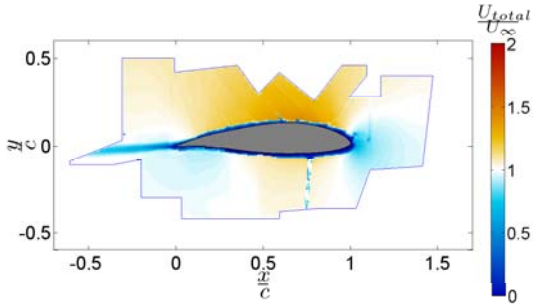

Figure 11.19: ($k = 0.2$, $\beta = 3 \pm 3°$, $\phi = 270°$)

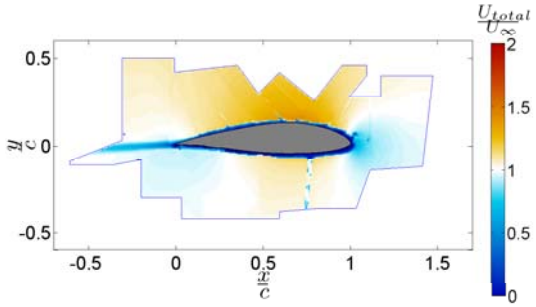

Figure 11.20: ($k = 0.2$, $\beta = 3 \pm 3°$, $\phi = 360°$)

The velocity is scaled by the freestream velocity. Figures 11.17 to 11.20 show the total velocity at the extreme positions of the flap. The entire set of images is found in Appendix B. The velocity fields show maximum velocities $1.3 \cdot U_\infty$ at the suction side of the airfoil. The figures reveal a change in velocity topology as a function of ϕ. By analyzing the figures carefully, one can detect that the low velocity region at the leading edge moves up and down as a function of ϕ. The same is detected at the trailing edge, where the velocity profile follows the flap with a lag due to the unsteadiness of the flow. Zooming in on Figure 11.18 irregularities in the flow are found on the edges of the fields of view, due to low quality PIV data. At the stagnation point the resulting velocity shows an irregularity due to reflection of the transition strip.

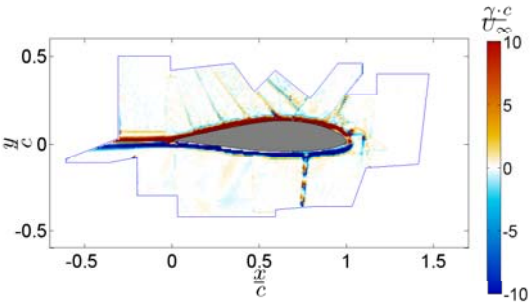

Figure 11.21: ($k = 0.2$, $\beta = 3 \pm 3°$, $\phi = 90°$)

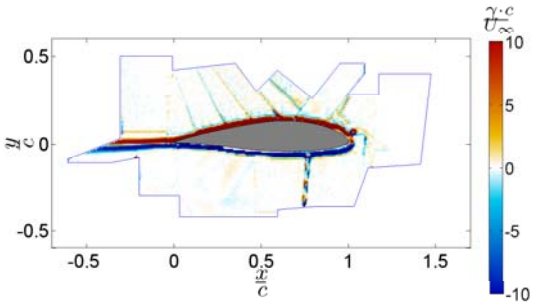

Figure 11.22: ($k = 0.2$, $\beta = 3 \pm 3°$, $\phi = 180°$)

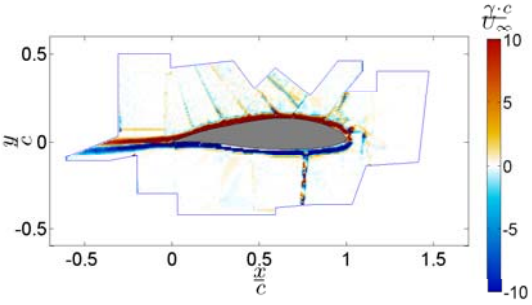

Figure 11.23: ($k = 0.2$, $\beta = 3 \pm 3°$, $\phi = 270°$)

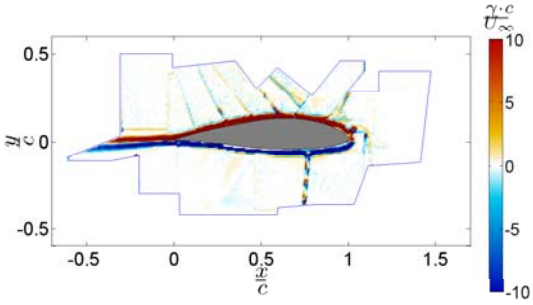

Figure 11.24: ($k = 0.2$, $\beta = 3 \pm 3°$, $\phi = 360°$)

Figures 11.21 to 11.21 reveal that the same reflection causes the introduction of artifical vorticity. Furthermore a considerable amount of noise exists, which is clear from the observation of similar vorticity patterns for all ϕ at the lower part of the flow domain. The wake shows clearly the large gradient in vorticity between the upper and lower surface of the airfoil, where the vorticity reduces for decreasing $\frac{x}{c}$.

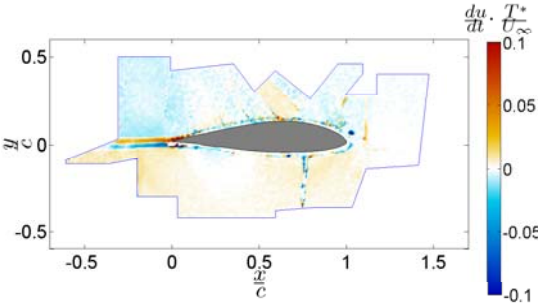

Figure 11.25: ($k = 0.2$, $\beta = 3 \pm 3°$, $\phi = 90°$)

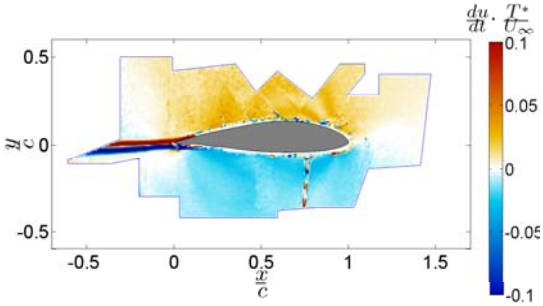

Figure 11.26: ($k = 0.2$, $\beta = 3 \pm 3°$, $\phi = 180°$)

The flow acceleration is determined by taking the difference between two consecutive velocity fields and division by the elapsed time between the acquisition of the two frames. As can be seen large noise levels exist where the suction side and the field of view containing the wake are affected the most. The time interval corresponds to $\Delta\ \phi_t$=45°. The time resolution of ϕ_t=5° is inappropraite due to very high noise levels. The wake shows

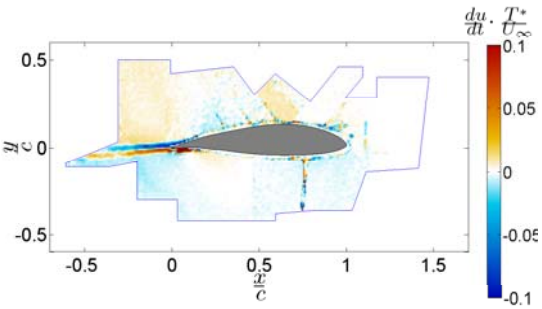

Figure 11.27: ($k = 0.2$, $\beta = 3 \pm 3°$, $\phi = 270°$), $\Delta\ \phi_t$=45°

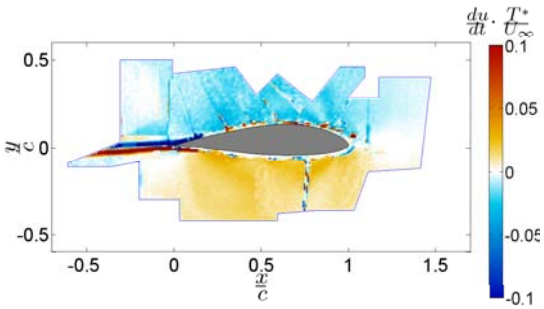

Figure 11.28: ($k = 0.2$, $\beta = 3 \pm 3°$, $\phi = 360°$), $\Delta\ \phi_t$=45°

the highest temporal change in the velocity as illustrated in Figures 11.25 to 11.28. In the extreme flap up and flap down position ($\phi = 90$ and $\phi = 270$) the acceleration of the flow is small compared to the positions in which the flap accelerates crossing the equilibrium position ($\phi = 180$ and $\phi = 360$).

Chapter 12

The experimental force results

This chapter evaluates the force results on basis of the velocity fields that are obtained according to the procedure in Chapter 11. In order to understand the influence of the unsteadiness level k created by the oscillating flap, the steady and unsteady results are compared. Insight in the associated error is required, in order to understand whether the trends in the determined lift and drag are correct.

Section 12.1 describes the general considerations for the determination of the forces in reference with chapter 9 in which the background of the presented methodology is found. Section 12.2 shows the results of the steady case ($k = 0, \beta = 0, 2, 4, 6$). The unsteady results are presented in Section 12.3. Section 12.4 is devoted to the comparison of the steady and unsteady results. Thereby the unsteady force amplitude and phase shift as explained by Theodorsen's function which is described in Chapter 5, is determined. In Section 12.5 insight is created in the variety of force determination methods that can be applied. All the force determination methods are presented with an indication of the fluctuation of the force. In Section 12.5.3 an analysis is performed on the sub components of the force.

12.1 General considerations on the momentum flux force evaluation

On basis of the flowfields acquired through the process demonstrated in the previous chapter, the forces can be determined on basis of the acquired velocity fields. Using the theory as described in Chapter 9 the evaluation of the forces is performed for the cases described in Table 10.1, which are the steady case at $\alpha = 0/\beta$=0,2,4,6 and the unsteady cases for k=0.1/$\beta = 3 \pm 3$ (case 2), k=0.2/$\beta = 1 \pm 1^\circ$ (case 3) and k=0.2/$\beta = 3 \pm 3$ (case 4). Fifteen contours on which the force evaluation can be done are drawn in the domain as depicted in Figure 12.1.

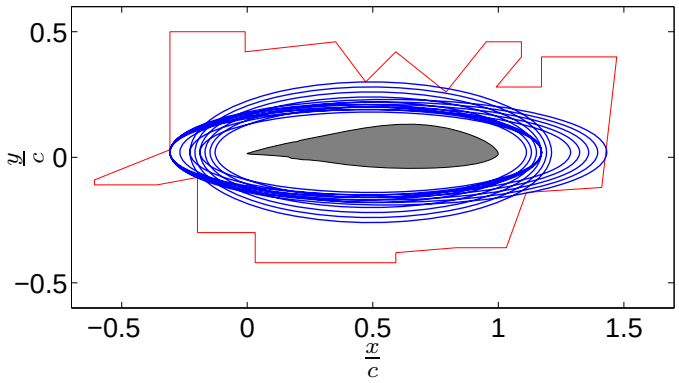

Figure 12.1: The momentum flux equation is evaluated over all the blue contours; the area bounded by the red line is the flow domain in which the velocity data is experimentally determined.

By applying multiple contours the statistical error reduction method is used as demonstrated in Section 9.5. However, the topology of the flowdomain is differs from the ideal homogeneous error due to areas with low quality data. Therefore, the contour positions need to be selected with care. The position of the contours shows that the wake is captured at different positions. The contours do not cross the wake close to the trailing edge, because of the coarseness of the grid. At these high gradient regions large errors might exist and are therefore not included in the procedure for the force determination. As indicated by the red contour line in Figure 12.1 the flow domain is relatively small. As known from the analysis in Chapter 9, the best results of the force are obtained in the outer region of the flow domain. On basis of the experimental data the outer region cannot be addressed as much as in the dummy case in Chapter 9. The contours defined, cross regions close to the airfoil, where relatively large gradients exist, as well as regions several percentages of the chord away from the airfoil, where gradients are less pronounced. Each differently defined contour addresses a different region with different errors. Increasing the number of contours, results in a better understanding of the accuracy of the force determination procedure in relation with the acquired velocity data. This information can consequently be used to improve the contour definition in order to obtain more reliable force results. For example, Section 9.7.4 shows that a specific distribution of contours in the inner region shows reasonable accuracies in terms of lift force prediction.

In order to capture the drag as a result of the aerodynamic phenomena (vorticity and acceleration) in the wake, the resolution of the wake should be such that these phenomena are well defined. Especially the vorticity and the acceleration of the flow need to have a fine spatial and temporal resolution to be well captured. The spatial resolution is 3.5mm x 3.5mm and the temporal resolution for the definition of the time term is $\Delta\phi_t = 45$ deg ($k = 0.2$ corresponds a timescale $t_s = 0.05s$ and $k = 0.1$ corresponds to $t_s = 0.1s$). The results presented in the upcoming sections show that the resolutions presented are not sufficient to capture the drag accurately. Therefore the focus of the force evaluation is on the lift coefficient.

The total force calculated on each contour should give the same result independent of

the position of the contour. However, the different contributions to the total force (the inviscid term, the time dependent term and the viscous term) will change as a function of contour position. For the unsteady cases, the contribution of the inviscid term, the time dependent term and the viscous term, will also vary in time, causing different values for the error. Thereby the error is a function of time and space.

By applying an averaging of the set of contours, the total lift force is determined. The fluctuation of the mean of the total lift force in this set of fifteen contours shows the uncertainty of the force prediction. This uncertainty is an integrated value of the errors encountered in the acquisition, the postprocessing of the images and the force determination method, excluding the systematic errors appearing in each evaluation of the different contours.

The set of contours shown in Figure 12.1 is used for both the drag and lift determination for all steady and unsteady test cases and phases. The velocity fields obtained through the process denoted in the previous chapter can be subjected to different force determination procedures, which will be discussed in Section 12.5. The force results shown in Section 12.2 to 12.4 are based on the force determination procedure with the highest accuracy.

12.2 Force evaluation in steady conditions

Case 1 ($k = 0, \beta = 0, 2, 4, 6$) is performed in steady conditions, in which the acceleration term in the momentum flux equation is explicitely set to 0, meaning that $\frac{d}{dt} = 0$ and hence the steady momentum flux terms govern the force determination. Equation 12.1 shows the steady form of the momentum flux equation, where the time dependent terms are removed from the general equation as stated in Equation 9.2.

$$\frac{F}{\rho} = \oint_{S(t)} \vec{n} \cdot \gamma_{flux} dS \tag{12.1}$$

$$\gamma_{flux} = \tfrac{1}{2}u^2 I - uu - \tfrac{1}{N-1}u(x \times \Omega) + \tfrac{1}{N-1}\Omega(x \times u) + \tfrac{1}{N-1}\left[x \cdot (\nabla \cdot T)\, I - x\,(\nabla \cdot T)\right] + T$$

Figures 12.2 and 12.3 show the lift coefficient and drag coefficient as a function of flap angle β for the experiment. Figure 12.2 shows an interpolated version of the lift coefficient versus flap angle β. This linear interpolation is performed for $\beta = 2\,\text{deg}$, since the original result shows an unexpected deviation from the linear trend detected in Figure 10.9. The large errorbar associated with this data point indicates that poor velocity data is used for the evaluation of the force and hence an interpolation is justified. In Figure 12.3 an increase in drag with β is detected, which corresponds with the expected trend observed in previous measurements.

The indication of the error in Figures 12.2 and 12.3 on basis of the fluctuation observed in the set of fifteen contours at β = 0,2,4,6 deg illustrate the poor precision of the force

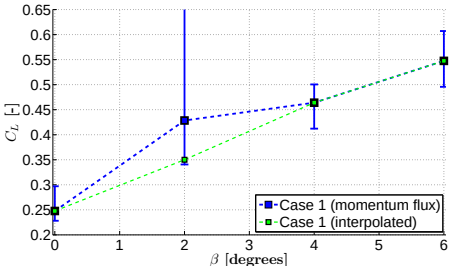

Figure 12.2: Lift force estimation by application of the momentum flux equation

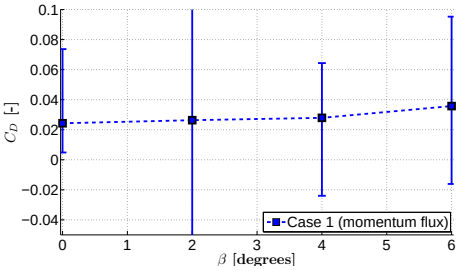

Figure 12.3: Drag force estimation by application of the momentum flux equation

determination tool. Since the drag coefficient is an order of 10^1 smaller than the lift coefficient, the postprocessing error is more dominant and therefore the accuracy in the determination of the drag is less.

12.3 Force evaluation in unsteady conditions

This section deals with the determination of the forces for the unsteady conditions in which one is referred to Equation 9.2. The third integral is the definition of the body acceleration term, which will firstly be discussed.

12.3.1 The body acceleration term

Accelerations of the flap are small and seem to not have a significant contribution ($< 1\%$) to the obtained value for lift. The third integral of Equation 9.2 is denoted in Equation 12.2.

$$\frac{F_{III}}{\rho} = \frac{d}{dt} \oint_{Sb(t)} \vec{n} \cdot (ux) dS \tag{12.2}$$

Analyzing Equation 12.2 shows a multiplication of ux. These terms only hold on the moving boundary induced by the motion of the flap. Since the motion is known, the velocity vector of each vertex on the moving boundary can be calculated through Equation 12.3.

$$\dot{r} = \frac{r_{t_2} - r_{t_1}}{\Delta t} \tag{12.3}$$

The position vector is denoted with r. By subtracting the position vectors at different time instances and dividing by the time interval, the velocity vector at the boundary is obtained. By knowing the position vector as a function of time ux can be calculated over the boundary. Multiplying with the normal component and integrating over the boundary, the results are obtained for different time instances. On basis of the evaluated

integrals as a function of time, Equation 12.4 shows how to obtain the time derivative of the integral. For the evaluation of this term the phases at which PIV acquisition is performed are used, which dictate the time interval Δt.

$$\frac{d}{dt}\int_{S_b} \vec{n}\cdot(ux)\,dS = \frac{\int_{S_b} \vec{n}\cdot(ux)\,dS\Big|_{t_2} - \int_{S_b} \vec{n}\cdot(ux)\,dS\Big|_{t_1}}{\Delta t} \tag{12.4}$$

Figures 12.4 and 12.5 show the contribution of the body acceleration term to lift and drag, which is negligable in the analysis of the force vector.

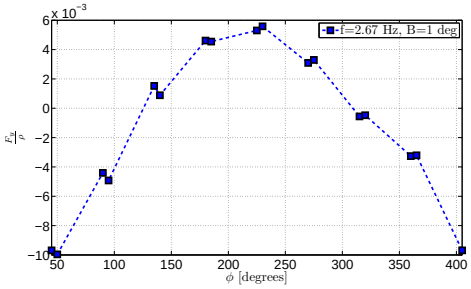

Figure 12.4: The body acceleration lift component on basis of Equation 12.2

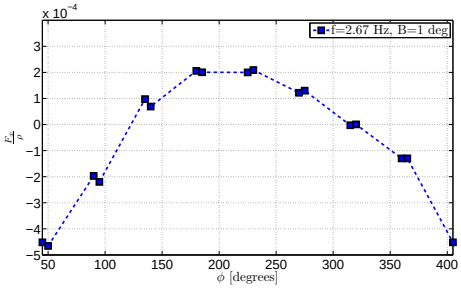

Figure 12.5: The body acceleration drag component on basis of Equation 12.2

12.3.2 Momentum flux term

The evaluation of the momentum flux term (γ_{flux}) is performed for all images at the different phases in the sinusoidal motion. The force results are plotted as a function of phase angle. The time dependent lift and drag force are plotted as a function of phase angle. For an indication of the encountered error in the set of fifteen contours, the reader is referred to Section 12.5.

In Figure 12.6 the lift force for the different unsteady cases is shown in which a clear difference in the force exist between the different cases. Case 2 ($k = 0.1, \beta = 3 \pm 3$) shows the most extreme lift values for all cases at $\phi = 90\,\text{deg}$ (minimum) and $\phi = 270\,\text{deg}$ (maximum). Case 3 ($k = 0.2, \beta = 1 \pm 1°$) shows a relatively small excursion in the lift of only ΔC_L=0.05, which matches the value $\frac{dC_l}{d\beta}$=0.05 for the steady case. Case 4 ($k = 0.2, \beta = 3 \pm 3$) shows smaller extreme values than case 2 ($k = 0.1, \beta = 3 \pm 3$), although the same flap amplitude is used. An analysis of the unsteady behaviour in terms of force amplitude reduction and phase shift as a function of the unsteadiness level k is found in Section 12.4.

The drag as plotted in Figure 12.7 is more influenced by the numerical postprocessing errors than the lift, because of the smaller force scale. However, case 3 ($k = 0.2, \beta = 1 \pm 1°$) that is expected to have the lowest drag, also complies with this fact. Case 2 ($k = 0.1, \beta = 3 \pm 3°$) and case 4 ($k = 0.2, \beta = 3 \pm 3°$) show the same trend and values

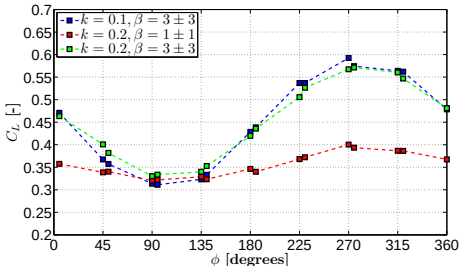

Figure 12.6: The lift force as a function of phase angle for the different cases; case 2 ($k = 0.1, \beta = 3 \pm 3$), case 3 ($k = 0.2, \beta = 1 \pm 1°$),case 4 ($k = 0.2, \beta = 3 \pm 3$)

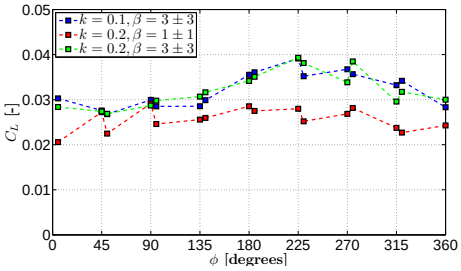

Figure 12.7: The drag force as a function of phase angle for the different cases; case 2 ($k = 0.1, \beta = 3 \pm 3$), case 3 ($k = 0.2, \beta = 1 \pm 1°$),case 4 ($k = 0.2, \beta = 3 \pm 3$)

in drag. The differences between these two cases are so small that, the effect cannot be accounted to the difference in unsteadiness, because of the high uncertainty level in the drag prediction.

12.3.3 Calculation of lift on basis of circulation

The force can also be determined by the circulation as performed in Section 9.8. The largest contour possible is considered such that it encloses the body and a large part of the wake. Figure 12.8 shows the steady lift coefficient for the circulation approach and the momentum flux approach as a function of β. For the circulation only one contour is considered, for which the steady force follows the linear trend better than the momentum flux approach (Figure 12.9).

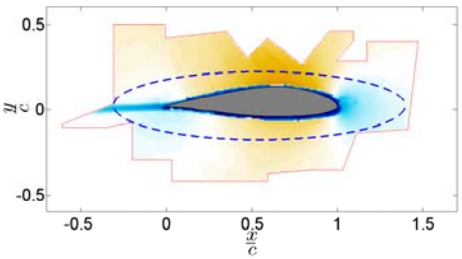

Figure 12.8: The contour over which the lift coefficient is calculated through the concept of circulation

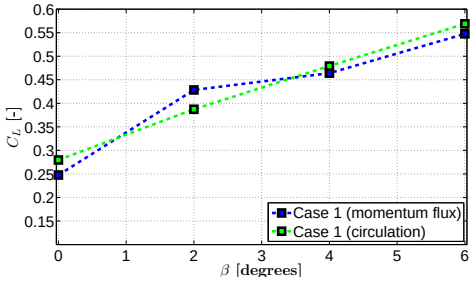

Figure 12.9: The force determined by application of the concept of circulation in steady conditions

The unsteady force is also calculated using the concept of circulation. The circulation approach is independent of time resolution, and hence no discretization errors of this type are introduced. The same contour as in the steady case is used yielding the results depicted in Figure 12.10. Differences between the two approaches are minor. The largest error occurs at the maximum flap velocity at ϕ=0deg and ϕ=180deg, indicating that the time resolution is too coarse.

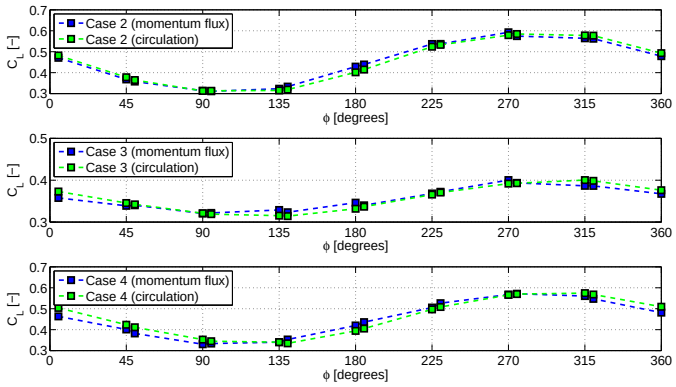

Figure 12.10: The unsteady force determined by application of the concept of circulation for the three unsteady cases

12.4 Unsteady and steady counterpart result

This section is devoted to find the effect in force amplitude and phase shift as a function of unsteadiness level k. In order to do so, use is made of the steady and unsteady lift as calculated in Section 12.2 and 12.3. Firstly, the flap angles β are calculated on the phase angles used in the determination of the unsteady force results. Secondly, a linear interpolation to these flap angles of the steady results is performed. In this case a sinusoidal motion is obtained, which is referred as *the steady counterpart*. Both the steady counterpart and the unsteady results form a sinusoidal motion. The results are plotted in Figure 12.11 and 12.12. From the plots a difference in equilibrium position, amplitude and phase is detected for both lift and drag. By comparing the unsteady force result and the steady counterpart a similar trend is detected for all unsteady cases. It shows that the unsteady force results incorporate a delay in reaching respectively their minimum and maximum value. The results for drag show that the unsteady drag can be double, compared to the steady counter part, however the accuracy level of this force is low.

In order to quantify the differences between the unsteady and steady counterpart of the lift (drag is not considered due to the large uncertainty), a least square curve fitting is applied in the three unsteady cases. In this analysis use is made of a sine reference function as represented in Equation 12.5, where A denotes the equilibrium position, B the amplitude, Φ the measured phase and ϕ the phase difference with respect to 0 phase.

$$C_L = A + B\sin(\Phi + \phi) \tag{12.5}$$

In Figure 12.13 a fitting curve for the unsteady lift according to Equation 12.5 is applied. The least square curve fitting shows a perfect match with the acquired force data. The same curve fitting is applied to the steady counter part of case 2, 3 and 4, where $\Delta\phi \simeq 0$, meaning that there is no phase difference with respect to the input sinusoidal flap motion.

The variables of Equation 12.5 (equilibrium position A, amplitude B and phase difference

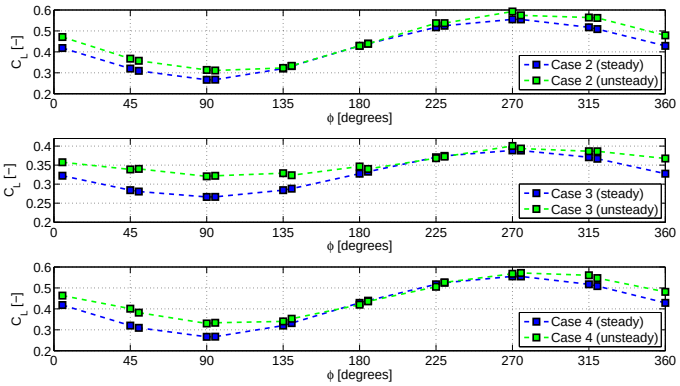

Figure 12.11: Unsteady and steady experimental lift comparison for the different test cases

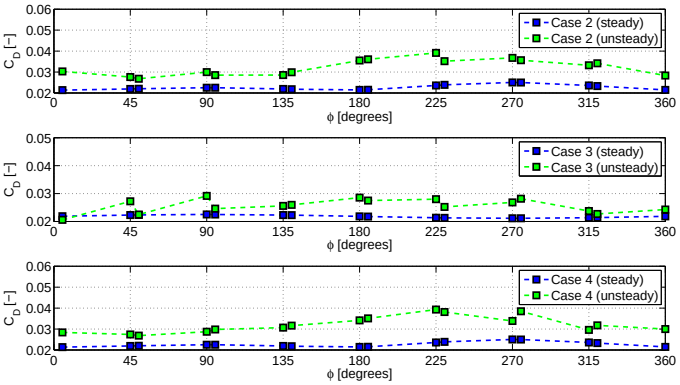

Figure 12.12: Unsteady and steady experimental drag comparison for the different test cases

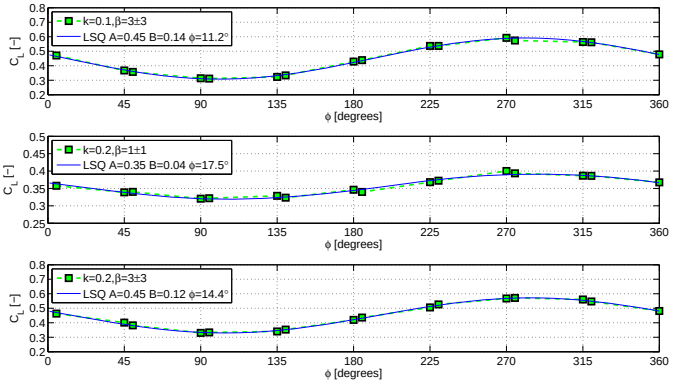

Figure 12.13: The unsteady lift coefficient with a least square sinusoidal curve fit for case 2 ($k = 0.1, \beta = 3 \pm 3°$), case 3 ($k = 0.2, \beta = 3 \pm 3°$) and case 4 ($k = 0.2, \beta = 3 \pm 3°$)

$\Delta\Phi$) are denoted in Table 12.1, where the results of the momentum flux equation are denoted in the columns M. A validation of the results is performed on basis of the unsteady force calculated by the circulation, denoted in the table in the columns C.

Parameter of $C_L = A + B\sin(\Phi + \phi)$ Method*		A $[C_L]$		B $[C_L]$		ϕ (lag) [deg]	
		M	C	M	C	M	C
Case 2 ($k = 0.1, \beta = 3 \pm 3°$)	unsteady	0.45	0.45	0.14	0.15	11.2	17.7
	steady	0.42		0.14		0.53	
	difference	0.03		0.0		10.67	
Case 3 ($k = 0.2, \beta = 1 \pm 1°$)	unsteady	0.35	0.36	0.04	0.04	17.5	31.4
	steady	0.33		0.06		0.01	
	difference	0.02		-0.02		17.4	
Case 2 ($k = 0.2, \beta = 3 \pm 3°$)	unsteady	0.45	0.46	0.12	0.12	14.4	28.0
	steady	0.42		0.14		0.53	
	difference	0.03		-0.02		13.87	

Table 12.1: The unsteady and steady counterpart equilibrium position (A), amplitude (B) and phase difference $\Delta\phi$. A quantification is given on the difference between the unsteady and steady counterpart of the sinusoidal lift force. * M is the momentum flux approach, C is the circulation approach

For both procedures (M and C), the effect of unsteadiness is clearly visible (comparing steady and unsteady force results), where a change in amplitude (B) and phase ($\Delta\phi$) is observed. As known from Theodorsen's theory (Chapter 5), the phase shift is larger when addressing a larger unsteadiness level and the amplitude of the lift reduces with larger unsteadiness levels. Focussing on Theodorsen's function with increasing k, one can see a reduction in the real part coinciding with the amplitude and an increase in the absolute value of the imaginary part, which coincides with the phase. Although Theodorsen assumes this function for pitching and plunging, the same trend is true for an unsteady flow created by an oscillated flap. If case 2 (k=0.1 $\beta = 3 \pm 3°$) and case 4 (k=0.2 $\beta = 3 \pm 3°$) are compared, it is shown that the case with k=0.1 has a smaller phase shift than the case with k=0.2. Furthermore case 2 shows a larger amplitude than case 4, which also follows from Theodorsen. The effect of flap amplitude is demonstrated by comparing case 3 (k=0.2 B=1°) and case 4 (k=0.2 B=3°). Case 3 with an amplitude of 1 deg shows a larger phase lag than case 4 in which an amplitude of 3 deg is applied. In this comparison, the equilibrium position of the flap might also have an influence on this effect.

Allthough the trend of the two approaches (momentum flux equation and circulation) is the same, a large difference exists in the phase lag observed. In the approach with circulation there is no determination of a time dependent term, involving a finite time resolution. This states that the circulation approach incorporates less numerical errors than the momentum flux equation and serves as a validator tool. However, this method does not provide any insight in the aerodynamic mechanisms driven by momentum, vorticity, acceleration and viscosity, which is the case when applying the momentum flux equation. In the next section an analysis is performed on the inviscid term and the time dependent term of the momentum flux equation.

12.5 Error analysis on the experimental force determination procedure

This section describes the errors which are encountered during the force determination procedure. It describes the error that is due to the processing of the PIV data, where three methodolgies are presented that can determine the force. For the unsteady cases the difference of the three methods is presented in terms of force fluctuations measured in the set of fifteen contours. The previous chapter shows the results of the best performing method. In order to understand the quality of the force data, one has to zoom in on the specific terms of the momentum flux equation, for which an analysis is performed.

12.5.1 Three momentum flux force determination methods

Different force determination methods are presented in this research, for which clear differences are observed. The three methods which are evaluated, are denoted in Table 12.2. All use the minimum intensity subtraction pre-processing technique for the Field of View (FOV) of the leading edge (see Chapter 11). The correlation method is fixed, which is sequential cross correlation with an interrogation window size of 32x32 pixels using an overlap of 50 %. The maximum resolution that can be obtained is 3.5 mm x 3.5 mm and is therefore applied for all methods. From the experiment a phase locked average is used on basis of hundred observations. In order not to degradate the determination of the velocity derivatives, it is decided to use the 'nearest neighbour' interpolation, leaving the velocity field for each FOV in the original shape as obtained from the PIV images. By doing so, a misalignment error can be introduced, which is treated in Section 9.6. The differences of the three methods are explained in the following paragraphs.

	RDFD method	iFFFD method	FIFD method
Pre processing techniques	minimum intensity subtraction FOV_{LE}	minimum intensity subtraction FOV_{LE}	minimum intensity subtraction FOV_{LE}
Correlation method	Sequential cross correlation (32x32 50% overlap)	Sequential cross correlation (32x32 50% overlap)	Sequential cross correlation (32x32 50% overlap)
General grid size	3.5 mm x 3.5 mm	3.5 mm x 3.5 mm	3.5 mm x 3.5 mm
Nr of samples averaged	100	100	100
Interpolation to general grid	'nearest neighbour'	'nearest neighbour'	'nearest neighbour'
Interpolation	none	Indicated regions for vorticity and acceleration	none
Filter	none	none	none
Force interpolation	no	no	yes

Table 12.2: The specification on the Raw Data Force Determination (RDFD), interpolated Flow Field Force Determination (iFFFD) and the Force Interpolation Force Determination (FIFD)

The Raw Data Force Determination method The Raw Data Force determination only uses the raw data as directly obtained from the stitching process. This means that the velocity vector field is not postprocessed with interpolation techniques to substitute likely erroneous data, which is the case for the two other methods presented.

The interpolated Flow Field Force Determination method This method uses the concept of substituting likely erroneous data in the velocityfield, the vorticity field and

the acceleration field. Figure 12.14 shows an original vorticity field without interpolation. In the same figure areas are indicated on which the interpolation should take place. The result of the interpolation process is found in Figure 12.15. The same regions as indicated in Figure 12.14 are used for the interpolation of the velocity and acceleration field. There is no filter applied for reducing noise in the velocity fields. The interpolated velocity data set is evaluated with the set of fifteen contours.

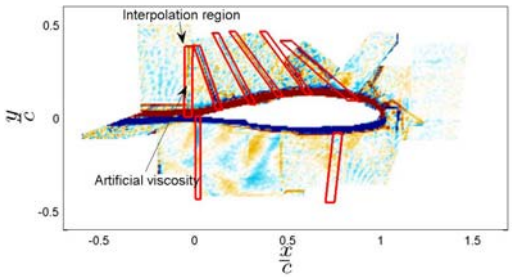

Figure 12.14: The actual vorticity field with the red regions indicating the interpolation areas

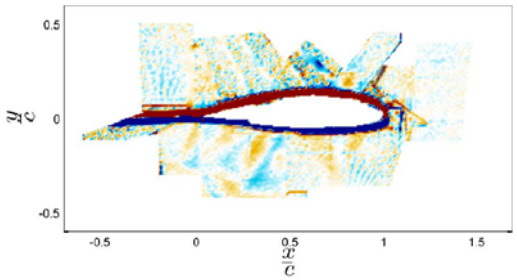

Figure 12.15: The postprocessed vorticity field

The Force Interpolation Force Determination method The Force Interpolation Force Determination method lacks the interpolation on the velocity, the acceleration and the vorticity, but uses the contour to interpolate the likely erroneous force data. In this way the total force is interpolated instead of the contributions to the force. Another difference compared to the iFFFD method is the fact that this interpolation is 1 dimensional, whereas the interpolation illustrated in Figure 11.15 uses the information from 2 dimensions. In Figure 12.16 the principle of the 1D interpolation is demonstrated.

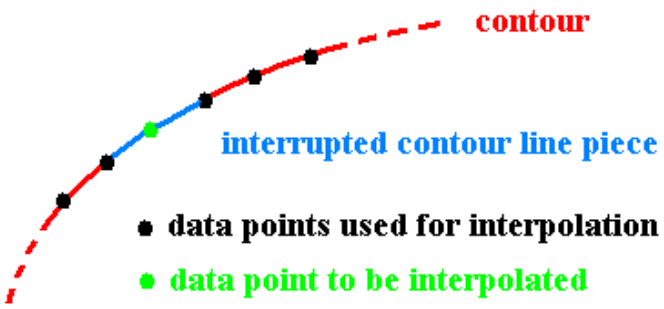

Figure 12.16: 1D force interpolation principle

A spline interpolation cannot be used since it uses a tangent boundary condition, leading to erroneous results. In this case data is used from existing data points on the same line to interpolate the gap, using a wheighted average according to Equation 12.6, the integration contour is interpolated, where V_{interp} is the variable on a point on the contour that needs to be interpolated, N is the number of points on the contour used for the interpolation and w is the weighting factor.

$$V_{interp} = \frac{\sum_{i=1}^{N} u_i \cdot w_i}{\sum_{i=1}^{N} w_i} \tag{12.6}$$

The weighting factor w is defined as $(\frac{1}{R_i})$, which ensures that the nearest points count more than points far away from the node to be interpolated.

12.5.2 The fluctuations measured in three force determination methods

The three methods are evaluated in terms of fluctuations measured within the set of fifteen contours. By doing so the precision of the three methods is determined, yielding the best method for determining the force on basis of the experimental data acquired. The relative error is determined on basis of the fluctuations found in the evaluation of the force over fifteen contours and is denoted in Equation 12.7, where C_{eq} is the equilibrium lift or drag coefficient and ϵ_{abs} is the largest deviation compared to the weighted mean of the set.

$$\epsilon_{rel} = \frac{\epsilon_{abs}}{C_{eq}} \tag{12.7}$$

Figures 12.17 to 12.22 show the results found for both lift and drag in the set of fifteen contours for the three force determination methods for case 4 ($k = 0.2$ and $\beta = 3\,\text{deg}$). The plots include gray uncertainty regions, which are the result of the process in which every contour has a deviation from the wheighted mean. In this case the weight of each separate contribution is based on the amount of bad spots encountered in the contour. A bad spot is referred to be a vector, which likely has a low peak ratio in the images/observation of the PIV measurements. If the force determination method shows almost no fluctuation in the set of contours, the solution has most likely minor influences of the finite grid resolution and the error associated with the PIV postprocessing. However, it still not guarantees the correctness of the acquired force vector, because of the systematic errors which can exist as described in 7. In general, the variation of the force is indicative how well the experiment and postprocessing is performed.

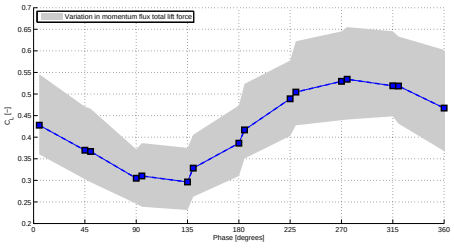

Figure 12.17: Lift force with error indication on basis of multiple contours for the RDFD method

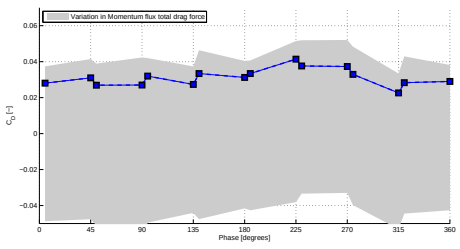

Figure 12.18: Drag force with error indication on basis of multiple contours for the RDFD method

The RDFD method shows the result without postprocessing of the vector fields. The relative error on lift in Figure 12.17 is $\epsilon_{rel} = 0.27$. For drag the relative error is far beyond 1 and hence no conclusions can be drawn about the trend.

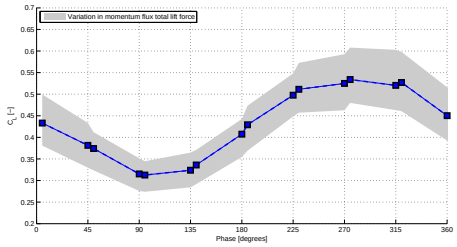

Figure 12.19: Lift force with error indication on basis of multiple contours for iFFFD method

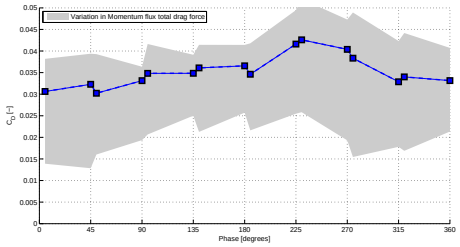

Figure 12.20: Drag force with error indication on basis of multiple contours for iFFFD method

From Figure 12.19 the maximum relative error for the lift for the iFFFD method is $\epsilon_{rel} = 0.22$. For drag the largest relative error is 1. Knowing this, drag cannot be considered as a proper result, since the error is of the same magnitude or larger as the quantity itself. Lift shows also quite a large relative error, but the trend of the solution can still be deduced.

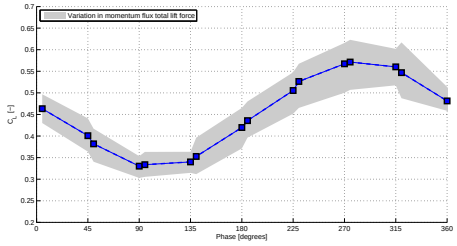

Figure 12.21: Lift force with error indication on basis of multiple contours for FIFD method

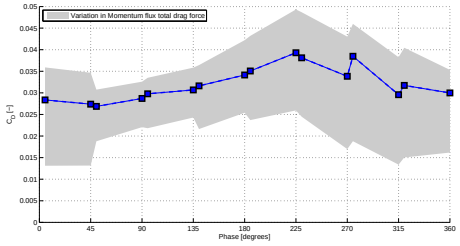

Figure 12.22: Drag force with error indication on basis of multiple contours for FIFD method

For the FIFD method a relative error for lift for case 4 ($k = 0.2$ and $\beta = 3 \pm 3°$) is $\epsilon_{rel} = 0.13$. For drag a relative error beyond 1 is observed.

In Table 12.3 the performance expressed in the relative error on basis of the evaluation of 15 predefined contours of all the methods are denoted for case 2 ($k = 0.1$ and $\beta = 3 \pm 3°$), case 3 ($k = 0.2$ and $\beta = 1 \pm 1°$) and case 4 ($k = 0.2$ and $\beta = 3 \pm 3°$). On basis of the results presented in this table, it can be concluded that the RDFD method without interpolation, shows large relative errors. The iFFFD method, which uses the information from 2 dimensions shows an improvement compared to RDFD. In this case the error region, reduces considerably, now it uses the information (velocity, vorticity and acceleration) from neighbouring points to substitute likely erroneous data. However, the FIFD method seems to improve the result even more, when an interpolation is considered on the contour itself, although the difference with the previous method is not very significant for all cases. However, this FIFD method is still preferred since the calculation cost

is less, due to the confined calculations on the contour rather than the interpolation over the entire specified regions.

		RDFD method	iFFFD method	FIFD method
Case 2	ϵ_{lift}	0.27	0.17	0.13
	ϵ_{drag}	2.50	0.71	0.67
Case 3	ϵ_{lift}	0.14	0.14	0.14
	ϵ_{drag}	1.20	1.20	0.80
Case 4	ϵ_{lift}	0.27	0.22	0.13
	ϵ_{drag}	> 2.70	0.69	0.62

Table 12.3: The maximum relative error in cases 2,3 and 4 for three force determination methods

12.5.3 Momentum flux constituents

The momentum term γ_{flux} consists of mutliple constituents as described in Table 9.1. Each constituent has a characteristic error. The position of the contour and the time instant when the flow is captured determine the composition of the total force as a function of the separate contributions. A demonstration is given on a contour showing the different contributions per test case.

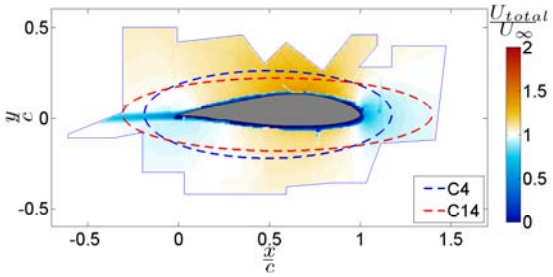

Figure 12.23: Velocity field of case 4 (k=0.2, β=3±3°) at 5 degrees of phase with 2 separate integration contours; C4 and C14

In Figure 14.10 two contours are plotted. The evaluation of the separate components is performed on contour C4, where Figure 12.24 shows the momentum term, Figure 12.25 shows the vorticity term and Figure 12.26 shows the time dependent term.

The momentum term and the time dependent term show similar trends for all cases. However, the vorticity shows large fluctuations in all cases. Each separate term contributing to the force has its own error. As shown earlier the noise contributing to an error has more influence on the inviscid term than on the time dependent term (see Section 9.3). As demonstrated the different contributions to the force are governed by the contour position and the time instance. Comparing the vorticity term for a contour close to the airfoil (C4) and relatively far away (C14) shows the influence of position on the force contribution (Figure 12.27). The fluctuations in the vorticity term on C4 is much larger than on C14. This can be caused by the fact that the vorticity is not well captured in regions close the airfoil as demonstrated in Chapter 9.

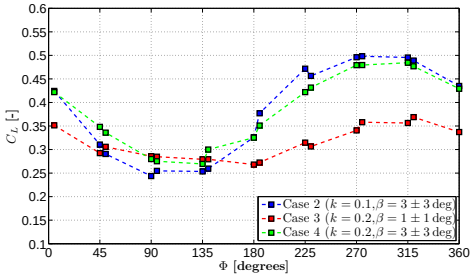

Figure 12.24: The momentum term for the three unsteady test cases for contour 4

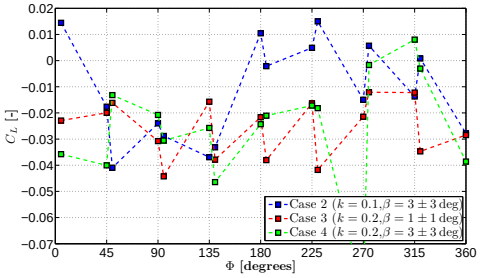

Figure 12.25: The vorticity term for the three unsteady test cases for contour 4

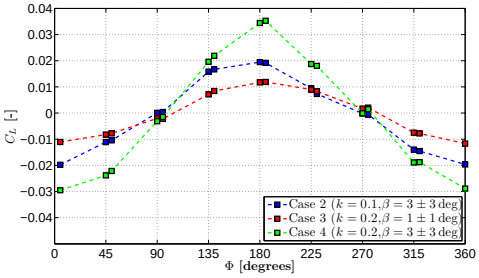

Figure 12.26: The time dependent term for the three unsteady test cases for contour 4

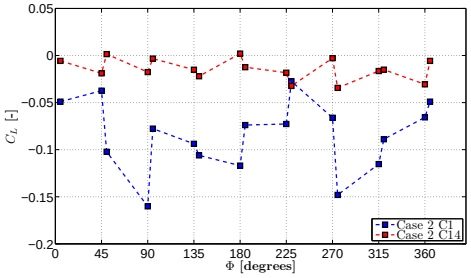

Figure 12.27: The vorticity term compared for the contour C4 and C14

Part III

Computational Fluid Dynamics

Chapter 13

Panel method simulation and the determination of flow features

This chapter describes how the theory outlined in Chapter 6 is used to simulate the aerodyanmics of a DU96W180 airfoil with oscillated airfoil for the testcases defined in the experiment; case 1 ($k = 0$ and $\beta = 0, 2, 4, 6$), case 2 ($k = 0.1$ and $\beta = 3 \pm 3\,\text{deg}$), case 3 ($k = 0.2$ and $\beta = 1 \pm 1\,\text{deg}$) and case 4 ($k = 0.2$ and $\beta = 3 \pm 3\,\text{deg}$).

The panel method is validated with Theodorsen's theory in Appendix C. In Section 13.1 a description is given on the setup of the panel code simulation. It gives an overview how the panels are defined in correspondence with the deforming geometry. Furthermore insight is provided for the determination of the force on basis of the distribution of flow elements on the panels. Also the technique to determine the velocity fields on basis of the distribution of flow elements is shortly addressed. Section 13.2 is devoted to a convergence study of the simulations performed. Finally, in Section 13.3 some velocity fields and its derivatives are plotted and discussed.

13.1 Panel method simulation

In order to create a similar situation as in the experiment, the same conditions are applied to the simualtion model; a freestream velocity U_∞=21 m/s, the chord $c = 0.5$ on which the reduced frequencies $k = 0.1$ and $k = 0.2$ are based. It must be stated that the wall of the wind tunnel is not considered, yielding forces that might be lower due to the neglection of the wall. This section is devoted to the setup of the panel code simulation. The section adresses the geometry definition and source-doublet-vortex distribution, the panel code force determination and the determination of the velocity vectors.

13.1.1 Geometry definition and source-doublet-vortex distribution

The geometry of the airfoil is defined by the original coordinates of the DU96W180 airfoil. The distribution of the sources, doublets and vortices is depicted in Figure 13.1.

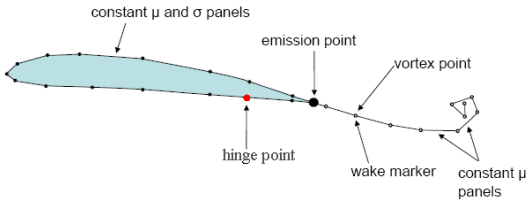

Figure 13.1: The distribution of sources, doublets and vortices over the body and wake surface Dixon [2008]

From the figure it becomes clear that the source-doublet elements are used for creating a thick airoil, with σ and μ respectively the strength of the source and the doublet. The emission point is the point where the vortices are shed as discussed in Chapter 6. The near wake is represented by constant doublet panels and the far wake is modelled by vortex elements. The hinge point is defined on the lower side of the airfoil, which is also the case on the airfoil model. The deformation of the body is performed as a function of time where use is made of the relation denoted in Equation 13.1, where f is the frequency in Hertz, t the time in seconds and h_f is the amplitude of the motion.

$$\beta = -h_f + h_f \sin(2\pi f t) \tag{13.1}$$

The flap angle β from this relation is then used in Equation 13.2 to deform the body.

$$\begin{bmatrix} X_r \\ Y_r \end{bmatrix} = \begin{bmatrix} \cos(\beta) & -\sin(\beta) \\ \sin(\beta) & \cos(\beta) \end{bmatrix} \begin{bmatrix} X \\ Y \end{bmatrix} \tag{13.2}$$

13.1.2 Force determination

The panel code used is on basis of the theory presented in Chapter 6. The forces acting on the body are calculated through Equations 13.3 and 13.4. These calculations serve as reference for the determination of the force vector by applying the momentum flux equation, where C_p is the unsteady pressure coefficient obtained through the unsteady Bernoulli formulation (J. Katz et al [2001]).

$$F_x = \sum_{n=1}^{N} \hat{n}_x C_p l_{panel} \tag{13.3}$$

$$F_y = \sum_{n=1}^{N} \hat{n}_y C_p l_{panel} \tag{13.4}$$

The determination of the force according to this section is referred as the direct output of the panel code.

13.1.3 The acquisition of the velocity vectors

In general the panel method calculates the strength of the doublets, sources and vortex elements on basis of the flow conditions determined by the explicit flow conditions and the geometry of the body as a function of time. The distribution and the strength of the singularities over the body influence every single grid point in the domain. In this way an entire velocity field can be build up by adding the individual contributions to the velocity for every singularity according to Equation 13.5 and 13.7, where the wake and the body are treated separately, N is the number of the specific singularity elements and (x_i,y_i) are the points where the velocity is calculated.

$$U_{Xi_{wake}}(x_i, y_i) = \sum_{i=1}^{N} U_{vor} \tag{13.5}$$

$$V_{Yi_{wake}}(x_i, y_i) = \sum_{i=1}^{N} V_{vor} \tag{13.6}$$

$$U_{Xi_{body}}(x_i, y_i) = \sum_{i=1}^{N} U_{src} + U_{dbl} \tag{13.7}$$

$$V_{Yi_{body}}(x_i, y_i) = \sum_{i=1}^{N} V_{src} + V_{dbl} \tag{13.8}$$

By specifying (x_i,y_i) a grid can be introduced on which the velocity vectors can be determined. The result of this process is the velocity field around the body at every time step for a specified grid. For determination of the force the momentum flux equation is used on basis of the procedure as found in the experimental case.

13.2 Convergence study

For the steady cases and the unsteady cases denoted in Table 10.1 a convergence study is performed. Multiple phases of the flap motion are followed and when a constant behaviour is detected the solution is converged. Also the time resolution is tested, since this parameter has an influence on the size of the wake panels and hence the results obtained.

The Figures show that all the results converge and that the time refinement of $\phi_t = 5°$ to $\phi_t = 1°$ does not influence the results. Therefore it is decided to use the low time resolution of $\phi_t = 5°$ in order to save computational time.

13.3 Visualisation of flow quantities

This section illustrates the different flowfeatures (total velocity, vorticity and acceleration) that are encountered in simulated case 4 ($k = 0.2$, $\beta = 3 \pm 3°$). Figures 13.6 to 13.14 illustrate the features at $\phi = 90°$, $180°$, $270°$, $360°$.

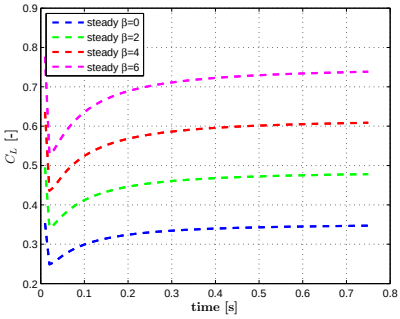

Figure 13.2: The convergence study of the panel code of the steady results for β=0,2,4,6

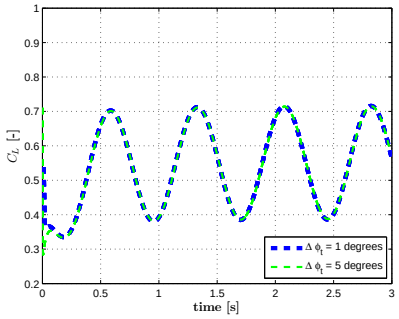

Figure 13.3: The convergence study of the panel code for the unsteady results for $\beta = 3 \pm 3$ and k=0.1

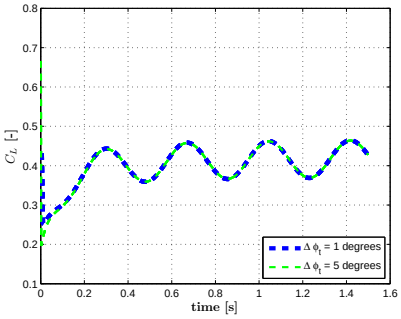

Figure 13.4: The convergence study of the panel code for the unsteady results for $\beta = 1 \pm 1$ and k=0.2

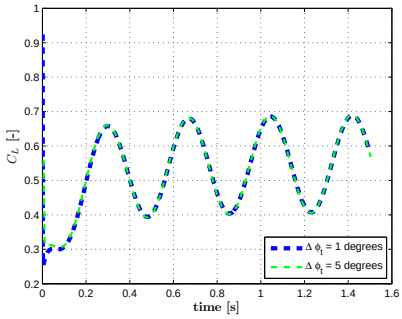

Figure 13.5: The convergence study of the panel code for the unsteady results for $\beta = 3 \pm 3$ and k=0.2

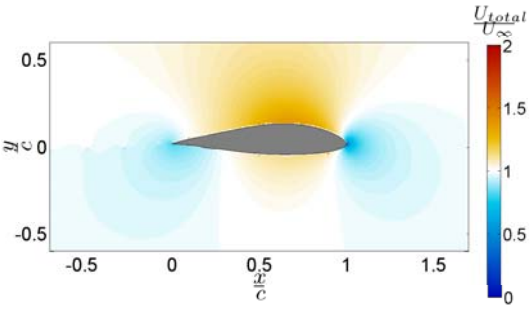

Figure 13.6: ($k = 0.2$, $\beta = 3 \pm 3°$, $\phi = 90°$)

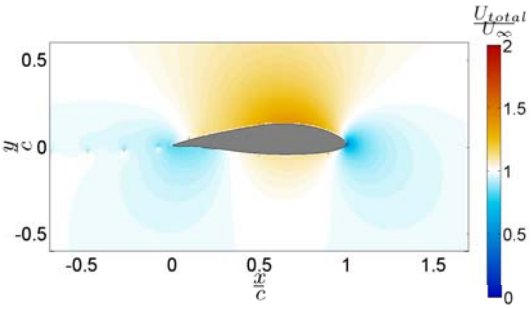

Figure 13.7: ($k = 0.2$, $\beta = 3 \pm 3°$, $\phi = 180°$)

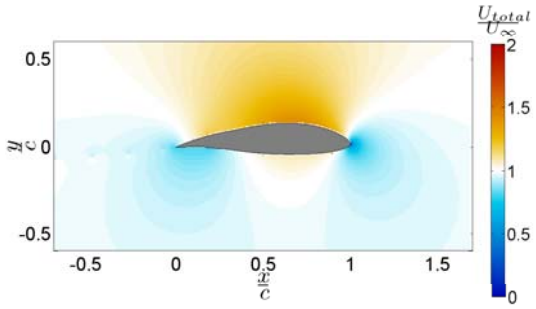

Figure 13.8: ($k = 0.2$, $\beta = 3 \pm 3°$, $\phi = 270°$)

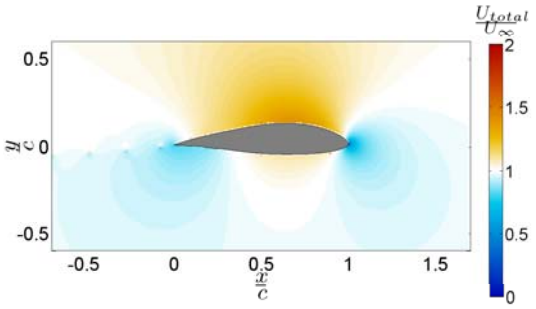

Figure 13.9: ($k = 0.2$, $\beta = 3 \pm 3°$, $\phi = 360°$)

Figures 13.6 to 13.6 show the total velocity fields at the maximum and minimum position of the flap and the two equilibrium position. It shows (see Appendix B) that the low velocity regions at the leading edge and the trailing edge move up and down as a function of flap angle β.

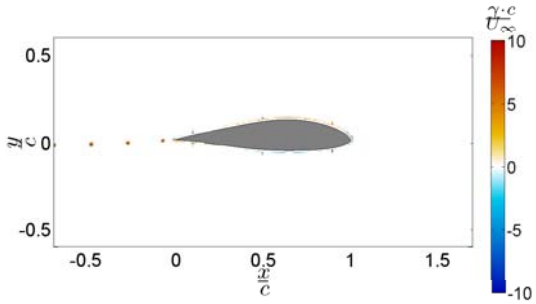

Figure 13.10: ($k = 0.2$, $\beta = 3 \pm 3°$, $\phi = 90°$)

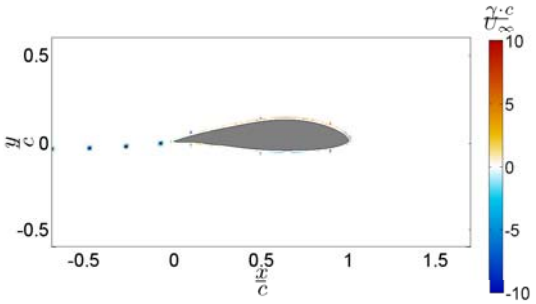

Figure 13.11: ($k = 0.2$, $\beta = 3 \pm 3°$, $\phi = 180°$)

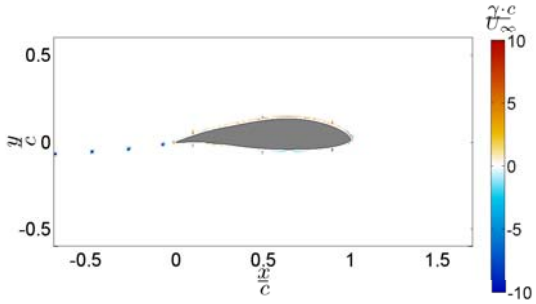

Figure 13.12: ($k = 0.2$, $\beta = 3 \pm 3°$, $\phi = 270°$)

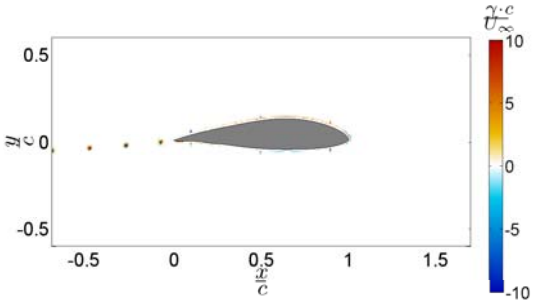

Figure 13.13: ($k = 0.2$, $\beta = 3 \pm 3°$, $\phi = 360°$)

As discussed in Chapter 6 the panel method expells vortices when a change of the bound circulation is felt. From Figures 13.10 to 13.13, these vortices are clearly visible. As a function of phase ϕ the strength of the vortices change. A counterclockwise motion of the flap, results in negative (clockwise) vorticity. A clockwise motion of the flap, implies positive (counter clockwise) vorticity.

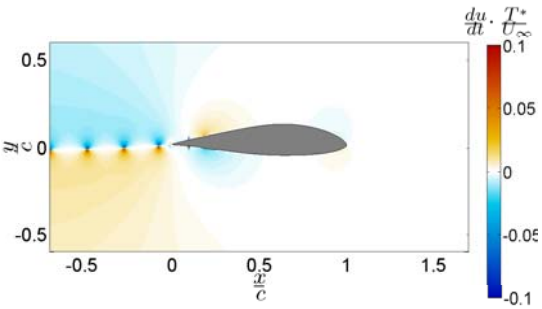

Figure 13.14: ($k = 0.2$, $\beta = 3 \pm 3°$, $\phi = 90°$)

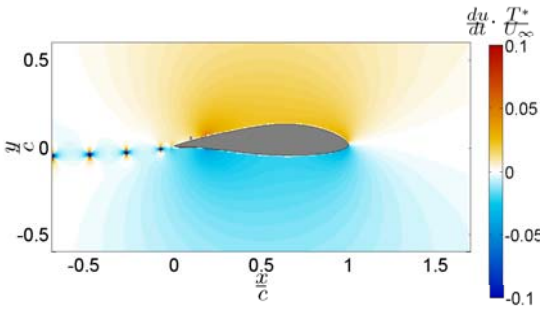

Figure 13.15: ($k = 0.2$, $\beta = 3 \pm 3°$, $\phi = 180°$)

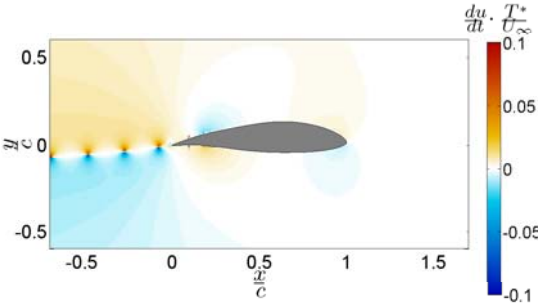

Figure 13.16: ($k = 0.2$, $\beta = 3 \pm 3°$, $\phi = 270°$)

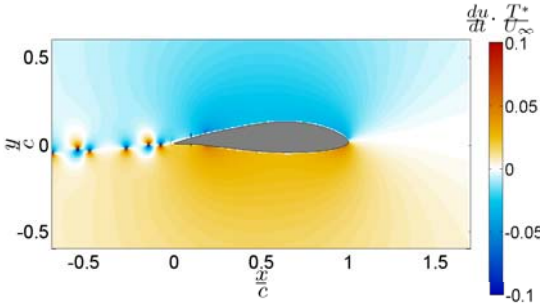

Figure 13.17: ($k = 0.2$, $\beta = 3 \pm 3°$, $\phi = 360°$)

The wake shows the highest temporal change in the velocity as illustrated in Figures 13.14 to 13.17, visible by the vortex singularities that convect down stream. In the extreme flap up and flap down position ($\phi = 90$ and $\phi = 270$) the acceleration of the flow is small compared to the positions in which the flap crosses the equilibrium position ($\phi = 180$ and $\phi = 360$). Similar behaviour is also detected in the experimental results as depicted in Section 11.5.

Chapter 14

The panel code force results

This chapter describes the determination of the force for the panel method. The determination is based on the momentum flux approach in reference with Chapter 9 and according to the theory described in Section 13.1.2, where the force is determined on basis of the pressure. This reference force is used to evaluate the performance of the momentum flux approach. In order to verify the performance of the momentum flux approach, different testcases are set up. From this information, it can for example be deduced if the experimental results would improve by application of a finer time and space resolution.

Section 14.1 describes the setup for the determination of the force by application of the momentum flux equation. Section 14.2 reveals the steady results of the panel method. In Section 14.3 the unsteady results are addressed, where in Section 14.4 the influence of the unsteadiness of the flow is described. It shows the result for the momentum flux approach and the panel code direct force output. This comparison reveals the limitation of the momentum flux approach as addressed in Section 14.1. Section 14.5 is devoted to the setup of different momentum flux force determination procedures in order to identify the influence of spatial resolution, temporal resolution and noise. Finally, in Section 14.5.2 the separate flux contributions to the total lift force are examined.

14.1 General considerations on the momentum flux force evaluation

In order to compare the panel code and the experimental results in Chapter 15 the same set of contours as illustrated in Figure 12.1 is used, in order to guarantee that similar numerical errors are introduced due to the spatial resolution of the grid (3.5 mm x 3.5 mm) at similar positions. Thereby also the time interval for the determination of the acceleration of the flow of the panel method is set equal to the time interval in the experiment, which is $\phi_t = 45\,\mathrm{deg}$ corresponding to t=0.05 and t=0.1 respectively for the

reduced frequencies of $k = 0.2$ and $k = 0.1$. Velocity fields are determined on the same phase angles as the experiment (ϕ=0, 5, 45, 50...) and in this way the same set of flow and force data is obtained with the same spatial and temporal resolution obtained from the same regions in the flow domain. In this chapter only lift is considered, due to the fact that potential flow of the panel code cannot determine drag.

14.2 Force evaluation in steady conditions

Figure 14.1 shows the lift coefficient as a function of flap angle β for the panel code in which the result of the panel code direct force output (see Section 13.1.2) and the momentum flux equation on basis of fifteen contours as presented in previous chapters, are considered. The lift increases linearly with increasing flap angle β. The figure shows no deviation between the two force determination methods.

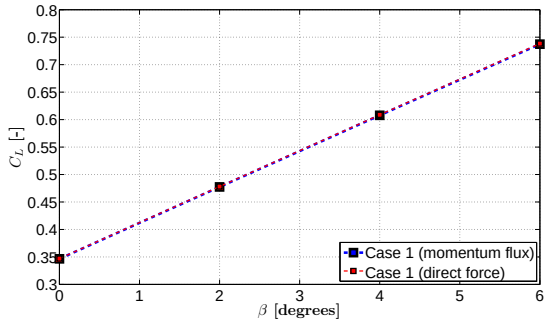

Figure 14.1: Comparison of the steady lift force determined by the momentum flux equation and direct force output by pressure integration

14.3 Force evaluation in unsteady conditions

Figure 14.2 shows the lift coefficient for the three different cases determined by the momentum flux equation over the velocity fields generated by the panel code. The lift coefficient clearly has an equilibirum position according to the mean flap angle. This coefficient is in correspondence with the interpolated steady result at β=1 and 3. Comparing case 2 ($k = 0.1$ and $\beta = 3 \pm 3°$) and case 4 ($k = 0.2$ and $\beta = 3 \pm 3\,\text{deg}$) shows an unsteady effect (due to a different unsteadiness level k) expressed in phase difference and amplitude. In Section 14.4 the influence of the unsteadiness k is quantified for the results presented in this section.

The results on basis of the determination of the force by the momentum flux equation, is depicted in Figure 14.2. The difference between the lift force for both methods (momentum flux and pressure integration) is illustrated in Figure 14.3. A phase shift is detected between the momentum flux result and the original force output. This difference is caused by the definition of the time term. The analysis on this type of error is found in Section 14.5.

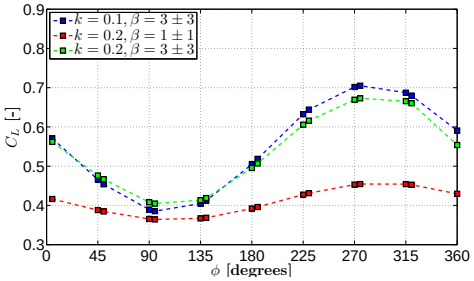

Figure 14.2: Comparison of the lift force for the different cases determined by the momentum flux equation

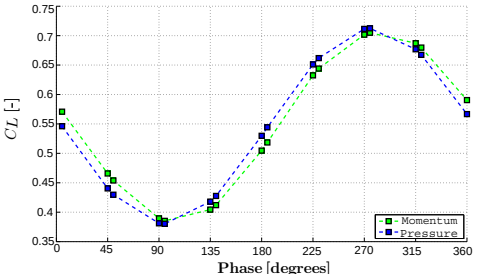

Figure 14.3: The lift coefficient determined by the the momentum flux equation and the panel code pressure integration for case 2 ($k = 0.1$ and $\beta = 3 \pm 3\,\mathrm{deg}$)

14.4 Unsteady and steady counterpart result

This section is devoted to find the effect in force amplitude and phase shift as a function of unsteadiness level k for the panel code. In order to do so, use is made of the steady and unsteady lift (direct output of panel code and momentum flux equation) as calculated in Section 14.2 and 14.3. Firstly, the flap angles β are calculated for the phase angles used in the determination of the unsteady force results. Secondly, a linear interpolation to these flap angles of the steady results is performed. In this case a sinusoidal motion is obtained, which is referred as *the steady counterpart*. Both the steady counterpart and the unsteady results form a sinusoidal motion. The results are plotted in Figure 12.11 and 12.12. From the plots a difference in equilibrium position, amplitude and phase is detected for the lift. By comparing the unsteady force momentum flux result and the steady counterpart a similar trend as in the experimental results is detected for all unsteady cases. It shows that the unsteady force results incorporate a delay in reaching respectively their minimum and maximum value.

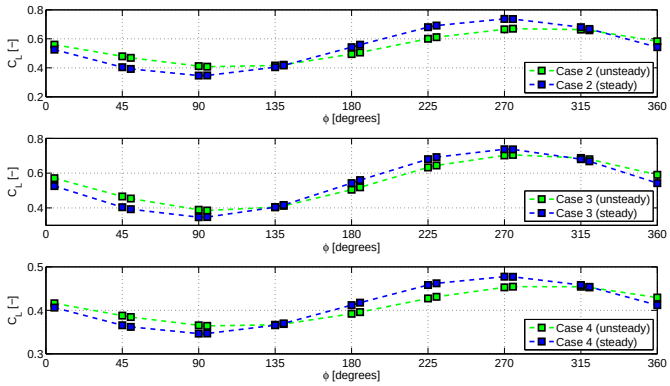

Figure 14.4: The unsteady lift and the steady counterpart of the lift produced by the panel code for unsteadiness levels $k = 0.1$ and $k = 0.2$

Again the same least square curve fitting is applied for all cases in both unsteady lift

and the steady counterpart of the lift. The same sinus reference function is used as in the experimental evaluation repeated in Equation 14.1, where A denotes the equilibrium position, B the amplitude, Φ the measured phase and $\Delta\phi$ the phase difference with respect to 0 phase.

$$C_L = A + B\sin(\Phi + \Delta\phi) \tag{14.1}$$

In Figure 14.5 the experimental unsteady results are plotted along the LSQ sine curve with the variables of Equation 14.1 denoted in the figure. Here the effect of unsteadiness is clearly visible, where a change in amplitude (B) and phase ($\Delta\phi$) is observed. Again Theodorsen's theory in phase lag and amplitude matches the results of the LSQ curve fit parameters. If case 2 and case 4 are compared it is shown that the case with k=0.1 has a smaller phase shift than the case with k=0.2. Furthermore case 2 shows a larger amplitude than case 4, which also follows from Theodorsen. The effect of flap amplitude is demonstrated by comparing case 3 and case 4. Case 3 with an amplitude of 1 deg shows a larger phase lag than case 4 in which an amplitude of 3 deg is applied.

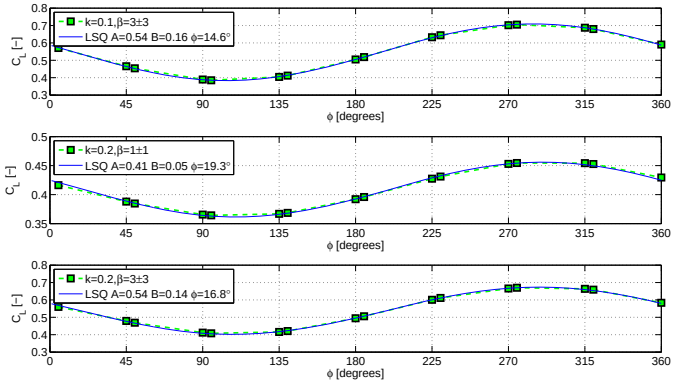

Figure 14.5: The unsteady lift and the steady counterpart of the lift produced by the panel code for unsteadiness levels $k = 0.1$ and $k = 0.2$

The variables of Equation 12.5 (equilibrium position A, amplitude B and phase difference $\Delta\Phi$) are denoted in Table 14.1, where the momentum flux result is denoted in column with captial M and the results according to the direct force output of the panel code with captial P.

The two results (M,P) presented in the table show the phase and amplitude differences determined by application of the Least Square Curve Fit for both the two force determination methods. The largest difference between the methods is found in the determination of the phase difference $\Delta\phi$. The difference in $\Delta\Phi$ between the two approaches are introduced due to the coarse timestep of $\phi_t = 45\,\text{deg}$ and the numerical errors introduced due to the spatial resolution. In Section 14.5 the influence of the spatial and temporal resolution on the force results is illustrated.

Parameter / Method*		A $[C_L]$ M	A $[C_L]$ P	B $[C_L]$ M	B $[C_L]$ P	$\Delta\phi$ [deg] M	$\Delta\phi$ [deg] P
Case 2 ($k = 0.1, \beta = 3 \pm 3$)	unsteady	0.54	0.55	0.16	0.17	14.6	5.7
	steady	0.54	0.54	0.19	0.19	0.01	0.01
	difference	0.0	0.01	0.03	0.02	14.61	5.69
Case 3 ($k = 0.2, \beta = 1 \pm 1$)	unsteady	0.41	0.41	0.05	0.05	19.3	5.8
	steady	0.41	0.41	0.07	0.07	0	0
	difference	0.0	0.0	0.02	0.02	19.3	5.8
Case 2 ($k = 0.2, \beta = 3 \pm 3$)	unsteady	0.54	0.54	0.14	0.15	16.8	6.8
	steady	0.54	0.54	0.19	0.19	0.01	0.01
	difference	0.0	0.0	0.05	0.04	16.79	6.79

Table 14.1: The unsteady and steady counterpart equilibrium position (A), amplitude (B) and phase difference $\Delta\phi$. A quantification is given on the difference between the unsteady and steady counterpart of the sinusoidal lift force. * M is the momentum flux approach, P refers to the panel code force output

14.5 Error analysis by means of the panel code force determination procedure

14.5.1 Four force determination methods

By application of the panel method the force vector acting on the body can be calculated in two ways;

- Momentum flux equation
- Direct output of the panel code

On basis of these two methods, different approaches for the force evaluation can be performed as summarized in Table 14.2.

	Method 1	Method 2	Method 3	Method 4
Force determination technique	Direct ouput of the panel code	momentum flux equation	momentum flux equation	momentum flux equation
General grid size	n/a	3.5 mm x 3.5 mm/ 1.5 mm x 1.5 mm	3.5 mm x 3.5 mm	3.5 mm x 3.5 mm
Temporal resolution	$\phi_t = 1\,\text{deg}$	$\phi_t = 5\,\text{deg}$	$\phi_t = 1\,\text{deg}$	$\phi_t = 5\,\text{deg}$
Noise	n/a	none	none	yes

Table 14.2: The different methods for determining the force acting on the body simulated by the panel code

The momentum flux equation approach is based on the velocity fields that are generated with the information of the singularity distribution of the panel code. The direct output of the panel code uses the foundation for the force determination prescribed in Chapter 6. These two outputs can be compared, yielding the estimation of the quality of the momentum flux procedure as outlined in Chapter 9.

Method 1 This method makes use of the theory described in Section 13.1.2, referred to as the direct output of the panel code. In this case grid resolution does not influence the results, since the force is calculated on basis of the distribution of flow elements on the surface of the body and wake. In this case the panelling of the body and wake can have influence on the force determined, however the panelling is assumed to be good enough to give a well converged solution. The forces are taken at every $\Delta\phi = 1\,\text{deg}$.

Method 2 This method uses the velocity data calculated at each node specified in the grid according to the resolutions stated in the table. Since the distribution of the flow elements have an implicit relation for the velocity vectors by means of the potential calculated, the velocity vector can be calculated on each node of the flow domain. So in this case the interpolation does not add unwanted errors on the velocity vectors. The temporal resolution is specified to be $\phi_t = 45\,\text{deg}$, which is also the timestep used in the experiment. The two resolutions are compared in terms of the fluctuations (error) measured over the total force as a function of contour.

Using a grid of 3.5 mm x 3.5 mm, a distribution of the error (the fluctuation over 15 contours) expressed as ΔC_L for all the phases is illustrated in Figure 14.6. For the phases $\phi = 5$ and 360, the largest error is observed, whereas the smallest errors occur at 90 and 270 degrees of phase, which is respectively the most flap up and flap down position.

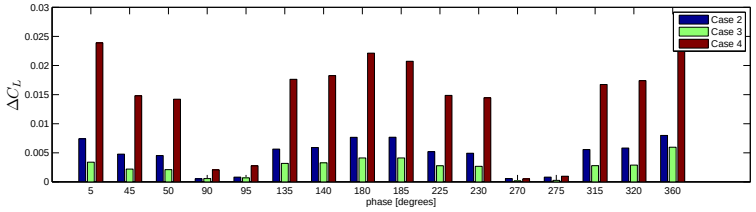

Figure 14.6: The error expressed as ΔC_L obtained over fifteen contours as a function of phase

The error (maximum difference between the panel code force and the momentum flux force) encountered within a full period of the flap is $\Delta C_L \simeq 0.02$ for case 2,$\Delta C_L \simeq 0.01$ for case 3 and ΔC_L=0.02 for case 4. This analysis shows that by taking the mean of the force of the different contours, the solution converges to the actual force observed by application of the force determination over multiple contours. In this case a grid resolution of 3.5 mm is used, which compares with the resolution of the experiment.

The forces are also calculated on a fine grid with a spacing of 1.5 mm. The errors (maximum difference between the panel code force and the momentum flux force) for both 1.5 mm and 3.5 mm spacing are denoted in Table 14.3.

From the maximum errors denoted in the table it can be concluded that grid refinement almost shows no variation in the error observed, meaning that the spatial related error is already converged at a grid size of 3.5 mm. This result states that refining the grid resolution beyond 3.5 mm does not influence the numerical determination of the force,

	$Error_{1.5mm}$	$Error_{3.5mm}$
Case 2	$\Delta C_L = 0.0165$	$\Delta C_L = 0.0167$
Case 3	$\Delta C_L = 0.0061$	$\Delta C_L = 0.0064$
Case 4	$\Delta C_L = 0.0178$	$\Delta C_L = 0.0183$

Table 14.3: The fluctuations of the momentum flux force with respect to the panel force ouput do not change significantly with increasing spatial resolution

such that a different mean lift force is calculated on basis of this specific set of contours. It states that the error incorporated in the momentum results has a different cause, which is denoted in the next method description.

Method 3 This method is a copy of method 2 except for the fact a only uses a spatial resolution of 3.5mm x 3.5 mm and the temporal resolution is specified to be $\phi_t = 1\,\text{deg}$. By using the coarse time step from method 2 and the refined time step of method 3, the influence of the resolution of the time term in the momentum flux equation is evaluated.

Since the experiment deals with unsteady flow ($\frac{d}{dt} \neq 0$) also the time resolution must be tested. Two time resolutions are tested, which are $\phi_t = 1\,\text{deg}$ and $\phi_t = 5\,\text{deg}$. For the different time resolutions, the contribution of the time term (term II in Table 9.1) is analyzed, showing the influence of time resolution on the unsteady force. Equation 14.2 is repeated, where Δt for deriving the acceleration of the flow is the variable in the definition of the time dependent term.

$$\frac{du}{dt} = \frac{\vec{u}_{t+\Delta t} - \vec{u}_t}{\Delta t} \tag{14.2}$$

Since a discrepancy exists between the momentum flux result and the panel code result it is likely that the time resolution is the cause of this difference. In Figure 14.7 an analysis is found showing the trend of the total force as a function of Δ t.

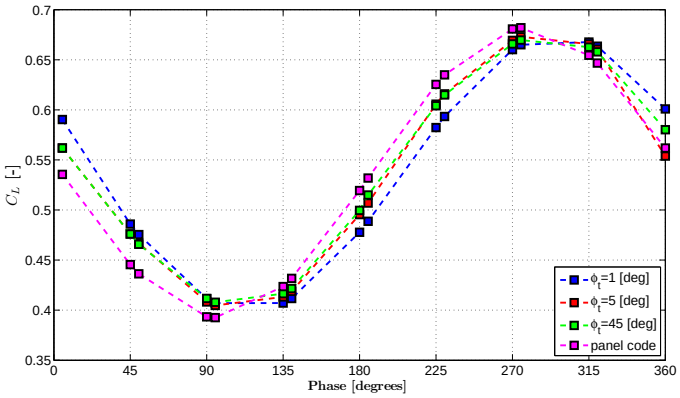

Figure 14.7: The total lift force for case 4 (k=0.2, $\beta = 3 \pm 3°$) with increasing time resolution,

The graph shows that the time term varies with changing time resolution, indicating that the unsteady phenomena cannot be captured by a coarse time resolution of 45 degrees of phase. The maximum difference for the 45 degrees resolution and the the 1 degree resolution is $\Delta C_L = 0.02$. However, comparing the result of the 1 degree time resolution and the panel code force ouput, shows that the error becomes even larger, although the result should be more accurate with a finer time resolution. So if the error in the time term is reduced and the discrepancy between the direct output of the panel code and the momentum flux result is larger for this fine time resolution, the error is caused by yet another phenomena. Viscosity is not part of the solution, so the error is determined in the establishment of the inviscid term. Thereby the error introduced due to the interpolation of velocity data to the contour and the determination of the gradient related terms, can be up to ΔC_L=0.05.

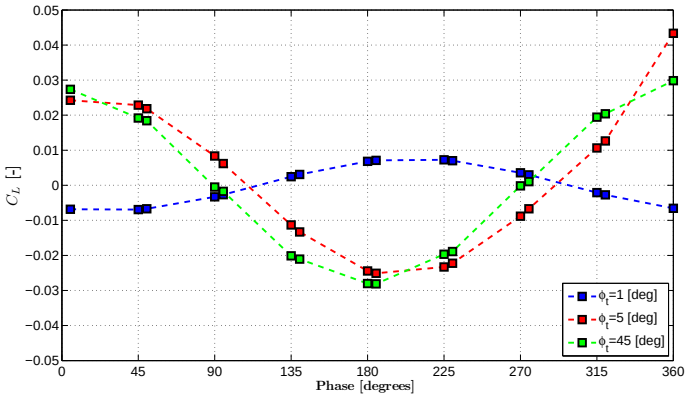

Figure 14.8: The time dependent lift force for case 4 with increasing time resolution; it shows opposite trend at fine time resolutions

The analysis on the time term shows that the usage of a coarse time resolution has a damping effect on the unsteady lift force determined. This is illustrated in Figure 14.8 where the fine time resolution shows an opposite effect on what is predicted by a coarse time resolution of $\phi_t = 5\,\text{deg}$ and $\phi_t = 45\,\text{deg}$. The largest errors are detected at ϕ = 0,180,360 deg, where around ϕ= 90 and 270 deg the error is minimal.

Method 4 This method uses a resolution of 3.5mm x 3.5mm and a time step of $\phi_t = 5\,\text{deg}$. Noise is subsequently introduced on basis of the theory described in Chapter 7 and Section 11.2.2. The influence of this noise is then used to determine the error on the momentum flux equation with an artificial PIV noise. In Chapter 15 this result is compared with the experimental result.

The method makes use of the error generated on basis of Equation 11.5, which uses the subpixel accuracy in combination with the interrogation window size to generate the error of 1.25%. Here it is assumed that the error takes the form of a Guassian distribution. Equation 7.5 describes the error when multiple observations are performed. In the experiment a phase locked average of 100 observations is performed, reducing the random error by $2\sqrt{(N)}$=20, with N=100. So the actual noise measured on the determined

velocity field is $\frac{1.25}{20}$ %. In Figure 14.9 three plots are given ranging from 0 % noise up to 1.25 % noise. The influence of the noise on the lift force is clearly visible, although the trend is still intact.

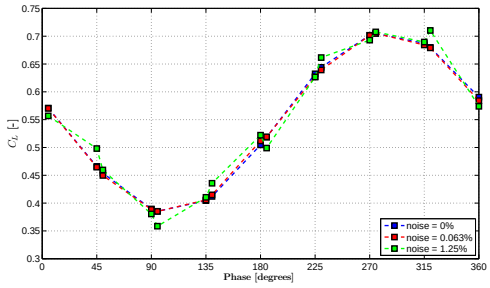

Figure 14.9: The total lift force for case 4 (k=0.2, β=3±3°) with increasing noise level

14.5.2 Momentum flux constituents

The momentum term γ_{flux} consists of mutliple constituents as described in Table 9.1. Each constituent has a characteristic error. The position of the contour and the time instant when the flow is captured determine the composition of the total force as a function of the separate contributions.

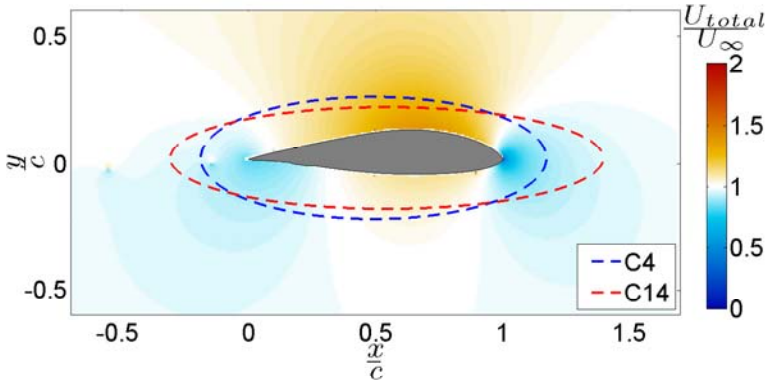

Figure 14.10: Velocity field of the panel code case 4 at 5 degrees of phase with 2 separate integration contours (C4, C14)

The contour is evaluated and the three contributions (momentum term, vorticity term and time dependent term) are shown in Figures 14.11 to 14.13. As opposed to the experimental results, the trend of the vorticity term and the momentum term are equal. The noisy character as determined in the experiment is not detected. The time dependent term shows an opposite trend for the cases associated with k=0.2 compared to the case k=0.1.

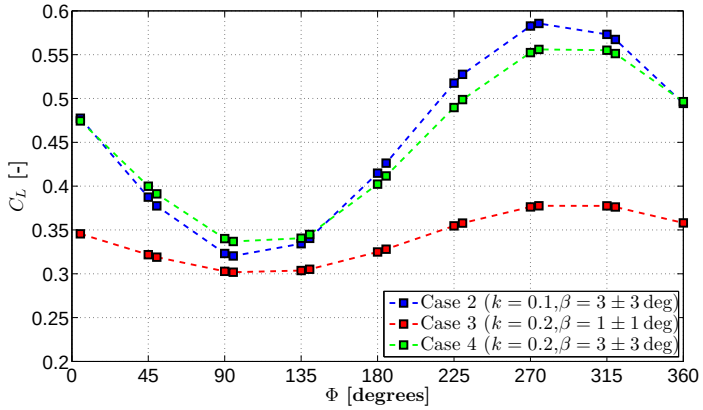

Figure 14.11: The momentum term for the three unsteady test cases for contour 4

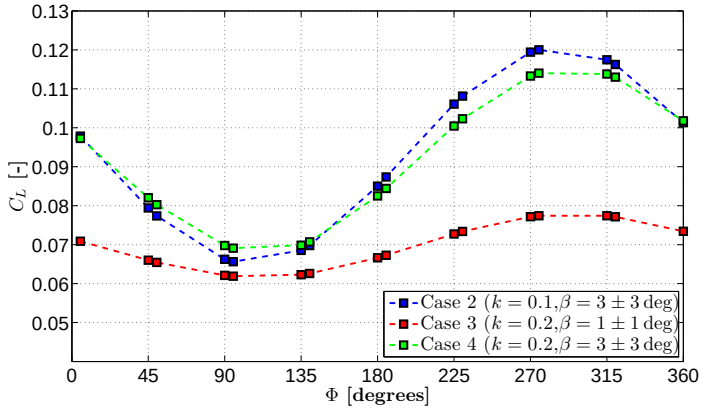

Figure 14.12: The vorticity term for the three unsteady test cases for contour 4

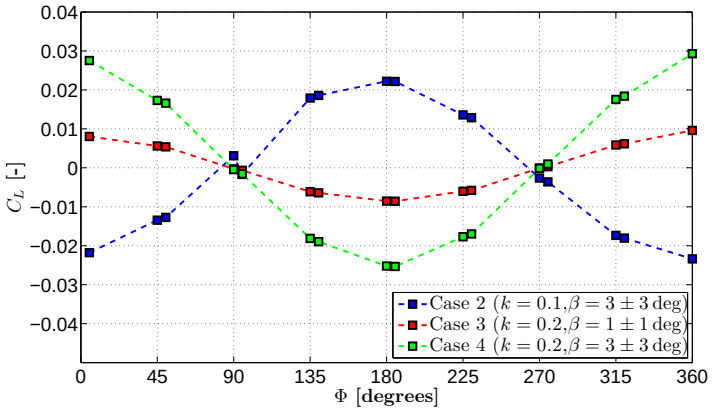

Figure 14.13: The time dependent term for the three unsteady test cases for contour 4

Part IV

Experiment vs Models

Chapter 15

Comparison of the experimental and simulated force data

In this chapter the force results of the experiment and the panel code are compared. The analyses is based on the results obtained in previous chapters. The difference between the model and the experiment is decomposed in terms of the errors encountered in the analysis of the experimental data and the panel code data. By indicating the effect of a specific error on the force, the physical difference between the panel code and the experiment can be deduced.

Section 15.1 illustrates the force difference between the experimental and simulated approach. It defines the errors as encountered in previous chapters in relation with the two models. Section 15.2 gives a discussion on the differences between the actual physics measured and the physics simulated through application of the panel method. In this analysis the separate terms of the momentum flux equation are key for a thorough understanding of the difference between the unsteady experiment and the simulation. In Section 15.3, the flow fields of the experiment and the panel code are compared in relation with the terms addressed in the momentum flux equation.

15.1 Force error analysis

Figure 15.1 shows an offset between the experiment and the panel code. This result is found for all the unsteady cases considered (Appendix D).

The difference between the force results of the experiment (Chapter 12) and the panel method (Chapter 14) can be expressed as Equation 15.1, where $\epsilon_{physical}$ is the error between the physics observed and the model, ϵ_{flap} is the error due to the inaccurate determination of the flap, ϵ_{aoa} is the error associated with the inaccurate determination of the angle of attack, ϵ_{PIV} are the errors inherent to the setup of the PIV experiment and

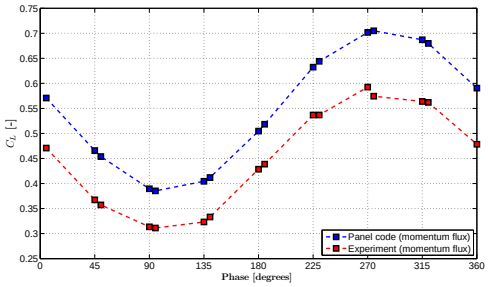

Figure 15.1: The difference between the force of the experiment and the panel code (momentum flux approach) for $k = 0.1$ and $\beta = 3 \pm 3°$

the correlation errors, ϵ_{time} is the error due to the coarsness of the time resolution, ϵ_{space} is the error due to the coarsness of the spatial resolution and $\epsilon_{gradient}$ is the truncation error introduced by the application of a first order difference scheme for the calculation of the derivatives.

$$\epsilon_{expvspan} = \epsilon_{physical} + \epsilon_{flap} + \epsilon_{aoa} + \epsilon_{PIV} + \epsilon_{time} + \epsilon_{space} + \epsilon_{gradient} \tag{15.1}$$

The most interesting difference to determine in this research is $\epsilon_{physical}$, where the physical differences between experiment and model are expressed. In order to determine this $\epsilon_{physical}$, the other errors denoted in Equation 15.1 need to be eliminated. In this research analysis is performed on ϵ_{time}, ϵ_{space}, ϵ_{PIV}. There are still three components that need to be examined in order to determine $\epsilon_{physical}$, of which two components will be analyzed, which are ϵ_{flap} and ϵ_{aoa}. In this research there is no analysis applied on finite difference schemes to calculate velocity derivatives. In the following paragraphs all the errors are adressed.

The ϵ_{piv} error The ϵ_{piv} error is associated with the setup of the PIV experiment and the postprocessing of the acquired images. Due to a limitation in subpixel accuracy, the determined velocity vectors include errors. An analysis on this error is performed in Section 11.2.2. The section reveals the different accelerations obtained due to the use of different correlation methods. According to the theory presented in the same section, the errors on the acceleration term can be large depending on the subpixel accuracy, the resolution, the pixelshift and the time interval between two pairs of images. It is shown that the larger the resolution of the interrogation window, the better the prediction of the acceleration will be, since smaller time intervals can be chosen, without an increase in noise. The reader is referred to Section 11.2.2 for an analysis on this mechanism. According to Theodorsen's function (Equation 5.32), unsteady aerodynamics for an oscillatory motion results in a phase shift and amplitude change driven by the reduced frequency k. If the acceleration of the flow is not captured properly an error will occur in the determination of the time term. This term seems to have a large influence on the phase shift observed as written in the next paragraph.

Next to distortions felt in the time dependent term due to errors in the determination of

Comparison*	Experiment$_{MC}$	Panel method$_{MF}$	EP_{flux}	EP_{val}
Case2	6.5 (lead)	8.9 (lag)	3.4 (lead)	12 (lag)
Case3	13.9 (lead)	13.5 (lag)	1.8 (lead)	25.6 (lag)
Case4	13.6 (lead)	10.0 (lag)	2.4 (lead)	21.2 (lag)

Table 15.1: The comparison of the phase lag $\Delta\phi$ for the different force determination approaches and models. * denotes the phase lag/lead for Experiment$_{MC}$ (momentum flux versus circulation), Panel method$_{MF}$ (momentum flux versus panel method direct output),EP_{flux} (experimental momentum flux approach versus panel code momentum flux approach) and EP$_{val}$ (experimental circulation approach versus panel method direct output).

the acceleration, the errors in the velocity vectors also affect the momemtum term (velocity), vorticity term (vorticity) and the viscous term (viscosity). In order to get insight in what the influence of the subpixel accuracy error is, the panel code is subjected to a simple model of noise that mimics the distortion due to subpixel accuracy. The effect of the noise introduces deviations in the force determined by the momentum flux approach and adds to the error ϵ_{piv}.

The ϵ_{time} error The results are validated for both the panel method and the experiment through different force determination approaches. The temporal resolution defined in the evaluation of the momentum flux equation, shows to have an effect on the phase lag in the sin motion as demonstrated in section 14.4. By introducing a coarse time step the time derivative is not accurately determined. Section 14.5.2 shows that the time dependent term can even show opposite trends, by changing the time interval in the determimnation of the acceleration of the flow. This is indicative for the fact that the time scale of the unsteady aerodynamics is not suited for the time intervals ($\Delta\phi_t$=45) chosen in the panel code. For the experimental data this effect is also detected by comparing the circulation force determination and the momentum flux force approach.Table 15.1 shows the deviation between the result of the momentum flux method and the validation force method for both the experiment as the panel method.

The table (first two columns) illustrates that a difference exists in the determination of the lag (ϕ) in the sinusoidal force compared to the original sinusoidal flap motion between the momentum flux equation and the validator method (circulation and panel code direct force output). The third and fourth column of the table show the deviation between experiment and panel code for the momentum flux approach (experiment and simulation) and the validation methods (experiment and simulation).

As stated in Section 12.4 and 14.4, the validation methods (circulation and direct force output) do not require the definition of the time resolution. Hence these values (EP$_{val}$) give a better understanding, between the physical difference of the experiment and model in terms of phase difference ($\Delta\phi$). From the table the following observations are made;

Comparing the two force procedures for the experimental data, a phase lead is observed for the momentum flux results. If the same is done for the two panel method results, a lag is detected in reference with the momentum flux approach.

The results EP_{flux} show that differences are small between the momentum approach for the experiment and panel method. A small lead is detected for the results of the experiment. Comparing the results of circulation (experiment) and direct force output (panel method), denoted with EP_{val} differences in phase are large. Thereby it can be concluded that a coarse time step of $\phi = 45°$ has a damping effect on the imaginary part of Theodorsen's function which is responsible for the phase difference (lag).

The ϵ_{space} error As demonstrated in Chapter 9 the resolution of the grid has a large influence on the determination of the vorticity term. A resolution which is too coarse, results in inaccurate force values. An analysis on grid resolution and force is performed in the panel method simulation. This analysis shows that the influence of the grid resolution is small in case of the resolution of the experiment (3.5 mm x 3.5mm).

The ϵ_{flap} and ϵ_{aoa} error The experimental error on the flap angle β is described in Section 10.5. Here it is assumed that $\epsilon_\beta = 1$ °. The offset in lift force might be caused by this uncertainty. The offset as depicted in Figure 15.2 is reduced by changing the amplitude flap position (other cases are found in Appendix D). It shows that for $\beta = 1.4°$ (flap up) the equilibrium force positions coincide. The force is plotted for both the momentum flux approach (with the same temporal and spatial resolution for panel code and experiment) and the validator methods (circulation and direct force output).

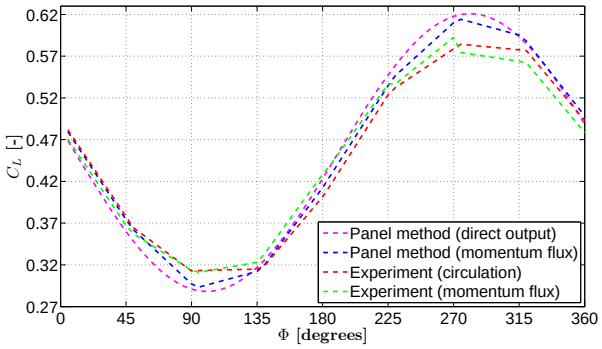

Figure 15.2: The experimental and simulated unsteady force for β-corrected case 2 ($k = 0.1, \beta = 3 \pm 3 - 1.4$)

The panel method force results show larger amplitudes for all unsteady cases. The cause of this effect can be explained by an error in the determination of the amplitude or a difference accounted to the physical assumptions of the panel code. In the latter case the difference between the experiment and model is caused by the physical boundary layer which is absent in the panel simulation.

The possible error on angle of attack ϵ_{aoa} is not considered in determining the new airfoil model-flap geometry.

The $\epsilon_{physical}$ error The potential flow of this panel model lacks some characteristics for real flows. The flow is assumed to be irrotational, incompressible and inviscid, meaning

that regions with large vorticity result in poor predictions. By knowing this the wake is always badly predicted by the panel code, which also is evident from Figures 15.9 to 15.12. The difference between the vorticity in the flow domain, as shown in previous chapters, for the real case and the panel prediction is evident. The panel code cannot model a boundary layer and therefore the curvature of the airfoil model is felt by the flow, whereas in the real case the boundary layer reduces the curvature slightly, reducing the lift acting on the body. So it is expected that the panel code would actually overpredict the lift, which is the case as found in Figures 15.2. The paradox of D'Alambert prevents a proper prediction of the drag. Therefore only the difference in the lift force is analyzed in the following section (Section 15.2).

15.2 Momentum flux term comparison for experiment and panel simulation

In order to compare the seperate contributions (momentum term, vorticity term and the time dependent term) to the force vector two contours are selected in the flow domain. The analysis is performed on basis of the iFFFD method for experimental velocity data (Section 12.5), where the velocity and its derivatives are interpolated for the low quality regions of the flow domain *and* and the flap corrected panel simulation.

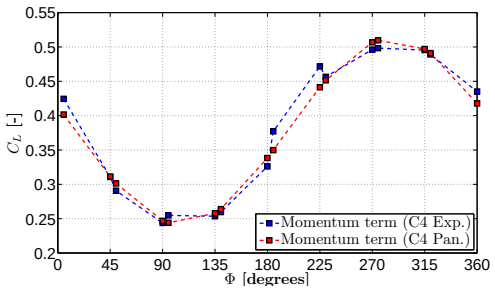

Figure 15.3: The momentum term for case 4 (k=0.2, β=3±3) evaluated on contour 4 for experiment and flap-corrected simulation

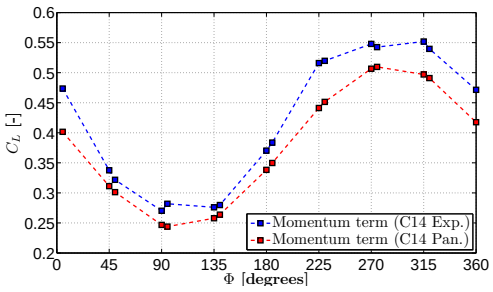

Figure 15.4: The momentum term for case 4 (k=0.2, β=3±3) evaluated on contour 14 for experiment and flap-corrected simulation

The momentum term shows a small error in the comparison of the force for contour 4 (see Figure 14.10). Contour 14 shows a large error, for which the panel force results underpredict the experimental momentum term.

The time dependent term shows a similar behaviour (for experiment and simulation) for the evaluation over contour 4 (C4) as depicted in Figure 15.7. The evaluation of the time dependent term on a large contour (C14), shows a large difference between experiment and simulation. This difference might be the effect of the assumption of incompressibility in the panel simulation. A change in the airfoil shape by flap deflection, is instantly felt in the entire flow domain, where in reality a lag is present. This would also explain the phase difference as denoted in Table 15.1.

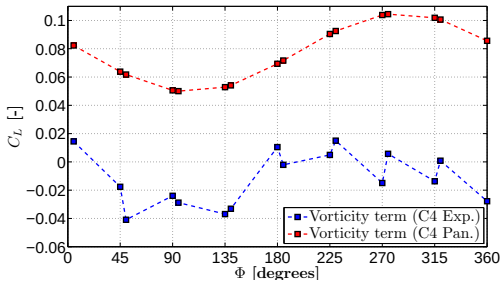

Figure 15.5: The vorticity term for case 4 (k=0.2, β=3±3) evaluated on contour 4 for experiment and flap-corrected simulation

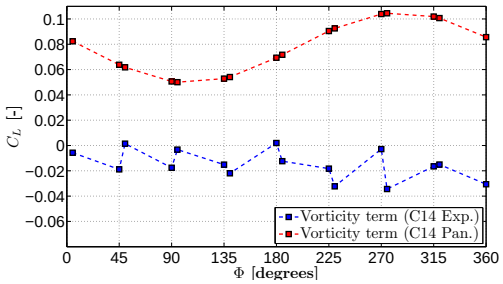

Figure 15.6: The vorticity term for case 4 (k=0.2, β=3±3) evaluated on contour 14 for experiment and flap-corrected simulation

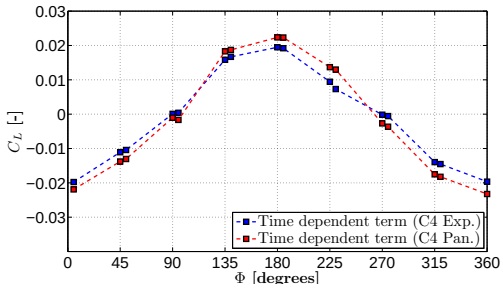

Figure 15.7: The time dependent term for case 4 (k=0.2, β=3±3) evaluated on contour 4 for experiment and flap-corrected simulation

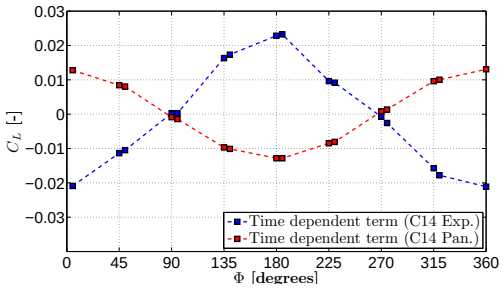

Figure 15.8: The time dependent term for case 4 (k=0.2, β=3±3) evaluated on contour 14 for experiment and flap-corrected simulation

15.3 Comparison of flow features

The difference in the velocity field and its derivatives between the experiment and the panel code is illustrated for case 4 ($k = 0.2$, β=3±3). Figure 15.9 shows a discrepancy in the x-velocity, which is relatively large in the wake and the vicinity of the wake. In the assumption that the flap amplitude B determined in the experiment does not contain large errors, this is expected since the panel code cannot model viscous effects. The y-velocity as shown in Figure 15.10, clearly shows the absence of the boundary layer in the panel code close to the surface. This difference results in an overprediction of the lift in the panel code since the curvature of the airfoil is reduced. This reduction in lift is a function of the phase angle ϕ governed by the unsteady viscous effects. In order to demonstrate this viscous effect, high quality and high resolution PIV data of the boundary layer is required.

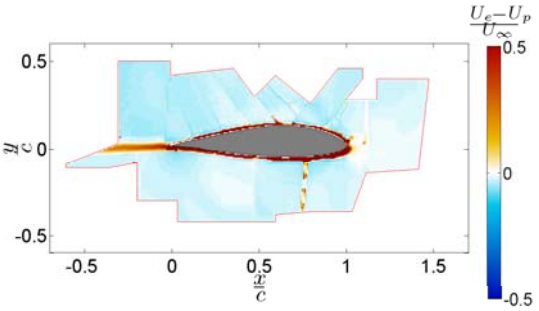

Figure 15.9: The dimensionless error in x-velocity ($\frac{u_e-u_p}{U_\infty}$) between experiment and simulation for $k = 0.2$, β=3±3°.

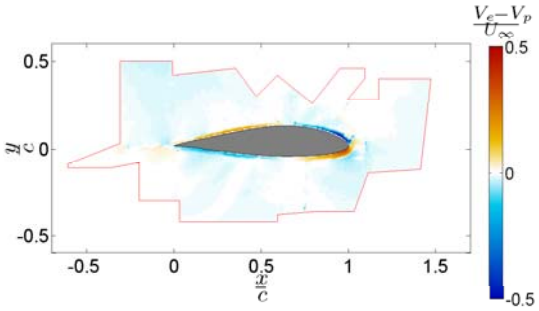

Figure 15.10: The dimensionless error in y-velocity ($\frac{v_e-v_p}{U_\infty}$) between experiment and simulation for $k = 0.2, \beta = 3 \pm 3$, ϕ=90°.

The vorticity difference between experiment and simulation is visualized in Figure 15.11. A large difference is observed from the comparison of the vorticity term as described in the previous section. The noisy character of the experiment is absent in the panel code simulation, where the vorticity term perfectly follows a sinus. The figure shows that the difference between experiment and simulation is of the scale of the experimental vorticity. The artificial vorticity as described in Chapter 12 is clearly visible in the figure, which might cause the noisy behaviour as observed in the experimental vorticity term.

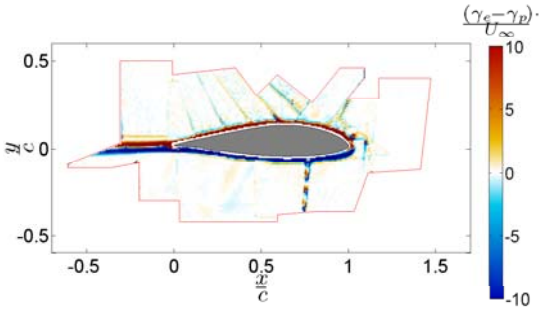

Figure 15.11: The dimensionless error in vorticity between experiment and simulation for $k = 0.2, \beta = 3 \pm 3$, ϕ=90°.

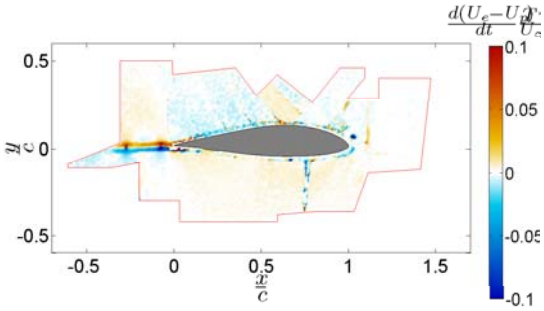

Figure 15.12: The dimensionless error in x-acceleration between experiment and simulation for $k = 0.2, \beta = 3 \pm 3$, ϕ=90°.

Chapter 16

Conclusions

The research presented couples the force results of a Particle Image Velocimetry (PIV) experiment to the force output of a potential flow panel simulation. The focus lies on the determination of the unsteady lift force by means of the momentum flux equation (F. Noca et al [1999]). The comparison between the experiment and simulation serves as a case to identify the errors inherent to the setup of the PIV experiment and the postprocessing of the experimental data. The objective of the thesis is repeated:

> *The determination of the unsteady forces on a DU96W180 airfoil with actuated flap by application of Particle Image Velocimetry and validation of the unsteady forces by a potential flow model*

In order to reach the posed objective, an experiment and potential flow simulation are performed in which the behaviour of the flow is respectively recorded through PIV and simulated by means of a panel method. Three unsteady test cases are defined, which are the cases at $k = 0.1$, $\beta = 3 \pm 3\,\text{deg}$; $k = 0.2$, $\beta = 1 \pm 1\,\text{deg}$, $k = 0.2$, $\beta = 3 \pm 3\,\text{deg}$. In all cases it is assumed that the flap oscillates according to a sine.

Although the experimental data contains errors related to the experimental setup, (the pre-/postprocessing of the PIV data and the numerical errors introduced on basis of the finite spatial and temporal resolution) the experimental results seem to follow the trend of the lift forces calculated by the panel simulation. The drag force shows a large domain of uncertainty and thereby lacks the quality for proper force prediction. In the determination of the force, multiple contours are selected, which address different regions in the flow. Because of the relatively small flow domain on which velocity vectors are determined, the variation of the position and size of the ellipses (integration contours) is limited. The error in the flow quantities is a function of space and time, and therefore each separate contour is subjected to different errors. In order to reduce the statistical error, the average of all the calculated forces in the set of contours is calculated. Thereby the large fluctuations

in the force spotted in separate evaluations are reduced. The averaging process seems to work and determine a correct trend compared to the panel results.

From the flap angle corrected force comparison between the experiment and the panel code by evaluation of the momentum flux equation, it shows that the unsteady force from experiment and panel method differ in amplitude and phase. The difference between the models is explained on basis of the analysis of the terms defined in the momentum flux equation.

On basis of the PIV velocity fields acquired, the forces on the airfoil model are determined through application of the momentum flux equation and the determination of the lift force by the concept of circulation. Comparing both methods, a clear difference in phase lag is detected, where the circulation determines larger phase lags. This effect is more pronounced for the unsteady cases associated with k=0.2. The force determination by circulation does not include a time dependent term. Therefore, the error associated with a coarse time resolution cannot exist in the evaluation of the force as such. Most probably the difference in the phase lag for the two different approaches is due to the time dependent term determination in the momentum flux equation.

The time-dependent term can only be properly determined under certain conditions. As stated in Section 11.2.2 the acceleration of the flow is determined by a first order forward difference scheme. This method requires two pairs of images to determine the acceleration. The time in between the two pairs of images, is limited by the noise in the PIV measurements. If the time interval reduces, the velocities measured per pair of images converge. At some small time interval Δt, noise becomes dominant such that the time dependent force cannot be determined properly. According to the statistical reduction methods, noise can be removed by increasing the number of samples. This method will only work when a purely random noise exists. Another way of improving the time dependent force term is by reducing the size of the interrogation window, such that a large absolute pixel shift is possible. In order not to lose spatial resolution by increasing the size of the interrogation window, the camera has to zoom in on that region. In essence the sub pixel accuracy of the PIV correlation method responsible for the error, drives this mechanism. Summarizing, it can be stated that a limitation in the temporal resolution means a limitation in the unsteadiness of the flow that can be measured.

The analysis on the resolution of the acceleration for the calculation of the time term is performed in the panel code simulation and shows large differences when different time resolutions are adressed, where opposite trends can be predicted. From the analysis of the total force as a function of time resolution, it can be stated that the time dependent term is at least partly resonsible for the phase shift explained by Theodorsen. In case the time dependent term is not properly predicted, the phase shift will also be erroneous.

Spatial resolution has a large effect on the determination of vorticity. The vorticity term from the experimental result shows large fluctuations, whereas the simulation shows a smooth sinusoidal trend. From theory it is known that potenial flow cannot contain vorticity in the solution domain. It only excepts singularities that mimic the effect of vorticity. It can be concluded that the results from the experiment and the simulation do

not give a clear answer on the prediction of the vorticity force term. Additional research is required to determine the influence of spatial resolution on the vorticity term. From this information it can be stated whether the noisy character is physical. Higher spatial resolutions also imply better predictions of the drag force. In this research drag is only considered in the experimental part, showing very large uncertainties, because of a probable error in the vorticity term.

The viscous term (associated with second derivative of the flow) is even more difficult to determine than the vorticity. In this experiment the data lacks the quality to properly determine the force on basis of the viscosity term, which will increase when a contour is selected close to the airfoil's surface.

All the errors addressed prohibit the determination of the physical difference between the forces of the panel code and the experiment. The nature of the errors is determined and therefore the difference between the experiment and model can qualitatively be described. Chapter 15 reveals the offset between the experiment and the panel code both calculated on the same grid, with the same time step and the same integration contours. The momentum term, the vorticity term and the time dependent term are compared at the same integration contour. It shows that the time dependent term acts in an opposite manner for the force over the selected contour. This effect might be caused by the incompressibility assumption of the potential flow model. A change in the airfoil geometry is directly felt over the entire flow domain. In this case it might be that the accelerations measured over the contour are distorted instantly, where the physical situation dictates that there should be a decelerating or accelerating effect.

In the total lift force for the flap corrected simulation and the experiment it shows that the panel code reaches larger force peaks at respectively $\phi = 90\,\text{deg}$ and $\phi = 270\,\text{deg}$ than the experiment. This is probably caused by the fact that the panel code ceases to model a boundary layer, which results in an effective decrease of the airfoil's curvature. This in turn leads to a decrease in lift prediction. However, the correction of geometry is only performed on the flap angle and not on the angle of attack. This might also cause the deviation between experimental and simulated results.

Both the model and the experiment follow the theory of Theodorsen, which shows a reduction of amplitude and an increase in phase lag when larger reduced frequencies are considered. The effect of amplitude on the phase lag is most probably best predicted by the evaluation of the experimental lift force by the time independent circulation calculation. The influence of flap amplitude is evaluated and shows that, keeping the reduced frequency constant, a small amplitude induces a larger phase lag compared to larger amplitudes. This result is also found in the evaluation of the momentum flux equation with a relatively coarse time resolution. Thereby the trend of the unsteady lift force is similar for both methods, but differ in the value of the phase lag.

Finally, it can be stated that the momentum flux method presented has the potential to capture unsteady forces. In order to capture vorticity (as part of the force determination) accurately, spatial refinement is necessary. From the research it also shows that high reduced frequency flows are difficult to capture in terms of time resolution. The

noise in the measurements prohibit the accurate determination of acceleration of the flow. Thereby it can be concluded that the determination of unsteady forces is limited by the experimental approach presented in this research.

Chapter 17

Recommendations

The methodology shown in this thesis is based on the experimental data acquired. The method shows an averaging of the forces obtained over multiple contours, to overcome the fact that a single contour contains random errors. By applying multiple force integrations the random error is minimized as long as a homogeneous random error distribution is valid. However, systematic errors still can have a large influence on the forces obtained. With the final goal to present a reliable method for the evaluation of the unsteady force with the ultimate goal to improve numerical methods for practical purposes, the systematic and random errors contained within the solution based on the experimental data need to be reduced. The error can be decomposed in three parts: the experimental error, the PIV correlation error, the numerical postprocessing error related to the momentum flux equation in correspondence with finite spatial and temporal resolutions.

The experimental error consists of calibration errors on the flap angle and the angle of attack. The angle of attack is determined by the procedure shown in Figure 10.8. An accurate mould would have provided a means to more accurately define the angle of attack of the main wing, such that the error could have been reduced. For the flap angle the same error can be reduced by using more accurate moulds. Furthermore a potentio meter is used to determine the flap angle in time, which seemed to be senstitive for inaccurate angle read-outs. More accurately determining the flap angle *beta* and angle of attack α, would obviously yield better comparison material for numerical methods.

Another experimental error is due to the setup of the PIV equipment. A co-planar orientation of the cameras is used to capture the flow around the airfoil over 16 fields of view. In the postprocessing it turned out that the orientation of the fields of view is not so straightforward and misalignment errors occurred. By reducing the number of fields of views this error is reduced considerably. In order to reach the same spatial resolution this means that high resolution cameras should be used instead of the 1.3 megapixel cameras used during the experiment.

Next to that a mirror is used to illuminate the upper side of the airfoil model. By doing so the power of the laser light reduces along the path it has to travel. It is important to keep the path of the laserlight as short as possible, to make sure that a proper illuminated area of particles can be recorded. Knowing this, the results would improve if the topsurface is directly illuminated without the use of a mirror. In this experimental setup (Figure 10.17), the laser can be placed on top of the windtunnel or the blade can be rotated upside down. The last option might induce slightly different flap dynamics due to the involvement of gravity acting on the flap in a different direction.

The PIV correlation error is based on the pre- and postprocessing techniques used with the goal to obtain the velocity vectors. As shown in Chapter 11 multiple techniques apply to a variety of differently appearing flow features. By having multiple fields of view, different regions with different illumination properties exist. Every field of view needs a special pre-/postprocessing technique to optimize for the correlation error inherent to the correlation. In this experiment the variety of techniques used is confined to sequential cross correlation with only some preprocessing techniques to reduce the reflections at the airfoil surface. If the different fields of view would have been treated with a dedicated processing technique some improvement would probably have been possible.

Insight is required in how the processing technique influences the determination of the time dependent term of the momentum flux equation. It is important to know what drives the limitation in determining the time dependent term. In this experiment it is demonstrated that a limitation exists, based on the processing technique used. If a clear indication in terms of processing techniques can be given about the causes of these limitations, the PIV experiments can be improved and higher time resolutions can be considered. With the knowledge that the error in the velocity vector reduces with increasing interrogation window size (Equation 11.5), it can be decided to use larger interrogation windows to cover the same area. By doing so more fields of view are necessary or higher resolution cameras are required.

The numerical errors associated with the momentum flux equation exist due to the finite spatial and temporal resolution in combination with the techniques to obtain the flow derivatives. According to the analysis on space and time refinement on basis of the potential flow model, the gradient function lacks the capabillity to predict the flow derivatives. The regions that include large vorticity such as the wake give an erroneous contribution to the total force on the body. As long as the numerical methods are not sufficient to capture the flow dynamics in the domain, where the integration takes place, it can be decided to choose contours further away from the body such that the vorticity term is considerably reduced in the outer region of the flow domain. However, an amplification effect of the error exists in the momentum term due to the square in the mathematical expression. This in turn can degradate the obtained force results. To overcome this effect, the error governed by Equation 11.5 should be reduced by choosing an appropriate pre-/postprocessing scheme *with* an adequate resolution.

In order to determine the fluctuations associated in the flow, the set of hundred observations used for the phase locked average should be statistically analyzed. The standard deviation obtained is an integrated value of the statistical error and the turbulent fluctua-

tions. This can be extended to the statitistical analysis of the force of a set of observations. Thereby insight is created on the effect of turbulence on the unsteady force.

The research performed compares experimental data with a potential flow simulation. In order to get more insight in the vorticity close to the airfoil, it can be decided to perform a similar analysis with e.g. a Reynolds-Averaged Navier-Stokes equation, which includes the effect of viscosity that is responsible for emanation of vorticity. From the experimental results it cannot be determined whether the fluctuations in the vorticity term are physical. With a RANS method this insight might be created. Also the time dependent term of the experiment showed strong deviations with the time term of the panel method. An analysis of RANS might also explain the difference between the experiment and potential flow simulation.

References

Aeroelasticity. (2007). Lecture notes Delft University of Technology.

C. Bak et al. (2007). Wind tunnel test on wind turbine airfoil with adaptive trailing edge geometry. *45th AIAA Aerospace Sciences Meeting and Exhibit*.

C.J. Simao Ferreira et al. (2008). Using PIV for Determining the Blade Load on a VAWT in Dynamic Stall. *46th AIAA Aerospace Sciences Meeting and Exhibit*.

Dixon, K. (2008). *The near wake structure of a vertical axis wind turbine.* Mémoire de Master non publié, Delft University of Technology.

Drela. (2001, February). *Xfoil.* Disponible sur http://web.mit.edu/drela/Public/web/xfoil/

Experimental Aerodynamics. (2007, 1 April). Lecture notes Delft University of Technology.

F. Noca et al. (1999). A comparison of methods for evaluating time-dependent fluid dynamic forces on bodies, using only velocity fields and their derivatives. *Journal of Fluids and Structures*, *Vol. 13*, pp. 551 – 578.

J. Katz et al. (2001). *Low-speed Aerodynamics.* Cambridge : Cambridge University Press.

J.W. van Wingerden et al. (2008). On the Proof of Concept of a Smart Wind Turbine Rotor Blade for Load Alleviation. *Wind Energy*, *Vol. 11*, pp. 265 – 280.

LaVision. (2005). DaVis FlowMaster Software [Manuel de logiciel]. Gottingen : LaVision.

Markus Raffel et al. (2007). *Particle Image Velocimetry A Practical Guide 2nd edition.* New York : Springer.

Rooij ir. R.P.J.O.M van. (2008). *The duwind airfoils.* windworkshops. Disponible sur http://www.windworkshops.tudelft.nl/files/presentaties/1A/Ruud/DWW

T. Buhl et al. (2005). Potential of load reduction using airfoils with variable trailing edge geometry. *Journal of Solar Energy Engineering*, *Vol. 127*, pp. 503 – 516.

Takahashi, M. D. (2006). Unsteady 2D potential-flow forces on a thin variable geometry airfoil undergoing arbitrary motion. *Technical report Riso, Riso-R-1478(EN)*.

Whittaker E.T. (1915). Expansions of the Interpolation-Theory. *Proc. Roy. Soc.*, *Vol. 35*, pp. 181.

Appendix A

Mathematical formulae

A.1 Momentum flux equation

$$\oint_{S(t)} \vec{n} \cdot \gamma_{flux} dS = \underbrace{\frac{1}{2}\begin{bmatrix} U_{total}^2 & 0 \\ 0 & U_{total}^2 \end{bmatrix} - \begin{bmatrix} u^2 & uv \\ uv & v^2 \end{bmatrix}}_{\text{I}} - \underbrace{\begin{bmatrix} yu\Omega_z & -xu\Omega_z \\ yv\Omega_z & -xv\Omega_z \end{bmatrix}}_{\text{II}}$$

$$\underbrace{- \begin{bmatrix} x\frac{du}{dt} + y\frac{dv}{dt} & 0 \\ 0 & x\frac{du}{dt} + y\frac{dv}{dt} \end{bmatrix} - \begin{bmatrix} x\frac{du}{dt} & x\frac{dv}{dt} \\ y\frac{du}{dt} & y\frac{dv}{dt} \end{bmatrix}}_{\text{III}}$$

$$\underbrace{+\mu \begin{bmatrix} \left(2\frac{\partial^2 u}{\partial x^2} + \frac{\partial^2 u}{\partial y^2} + \frac{\partial^2 v}{\partial x \partial y}\right) x + \left(2\frac{\partial^2 v}{\partial y^2} + \frac{\partial^2 v}{\partial x^2} + \frac{\partial^2 u}{\partial x \partial y}\right) y & 0 \\ 0 & \left(2\frac{\partial^2 u}{\partial x^2} + \frac{\partial^2 u}{\partial y^2} + \frac{\partial^2 v}{\partial x \partial y}\right) x + \left(2\frac{\partial^2 v}{\partial y^2} + \frac{\partial^2 v}{\partial x^2} + \frac{\partial^2 u}{\partial x \partial y}\right) y \end{bmatrix}}_{\text{IV}}$$

$$\underbrace{- \mu \begin{bmatrix} \left(2\frac{\partial^2 u}{\partial x^2} + \frac{\partial^2 u}{\partial y^2} + \frac{\partial^2 v}{\partial x \partial y}\right) x & \left(2\frac{\partial^2 v}{\partial y^2} + \frac{\partial^2 u}{\partial x \partial y} + \frac{\partial^2 v}{\partial x^2}\right) x \\ \left(2\frac{\partial^2 u}{\partial x^2} + \frac{\partial^2 u}{\partial y^2} + \frac{\partial^2 v}{\partial x \partial y}\right) y & \left(2\frac{\partial^2 v}{\partial y^2} + \frac{\partial^2 u}{\partial x \partial y} + \frac{\partial^2 v}{\partial x^2}\right) y \end{bmatrix} + \mu \begin{bmatrix} 2\frac{\partial u}{\partial x} & \frac{\partial v}{\partial x} + \frac{\partial u}{\partial y} \\ \frac{\partial v}{\partial x} + \frac{\partial u}{\partial y} & 2\frac{\partial v}{\partial y} \end{bmatrix}}_{\text{IV}} \tag{A.1}$$

Appendix B

Flow quantities

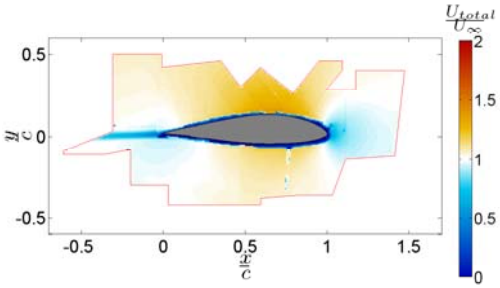

Figure B.1: Total velocity field experiment; k=0.1, amplitude = 3 deg phase = 90 [degrees]

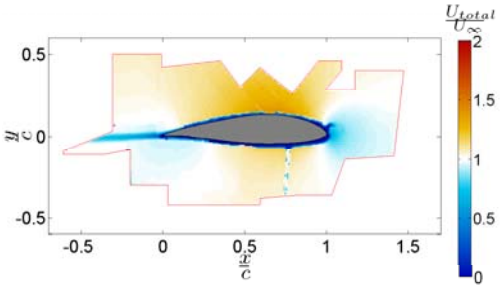

Figure B.2: Total velocity field experiment; k=0.1, amplitude = 3 deg phase = 180 [degrees]

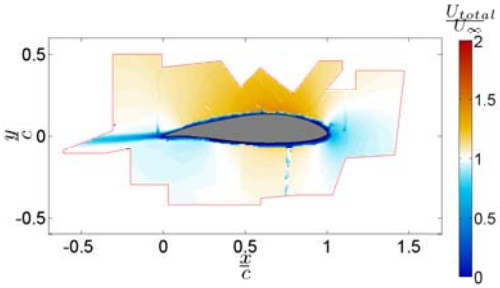

Figure B.3: Total velocity field experiment; k=0.1, amplitude = 3 deg phase = 270 [degrees]

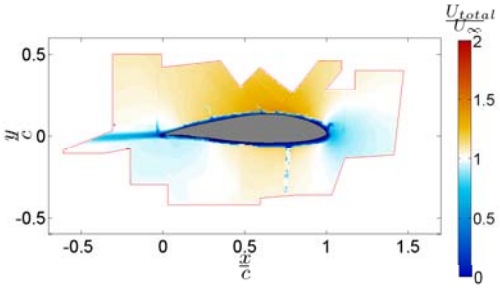

Figure B.4: Total velocity field experiment; k=0.1, amplitude = 3 deg phase = 360 [degrees]

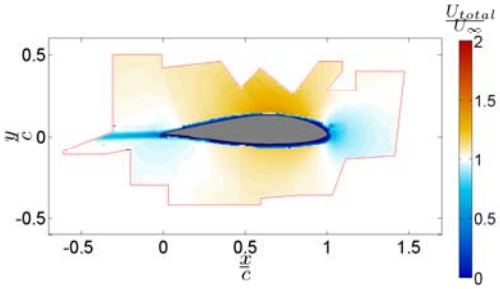

Figure B.5: Total velocity field experiment; k=0.2, amplitude = 1 deg phase = 90 [degrees]

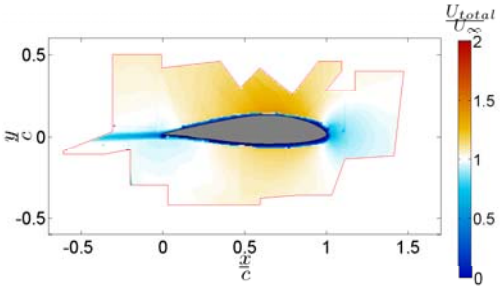

Figure B.6: Total velocity field experiment; k=0.2, amplitude = 1 deg phase = 180 [degrees]

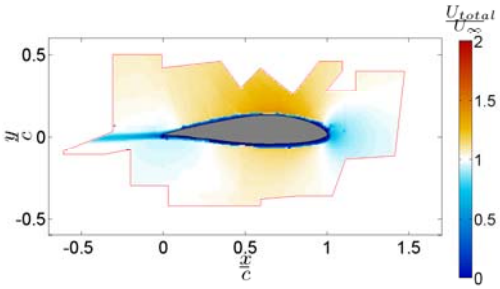

Figure B.7: Total velocity field experiment; k=0.2, amplitude = 1 deg phase = 270 [degrees]

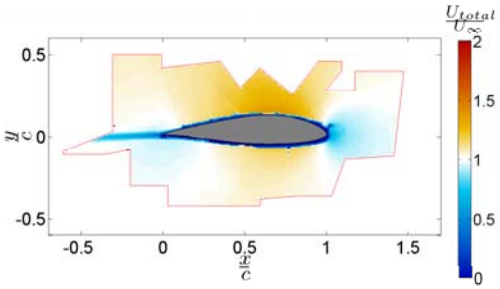

Figure B.8: Total velocity field experiment; k=0.2, amplitude = 1 deg phase = 360 [degrees]

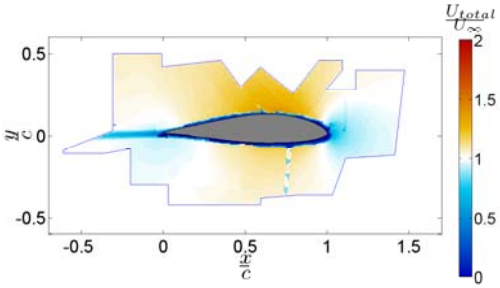

Figure B.9: Total velocity field experiment; k=0.2, amplitude = 3 deg phase = 90 [degrees]

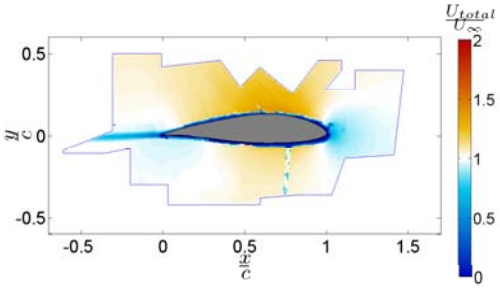

Figure B.10: Total velocity field experiment; k=0.2, amplitude = 3 deg phase = 180 [degrees]

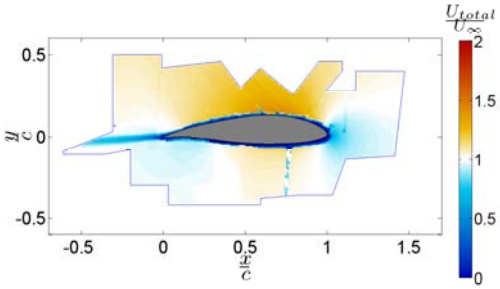

Figure B.11: Total velocity field experiment; k=0.2, amplitude = 3 $\deg$ phase = 270 [degrees]

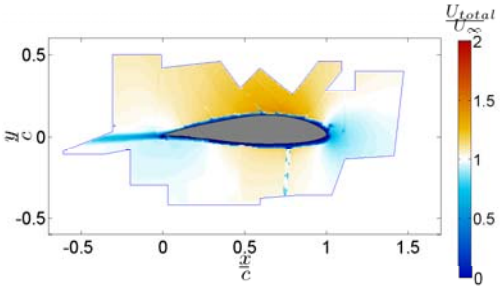

Figure B.12: Total velocity field experiment; k=0.2, amplitude = 3 $\deg$ phase = 360 [degrees]

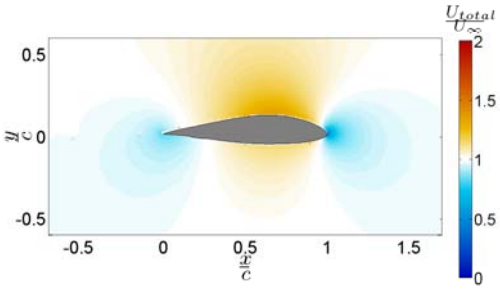

Figure B.13: Total velocity field potential flow; k=0.1, amplitude = 3 $\deg$ phase = 90 [degrees]

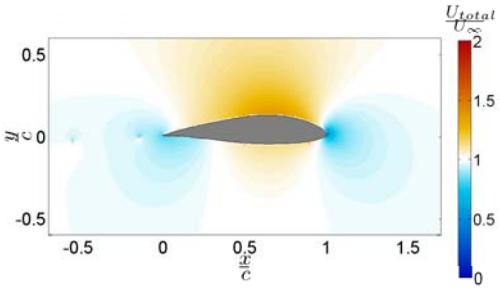

Figure B.14: Total velocity field potential flow; k=0.1, amplitude = 3 $\deg$ phase = 180 [degrees]

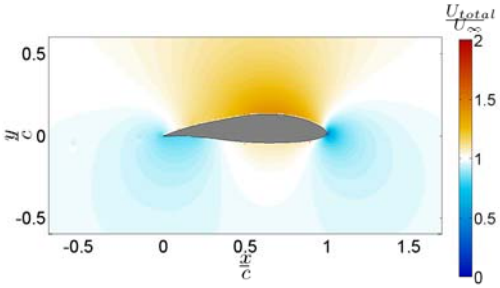

Figure B.15: Total velocity field potential flow; k=0.1, amplitude = 3 $\deg$ phase = 270 [degrees]

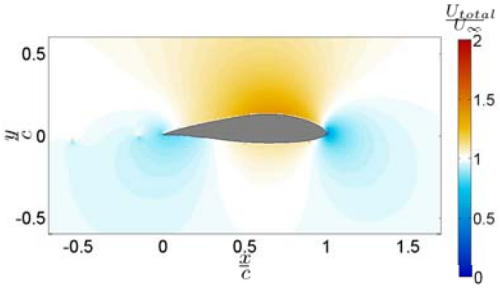

Figure B.16: Total velocity field potential flow; k=0.1, amplitude = 3 $\deg$ phase = 360 [degrees]

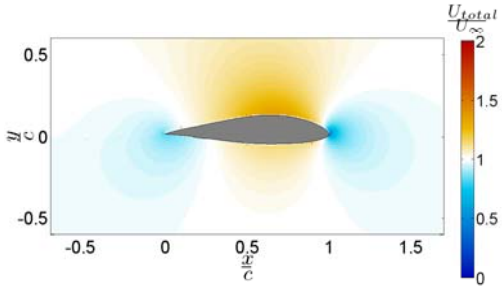

Figure B.17: Total velocity field potential flow; k=0.2, amplitude = 1 $\deg$ phase = 90 [degrees]

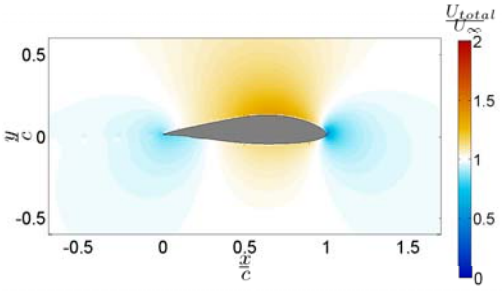

Figure B.18: Total velocity field potential flow; k=0.2, amplitude = 1 $\deg$ phase = 180 [degrees]

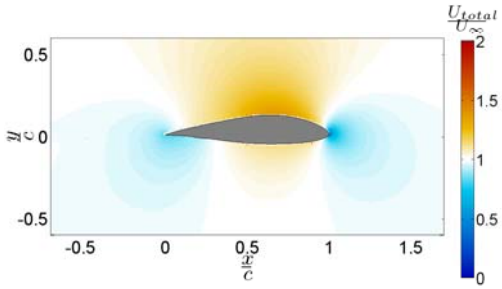

Figure B.19: Total velocity field potential flow; k=0.2, amplitude = 1 $\deg$ phase = 270 [degrees]

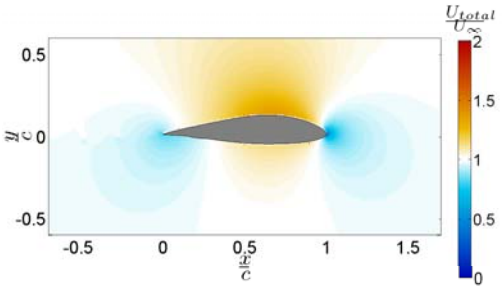

Figure B.20: Total velocity field potential flow; k=0.2, amplitude = 1 $\deg$ phase = 360 [degrees]

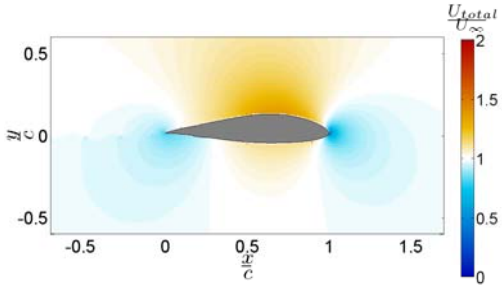

Figure B.21: Total velocity field potential flow; k=0.2, amplitude = 3 $\deg$ phase = 90 [degrees]

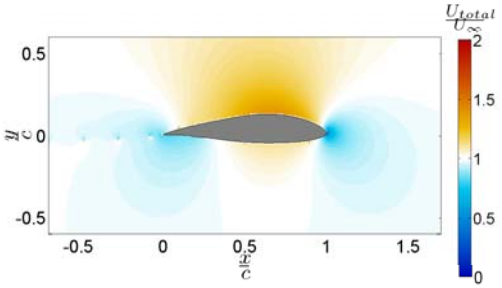

Figure B.22: Total velocity field potential flow; k=0.2, amplitude = 3 $\deg$ phase = 180 [degrees]

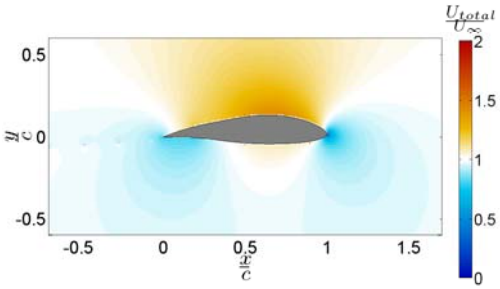

Figure B.23: Total velocity field potential flow; k=0.2, amplitude = 3 $\deg$ phase = 270 [degrees]

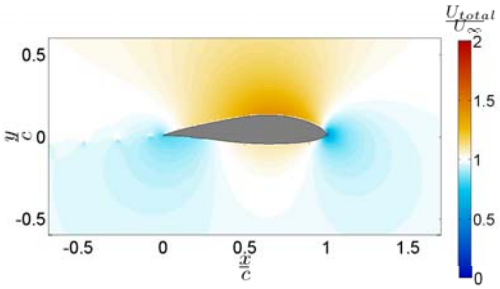

Figure B.24: Total velocity field potential flow; k=0.2, amplitude = 3 $\deg$ phase = 360 [degrees]

Appendix C

Validation with Theodorsen

A panel method is developed as described in 6. In order to validate what the performance of the method is in unsteady conditions, Theodorsens theory will be matched with the results of this panel method. The Theodorsen function models harmonic oscillations in pitch and plunge with a constant forward speed. It's theory assumes that the airfoil can be approximated by a flat plate with zero thickness. Its wake is flat and aligned with the freestream velocity. The flow is assumed to be attached at every instant. All the assumptions stated for potential flow (incompressible and inviscid) also apply. The assumption that the wake is flat and aligned is only valid for k less than 0.4. Otherwise the model ceases to match physical reality J. Katz et al [2001]. Theodorsen's solution **?** for the lift coefficient is denoted in Equation C.1.

$$C_l = \pi b \left\{ \frac{\dot{\alpha}}{V} + \frac{\ddot{h}}{V^2} - \frac{ba\ddot{\alpha}}{V^2} \right\} + 2\pi C\left(k\right) \left\{ \frac{\dot{h}}{V} + \alpha + b\left(\frac{1}{2} - a\right)\frac{b\dot{\alpha}}{V} \right\} \tag{C.1}$$

Where V is the velocity, b is the semi-chord, a is the distance to pitch axis as measured from mid chord (i.e. $a = -\frac{1}{2}$ for pitching about the quarter chord). Equation C.1 is complex valued and contains $C(k)$, Theodorsen's *lift reduction* function. $C(k)$ describes a magnitude reduction and phase shift in the circulatory component of the lift due the presence of the shed wake as a function of the reduced frequency. The term C.1 is split into two types, which are the components associated with circulation ($C(k)$) and the components which have to do with the acceleration of the fluid around the body-termed *added mass*. As k becomes larger, the expressions are dominated by this added mass terms.

For the validation of the panel code it is important that the code follows Theodorsens function for thin airfoils and small oscillations (linear assumption). If the solution of the panel code resembles the solution of Theodorsen, the wake surface is as flat as possible. This is a central assumption in Theodorsens theory.

The panel code is compared with Theodorsens's theory for a pitching airfoil. In this model a NACA0001 profile is used in order to validate the results with Theodorsens theory. The NACA0001 airfoil has one percent thickness which should resemble a flat plate. In Figure C.1 the lift force in time from the panel code and the lift force produced by Equation C.1 are plotted. In the simulation an amplitude of 0.01 degrees (to stay with the assumption of linearity) at a reduced frequency of k=0.1 is assumed, where the pitch axis is at 0.25c. In this figure a shift in phase angle is observed, by comparing the peaks of both plots. In addition, there is a mismatch in the amplitude of the lift, which is likely due to the thickness difference (Dixon [2008]).

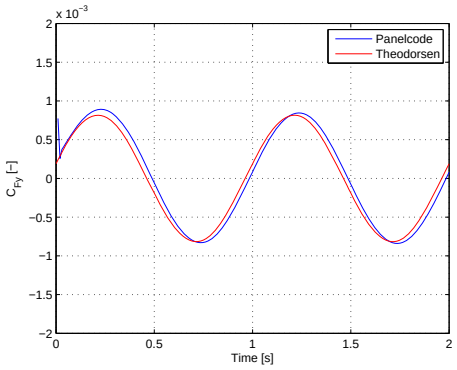

Figure C.1: The lift coefficient in time for a pitching NACA0001 at k=0.1

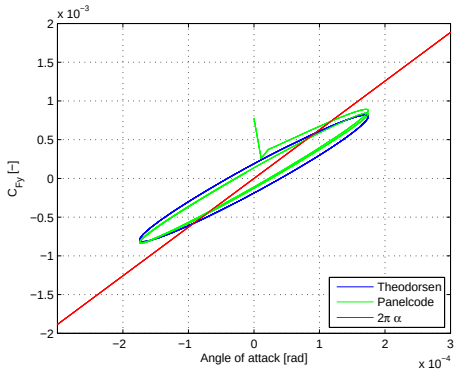

Figure C.2: The lift coefficient as a function of α for a pitching NACA0001 at k=0.1

The effect of thickness is demonstrated by comparing Figures C.2 and C.4, showing the $C_l - \alpha$ loop for a NACA0001 and a NACA0015. The NACA0015 is thicker which means that a greater phase lag between the 'input' angle and the 'output' C_l is obtained. The mean slope is increased slightly which is an effect that thickness has on the lift slope **?**. From the plots in Figures C.1 and C.3 the phase lag between the two cases can be deduced. This effect is accounted to the difference in thickness.

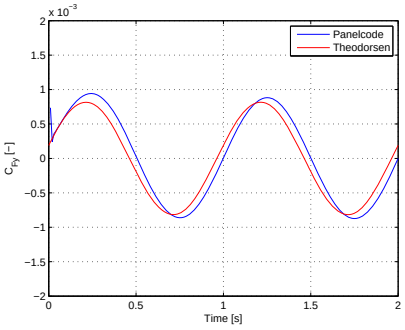

Figure C.3: The lift coefficient in time for a pitching NACA0015 at k=0.1

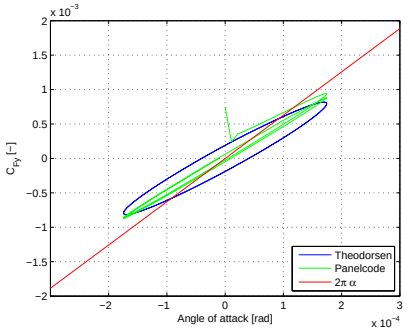

Figure C.4: The lift coefficient as a function of α for a pitching NACA0015 at k=0.1

The model is also tested for reduced frequencies k=0.01 (quasi steady) and k=0.2, since

these (un)steadiness levels are used in the experiment. At higher reduced frequencies Theodorsens theory, assuming that the wake is flat, is not valid any more. Large vorticies exist, which deform the wake. The offset between the panel code and Theodorsens theory increases with reduced frequency k, due to this effect (Dixon [2008]).

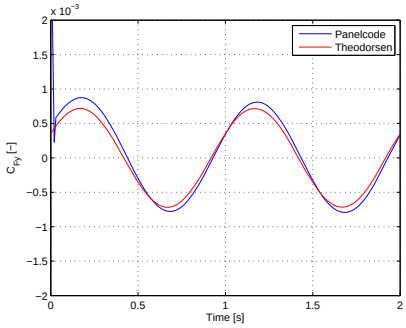

Figure C.5: The lift coefficient in time for a pitching NACA0015 at k=0.2

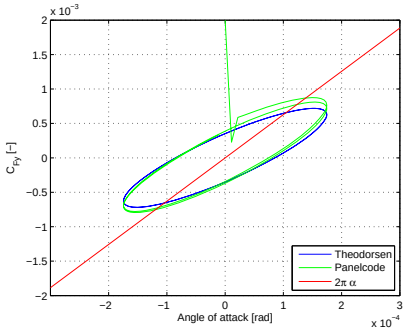

Figure C.6: The lift coefficient as a function of α for a pitching NACA0015 at k=0.2

The quasi steady result shows that the lift slope resembles the steady liftcurve of $2\pi\alpha$, for both the panel code and Theodorsen's theory. In this case Theodorsens Hankel function does not influence the phase and amplitude of the lift output.

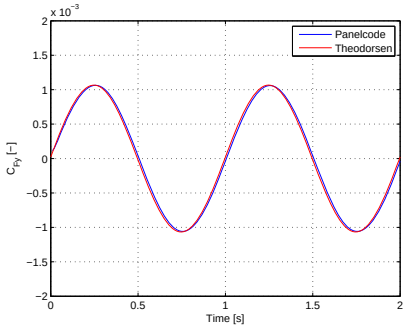

Figure C.7: The lift coefficient in time for a pitching NACA0015 at k=0.01

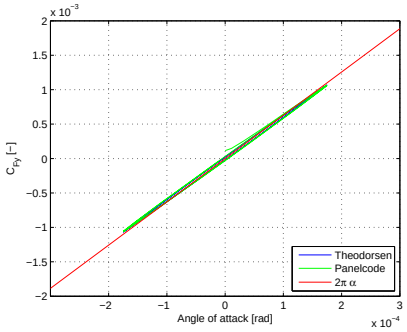

Figure C.8: The lift coefficient as a function of α for a pitching NACA0015 at k=0.01

The validation of the panel code, although performed in pitch only, shows a comparable behaviour (only small deviations are detected) with the widly accepted Theodorsen's theory.

Appendix D

Force results

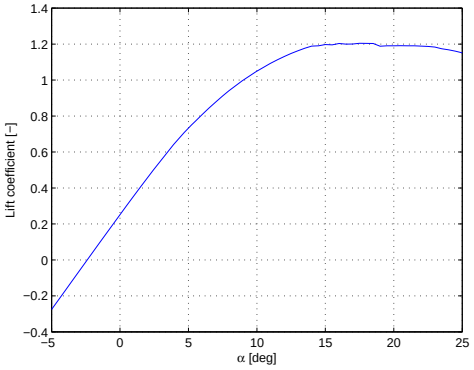

Figure D.1: XFOIL Lift coefficient for a DU96W180 airfoil at Re=7 $\cdot 10^5$

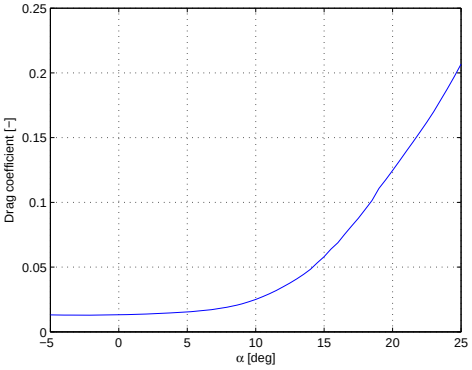

Figure D.2: XFOIL Drag coefficient for a DU96W180 airfoil at Re=7 $\cdot 10^5$

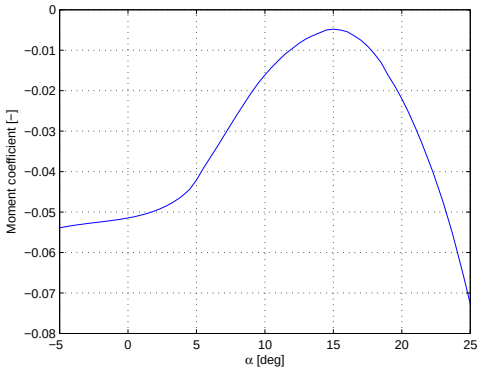

Figure D.3: XFOIL Moment coefficient for a DU96W180 airfoil at Re=7 $\cdot 10^5$

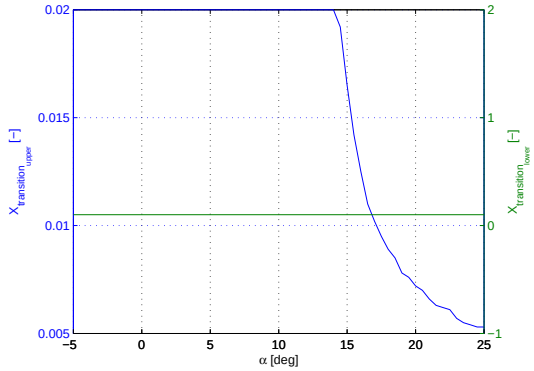

Figure D.4: XFOIL Forced transition for a DU96W180 airfoil at Re=7 $\cdot 10^5$

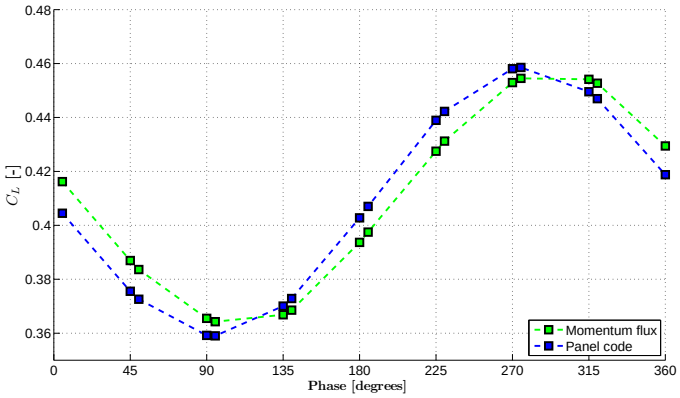

Figure D.5: The lift coefficient determined by the panel code and the momentum flux equation for case 3 ($k = 0.2$ and $\beta = 1 \pm 1\,\mathrm{deg}$)

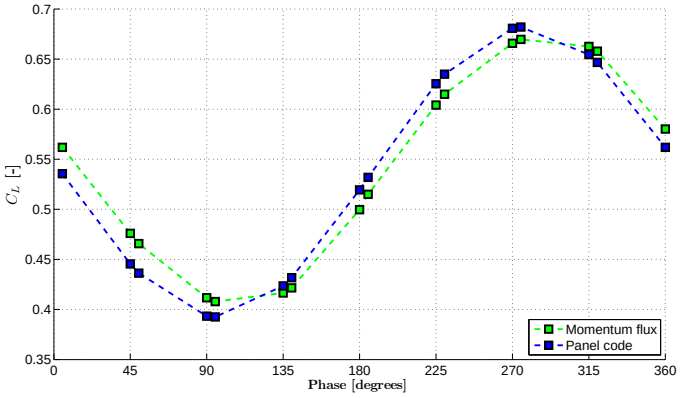

Figure D.6: The lift coefficient determined by the panel code and the momentum flux equation for case 4 ($k = 0.2$ and $\beta = 3 \pm 3\,\mathrm{deg}$)

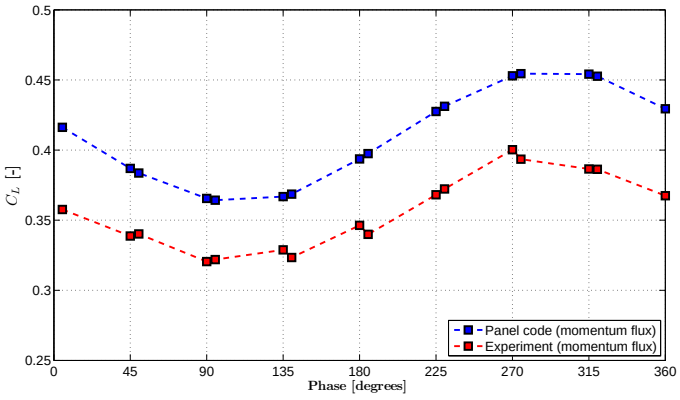

Figure D.7: The difference between the force of the experiment and the panel code over the same set of contours for case 3 (β=$1 \pm 1°$)

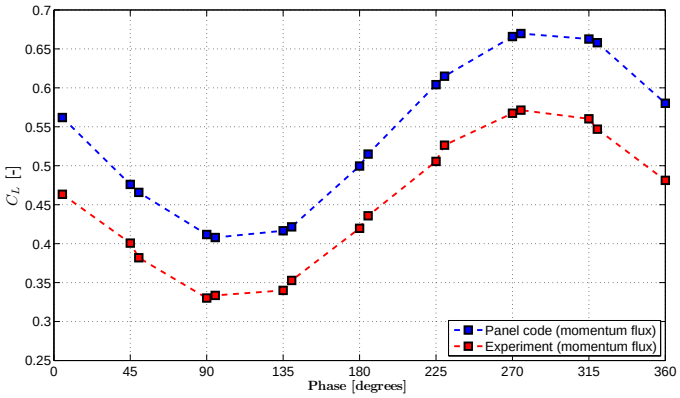

Figure D.8: The difference between the force of the experiment and the panel code over the same set of contours for case 4 (β=$3 \pm 3°$)

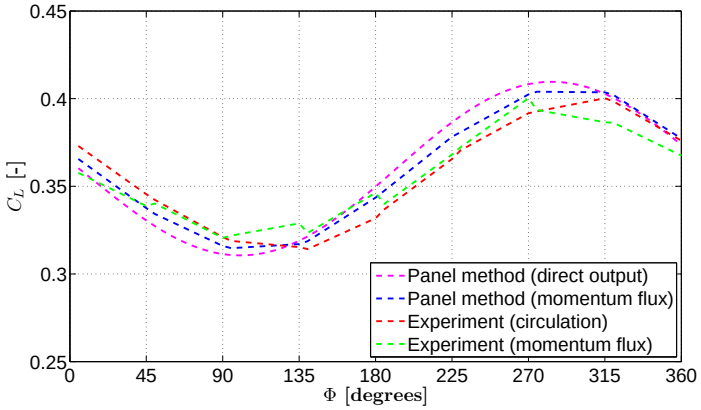

Figure D.9: The experimental and simulated unsteady force for β-corrected case 3 ($k = 0.2, \beta = 1 \pm 1 - 0.7$)

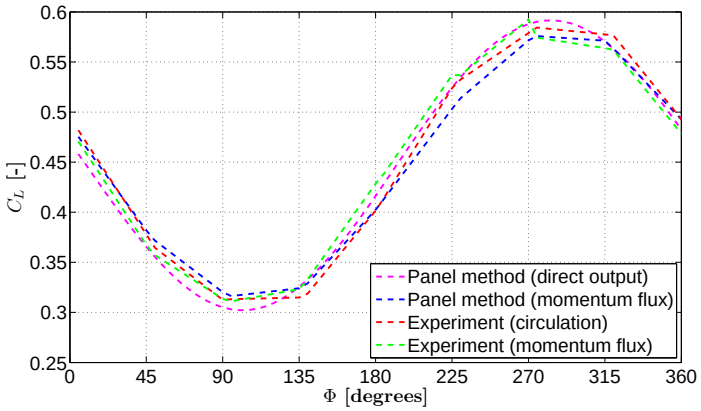

Figure D.10: The experimental and simulated unsteady force for β-corrected case 4 ($k = 0.2, \beta = 3 \pm 3 - 1.4$)